STAR COUNTS IN M31

By

Philip J. C. Hodder
B. Sc. (Astronomy & Astrophysics) University of St. Andrews
M. Sc. (Astronomy) University of British Columbia

A THESIS SUBMITTED IN PARTIAL FULFILLMENT OF
THE REQUIREMENTS FOR THE DEGREE OF
DOCTOR OF PHILOSOPHY

in

THE FACULTY OF GRADUATE STUDIES
GEOPHYSICS AND ASTRONOMY

We accept this thesis as conforming
to the required standard

.....

THE UNIVERSITY OF BRITISH COLUMBIA
1995

In presenting this thesis in partial fulfilment of the requirements for an advanced degree at the University of British Columbia, I agree that the Library shall make it freely available for reference and study. I further agree that permission for extensive copying of this thesis for scholarly purposes may be granted by the head of my department or by his or her representatives. It is understood that copying or publication of this thesis for financial gain shall not be allowed without my written permission.

Geophysics and Astronomy
The University of British Columbia
129-2219 Main Mall
Vancouver, Canada
V6T 1Z4

Date: 13 July 1995

Abstract

The structural properties of external galaxies may be investigated using a model to generate the predicted number of stars as a function of apparent magnitude in any field in the galaxy. An implementation of such a model is explained in detail and is then tested against observations of M31. These data consist of several CCD images of several fields in M31 along the minor axis, with one field along a "diagonal". Additional data for 5 fields along the major axis was also made available.

Modelling of two galaxy components – the spheroid and the disk – is undertaken. A spheroid density normalization of 3.1×10^{-6} stars pc^{-3} at 10 kpc is derived for two of the spheroid fields. The data for the field along the diagonal gives a density approximately 1.5 greater than this, possibly implying that the spheroid of M31 is inhomogenous. The spheroid axial ratio can be constrained to between 0.4 and 0.7, values similar to previous works. The effective radius cannot be constrained as well because it has a much smaller effect on the observed number counts. It is also noted that changes in these parameters can compensate for changes in the density normalization.

Modelling the disk counts is more problematical – the reasons for this are discussed in some detail. The disk density normalization is found to be approximately 1.5×10^{-4} stars pc^{-3} at 10 kpc giving a disk to spheroid density ratio of about 48:1. Using models run over grids of scale height and scale length it is found that the scale height is limited to between 50 and 400 pc, the scale length constrained to between 5 and 7 kpc.

Table of Contents

List of Tables

List of Figures

Acknowledgements

I would like to thank my parents and family, for their continued love and support. Thanks to all the friends I've made in Vancouver: Brad and Kristine, Ted, Scott and Sally, James (especially for the use of his data), Dave (all of them! - especially Dave Woods for his galaxy counts), Andrew, Yiman, Steve, Remi, Greg, Sandra, and all the others. And finally thanks to Harvey Richer and Greg Fahlman for supervising this thesis and helping me along.

'I look at it like this,' he said. 'Before I heard him talk, I was like everyone else. You know what I mean? I was confused and uncertain about all the little details of life. But now,' he brightened up, 'while I'm still confused and uncertain it's on a much higher plane, d'you see, and at least I know I'm bewildered about the really fundamental and important facts of the universe.'

Terry Pratchett, Equal Rites

Chapter 1

Star Counts and Galactic Structure

1.1 Introduction

One of the most fundamental problems in the field of Galactic astronomy is that of stellar populations: that is, what is the number and type of kinematic and chemical components that make up our Galaxy and others. This problem has generated much debate and controversy amongst researchers, but has also led to some important discoveries about the nature and history of galaxies. This chapter will briefly review the main points in the history of this subject and how they relate to this thesis. The emphasis will be on the subject of star counts rather than on kinematical studies.

1.2 Early Studies of Galactic Structure

The first attempt to derive quantitative measurements of the Galaxy by counting stars in different areas of the sky was by William Herschel in the 18^{th} century. His work on "star-gauging" – counting the numbers of stars down to increasingly faint magnitudes – led him to conclude that the Galaxy was roughly elliptical (with an axial ratio of about 5:1) with the Sun near the center. At that time interstellar absorption was an unknown quantity and this, coupled with Herschel's assumption that all the stars were of the same brightness, led to this erroneous result. [1]

[1] See Mihalas & Binney 1981 for a more complete description and further references.

With the development of large telescopes and astronomical photography (which permitted much more accurate measurements of a larger number of stars) Kapteyn 1922 undertook a similar task, leading to a similar model of the galaxy. Kapteyn deduced from star counts and proper motion analyses that the Galaxy was a flattened spheroid, with the density of stars dropping to half the central value at about 800 pc in the plane and 150 pc perpendicular to the plane. This is now known to be rather too small because the model also did not include the effects of interstellar absorption. Kapteyn, whilst aware that absorption *could* be present, could find no direct evidence for it at that time.

In Kapteyn's model the Sun was close (650 pc) to the centre of the Galaxy. This was disputed by Shapley (see Shapley 1919, for example) on the basis of his analysis of the distribution of galactic globular clusters. Shapley proposed that the Sun was in the outer parts of the Galactic plane, about 15 kpc from the centre. Although this value is nearly twice as large as the currently accepted value, the idea was basically correct.

Support for Shapley's model of a large Galaxy with the Sun near the edge was provided by the dynamical studies of Lindblad 1927, who also proposed that the Galaxy may be composed of a number of components all rotating about an axis through the galactic centre and exhibiting various degrees of flattening depending on the speed of rotation. This dynamical reference was one of the first suggestions that the Galaxy may be composed of two or more physical components with distinct properties. Oort 1927, 1928 built on Lindblad's ideas to produce a more complete *kinematical* model of the galaxy, compatible with Shapley's.

Baade's 1944 study of M31 revealed the presence of two classes or *populations* of stars. Baade designated these as Population I (young objects in the spiral arms of galaxies, with colour-magnitude diagrams similar to those of open clusters) and Population II (older red stars found in the halo, and with globular cluster-like colour-magnitude diagrams). A

system of five populations (Blaauw 1965) was later considered by many to be necessary to provide a complete description of the Galaxy. However this figure is now viewed as unnecessarily high – usually only two populations, a thin disk-like configuration and a spheroidal halo, are used to model Galactic structure (Bahcall 1986). However there is some evidence for a third "thick disk" component (see §1.4).

Until quite recently population studies of the Galaxy concentrated mainly on analyzing samples containing detailed information on the spatial, kinematic and chemical abundances of a number of stars (see, for example, the references in §1.4). These types of studies usually share a common feature: the samples consist of stars within our Galaxy with well known properties (kinematics, distances, metallicities etc.). This means that sample size is often limited, and that samples can often be subjected to observational bias. For example, the data set of Carney, Latham & Laird 1989 is chosen from the Lowell Proper Motion Catalogue. Compared to other samples (e.g. Norris 1986) the halo stars in this set have an unusually large velocity dispersion in the radial direction, implying a bias against stars moving on more circular orbits. The stars in the sample are therefore kinematically biased but are unbiased in metallicity.

Because the sample sizes are generally small, they are susceptible to bias effects introduced by the presence of a few stars with extreme properties – for which there may be no *a priori* reason to remove from the sample. Further complications arise due to the fact that the metallicity and kinematics of a population can only be described by some form of distribution function: therefore there will always be an overlap between the two or more components.

1.3 Modern Star Count Analysis

Recently (as discussed in Bahcall 1986) the technique of using star counts has made a comeback – principally due to the advent of computer controlled machines to analyze photographic plates and CCD cameras capable of fast and accurate data acquisition.

When making observations of a particular field the final number of stars one sees (down to some limiting magnitude) comes from three sources: the density distribution of stars throughout the Galaxy, the distribution of stars with absolute magnitude (the luminosity function) and the interstellar absorption. Although the latter does not change the *number* of stars, it does change their apparent magnitude and therefore the observed luminosity function. One may formalize this and write that the number of stars, A, having magnitudes m ($m_1 \leq m \leq m_2$) in direction (ℓ, b) in a projected area $d\Omega$ is given by

$$A(m_1, m_2, \ell, b)d\Omega = \int_{m_1}^{m_2} dm' \int_0^\infty R^2 \rho(\ell, b, R, M)\Phi(M)d\Omega dR \qquad (1.1)$$

where $M = m' - 5\log R + 5 - \Theta(R)$. In this "fundamental equation of stellar statistics", ρ, Φ and Θ refer to the density and luminosity functions and the interstellar absorption in the field. ℓ and b are the Galactic longitude and latitude respectively. The density function, ρ, may also be a function of spectral type or absolute magnitude. For example, the scale height of stars in the disk varies from approximately 200 pc for the main-sequence dwarfs up to about 1 kpc for the red giants (Bahcall 1980). In addition the luminosity function is assumed to be independent of the density function and position.

The classical approach to solve this equation for ρ, Φ and Θ – given an appropriate set of data – is to invert it mathematically. The most common methods are those of $(m, \log \pi)$ (see, for example, Mihalas & Binney 1981), and that of Malmquist 1924, 1936. However these can be unstable mathematical procedures, especially when the sample is small (as is often the case), its photometry poor and the obscuration is patchy or

unknown (or both). It is often desirable to obtain the luminosity functions of stars of different spectral types, $\Phi(M, S)$. These are quite well defined and can be extracted from the data separately. However it is often necessary to solve for a *general* luminosity function $\Phi(M)$ to avoid reducing the sample size still further.

The alternative adopted by Bahcall & Soneira 1980, 1984 is to assume that the density distributions and luminosity functions are known, predict what the star counts (and colour distribution) should be, and compare this to the observations. This can be repeated with changes in the model parameters until a suitable match is found. This method is much simpler than the usual inversion techniques. However, the resulting model will probably not be unique, but it *will* determine the basic structural properties of the Galaxy. Bahcall & Soneira 1984 and Bahcall 1986 have used this model, with only two structural components (a disk and a spheroid), with considerable success in fitting the observations from a variety of observers in a multitude of fields in our Galaxy.

1.4 The Thick Disk

In recent years the existence of a third discrete component, usually referred to as a "thick disk", has been both proposed by some and been found unnecessary by others. The presence of a thick disk was first proposed by Gilmore & Reid 1983 who found an excess in the density distribution perpendicular to the galactic plane. Further evidence of a thick disk has also been claimed by, amongst others, Gilmore & Wyse 1985, Norris, Bessell & Pickles 1985, Rose 1985 and Carney, Latham & Laird 1989. However the original work by Gilmore & Reid has been criticised by Bahcall & Soneira 1984 who point out that the sample could be contaminated with giants, leading to the observation of an artificial thick disk. Bahcall 1986 reviews the case for the two component model, and finds the existence of a thick disk to be unnecessary.

Furthermore, Norris 1987 demonstrates that a four component model can fit the data – which implies that one can construct a model composed of almost any number of components, of which few (or none) may have any physical basis.

However a recent study by Majewski 1992 has shown that there appears to be a thick disk, and furthermore, that it is a spatially distinct entity. He uses photometry and proper motion studies of SA 57, calibrated with CCD photometry and claims the study is unbiased out to a distance of up to 25 kpc from the Galactic plane. He finds a sharp change in the stellar populations at a height of approximately 5.5 kpc, which he associates with the edge of the thick disk. The chemical and kinematical properties of this component are found to be quite distinct from the spheroid.

1.5 Stellar Populations and Galaxy Evolution

The presence, or lack, of a discrete thick disk will have significant effects on theories of galaxy formation. With no thick disk, a model of monolithic galactic collapse akin to that proposed by Eggen, Lynden-Bell & Sandage 1962 is plausible. In this model, the galaxy formed out of a cloud of gas in a uniform manner, the disk rotating faster as it collapsed and increased its angular momentum. If a thick disk is present then a slower accretion of "sub-units" (such as that favoured by Searle & Zinn 1978) would be preferred. After the formation of the disk the collapse of spheroid components would be much more independent and inhomogenous, possibly leading to a flat metallicity gradient in the outer parts of the galaxy.

If a thick disk is present, and if it has properties distinct from those of the spheroidal halo (as the results by Majewski 1992 seem to indicate), then its formation cannot have occurred as a smooth transition between the formations of the (thin) disk and the halo. Each of the three Galactic components may have formed separately from the others –

possibly the disk formed via a process similar to that proposed by Eggen, Lynden-Bell & Sandage 1962, whilst the halo formed "chaotically".

1.6 External Galaxies

A number of the problems mentioned in §1.3 can be overcome by examining external galaxies. In practice this usually means looking at the Andromeda Galaxy, M31, where individual stars can be resolved. This is the most luminous galaxy in our Local Group, and the third brightest in the sky (after the LMC and SMC). van den Bergh 1960 classifies its Hubble type as Sb I–II, making it very similar to our Galaxy (type Sb/c). The distance is well known – van den Bergh 1991 gives a mean distance (determined from a variety of methods) of 725 ± 35 Kpc. Walterbos & Kennicutt 1988 (hereafter WK88) have conducted an extensive study of the surface brightness profiles of M31, particularly the disk and spiral arm regions. They derive several parameters for the disk and spheroid that will be referred to in this work, usually as starting points for analysis.

To investigate stellar populations in M31 it was decided to adopt an approach similar to Bahcall & Soneira – that is, assume a density distribution and luminosity function and predict the star counts for various fields in M31 by integrating from the *outside* into the galaxy. The model is fairly straightforward – once the projection effects due to the inclination are accounted for, the distance of the field from the centre of the galaxy can be found and a "back-bearing" can be obtained to find an effective "ℓ" and "b". The integration then proceeds in a manner similar to the Bahcall – Soneira model except now the apparent magnitude is given by $M = m - 5\log(D \pm R) - \Theta + 5$ where D is the distance to M31 and R the distance from the plane of M31 (R is added or subtracted from D depending on whether the integration is proceeding away from or towards the observer).

The terminology used by different works to describe various galactic components can be confusing at times. In this work the *spheroid* will be taken to mean the extended distribution of stars in a galaxy – it will not be referred to as the bulge or halo (the latter often referring to an extended (R^{-2}) distribution of dark matter).

1.7 Star Counts in External Galaxies

Star counts in M31 have been performed by Reddish 1962, van den Bergh 1966 and Berkhuijsen & Humphreys 1989. However these are not "counts" in the same sense as the method discussed here – they derived luminosity functions from counts of OB associations and individual OB stars.

Pritchet & van den Bergh 1994 (hereafter PvdB94) have also performed a study of the stellar populations of M31 using star counts. However after performing the star counts and conducting the incompleteness tests they convert these numbers to a surface brightness to determine the halo parameters. They achieve a good fit to the $r^{\frac{1}{4}}$ law and also note that the maximum disk contribution is approximately 40% at a minor axis distance of 15′. They conclude that a single de Vaucouleurs law with a minor axis effective radius of 1.3 kpc can fit the spheroid from $r = 200$ pc all the way out to $r = 2$ kpc. From analysis of fields along the "diagonal" they derive an axial ratio of 0.55 ± 0.05. This is fairly consistent with the values of 2.0 kpc and 0.63 derived by WK88.

Chapter 2

Observations and Data Reduction

2.1 Introduction

Any external galaxy model must be tested against observations of real galaxies. In this work, observations of several fields in M31 were used as a test of the model. These observations came from a program originally proposed by Fahlman & Richer (private communication) and combined with a project by Christian & Heasley (private communication).

The data set consists of three nights of observation of globular clusters in M31. These objects take up a very small area of the frame (the typical diameter is less than 10″) and can easily be masked out of the analysis procedure. The total amount of data available in this set is quite large but of variable quality: only six fields were picked for study and are discussed in this chapter. These fields lie mainly along the south east minor axis, with one lying due east of the galaxy along a "diagonal".

Additionally the results of data from five fields along the south west major axis were kindly made available by Brewer (private communication). Although these data were obtained with a very different purpose in mind they do lend themselves quite well for use in star count analysis.

This chapter will describe the observations and data reduction procedures used to analyze the first six fields. Interpretation of the results and comparison with the external galaxy model will be discussed in chapters 4 and 5.

2.2 Observations

The data used in this work were obtained by Fahlman and Christian at CFHT [1] on the nights of 1990 August 16/17, 1990 August 17/18 and 1990 August 18/19 (designated as nights 1 to 3 in the following discussion) using HRCam and the SAIC2 CCD. This device has a size of 1024 × 1024 pixels with a scale of 0.″13 per pixel when used with the High Resolution Camera.

Table 2.1 lists the fields used in this work, identified by the globular cluster in the field (column 1, Sargent *et al.* 1977). Coordinates (epoch 2000.0) are given in columns 2 and 3. The projected distance from the centre of M31 ($\alpha_{2000} = 0^h42^m44.5^s$, $\delta_{2000} = +41° 16'29''$) – essentially the impact parameter, b – is given in column 4 in kpc. The number of V and I frames are given in columns 5 and 6 along with the exposure times (in seconds) as the second number. The size of each field was 1014 × 1023 pixels, or 132″ × 133″ , after preprocessing. At the distance of M31 each field is ≈ 420 pc on a side.

In addition, the five major axis fields made available by Brewer (private communication) are listed (B1, B2, B3, B4 and B5). These were obtained with FOCAM at CFHT. These fields are substantially larger than the HRCam fields at 7′ × 7′. They are more fully discussed later in this chapter.

Table 2.2 lists the standard star observations for each night. Positions (epoch 2000.0) are given in columns 2 and 3, exposure times for each standard frame (in seconds) are given in column 4 (V) and 5 (I). The M92 standards consist of 10 to 12 stars in the outer regions of M92. Magnitudes in V and I were taken from Landolt 1992, except for the M92 stars whose data came from the work of the "Kitt Peak consortium standards in M92" (Christian *et al.* 1985, Heasley and Christian 1986).

[1]The Canada-France-Hawai'i Telescope (CFHT) is operated by the National Research Council of Canada, le Centre National de la Recherche Scientifique de France, and the University of Hawai'i.

Table 2.1: List of observed fields in M31

ID	α_{2000}	δ_{2000}	b	V frames	I frames	Night
G213	$0^h43^m14.6^s$	$41^\circ\,07'\,23''$	2.2	2×300	5×120	3
G263	44 03.3	41 04 57	3.9	1×450	1×450	3
G302	45 14.9	41 06 23	6.2	3×1000	4×400	1
G312	45 58.8	40 42 32	10.5	6×600	5×300	2
G352	50 10.0	41 41 01	18.2	3×600	3×300	3
G355	51 33.9	39 57 34	26.8	1×450	—	3
B1	41 40.4	40 59 00	4.5	9×600	7×300	
B2	41 12.7	40 50 41	6.6	6×600	4×300	
B3	40 21.9	40 36 24	10.3	6×600	4×300	
B4	39 23.8	40 14 32	15.4	6×600	3×300	
B5	35 41.9	39 29 03	28.4	4×600	5×300	

Table 2.2: List of standard star frames

Field	α_{2000}	δ_{2000}	V exp.	I exp.	Night
SA93–317	$01^h54^m38^s$	$+00^\circ\,43'\,00''$	5	2	1
SA93–424	01 55 26	+00 56 43	5	2	1
Feige 16	01 54 08	−06 42 54	5	5	1
M92	17 17 07	+43 08 11	60	60	1
M92	17 17 07	+43 08 11	60	60	2
SA113–492	21 42 28	+00 38 21	2	2	2
PG1633+099	16 35 24	+09 47 50	20	10	2
SA93–317	01 54 38	+00 43 00	5	2	3
SA93–424	01 55 26	+00 56 43	5	2	3
Feige 16	01 54 08	−06 42 54	5	5	3

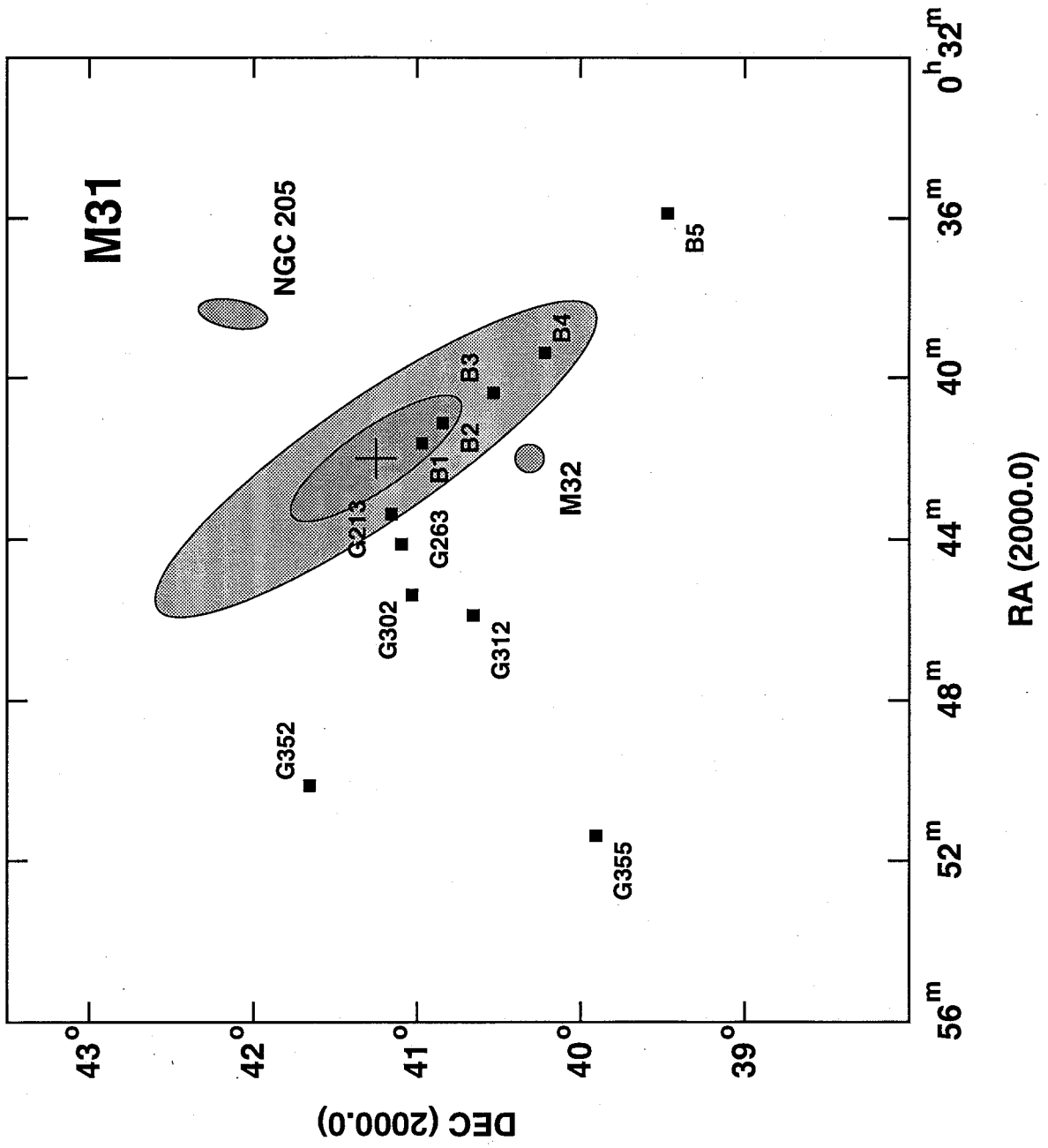

Figure 2.1: A map of M31 showing the locations of the fields listed in Tables 1 and 2 (the black squares). Also shown are the companions M32 and NGC 205. The shading in the figure is only representative and does not indicate a true optical size. The centre of M31 – shown by the small cross – is at $\alpha_{2000} = 0^{\rm h}42^{\rm m}$ and $\delta_{2000} = 41^\circ\,16'$ in this figure.

2.3 Data Reduction

The frames were preprocessed (bias subtracted and flat fielding) using IRAF [2]. If three or more frames were available for a particular field they were combined using the **sigma clip average** option of the IRAF task **imcombine**. In this procedure each pixel of the final frame is the average of the same pixel in the input frames, but with deviant pixels excluded. This has the effect of increasing the S/N ratio and successfully removing most cosmic rays. If only two frames were available they were averaged and the cosmic rays removed with the **cosmicray** task in IRAF. This was also quite successful, and was also the method used to remove cosmic rays if only one frame was available. The images were then trimmed to remove several columns of bad pixels along one edge.

In a few cases the same field had been observed on two or more nights. In these cases the frames from the best night (most frames, better seeing) were combined and used. Frames taken on different nights were not combined because of small rotations between the frames. Note that in the case of the G213 field both V and I data were available but only the V data is presented here. The individual and combined I images suffer from extreme crowding and large background variations due to their proximity to the centre of M31.

After preprocessing and combining (where appropriate) each image was reduced using the DAOPHOT software package (Stetson 1987). DAOPHOT automates the process of finding objects on the image, identifying them as stars and measuring their magnitudes. A certain amount of user interaction is required to set the point spread function (PSF) for the image. In practice the ALLSTAR program in the latest version of the DAOPHOT software was used in this analysis.

The output from the reduction of each image is a list of star positions and instrumental

[2]Image Reduction and Analysis Facility (IRAF), a software system distributed by the National Optical Astronomy Observatories (NOAO).

magnitudes. The final steps are to remove stars that are (a) too near (within 100 pixels of) the globular cluster on the image; (b) stars on and around the HRCam guide star on the edge of the image (typically bright and saturated); and (c) remove stars that are obviously not stars at all – on a few of the final images one or two bright galaxies are present which the DAOPHOT `find` detection routine did not classify correctly.

2.3.1 Standard Star Frames

Standard star frames (see Table 2.2) were preprocessed in the same way. For all the standards (except for the M92 field) it was necessary only to measure the aperture magnitude (see the §2.4.2, below). The M92 standard field was sufficiently crowded to require a full reduction procedure. This enabled the "non" standard stars to be removed (subtracted) from the frame. Although this leads to noisier images (in the sense that some stars will not subtract out perfectly and will leave residual effects behind) it is necessary to do this to get uncontaminated magnitudes for large apertures.

2.4 Calibration

From Table 2.2 one can see that the available standards were quite limited – the low number of standards for each night precluded the calculation of extinction coefficients. Standard CFHT coefficients of $\alpha_V = 0.13$ and $\alpha_I = 0.05$ were used instead. Checks were made, however, to ensure that these were consistent with the data. This turned out to be the case. The data are also consistent with a zero colour coefficient, though a non-zero coefficient cannot be ruled out entirely.

2.4.1 DAOGROW

The DAOGROW program was used to determine aperture magnitudes for both the standard stars and all the secondary standards on the individual images. The usual calibration procedure is to use an aperture magnitude and a profile fitting magnitude (PSF magnitude) for the same secondary standards to derive an offset, and to correct the PSF magnitudes of all the stars on the image to the aperture photometry scale. If the frame is crowded then there may be few (or no) stars that are sufficiently isolated for this to work properly. In this case two aperture magnitudes can be used (at radii of, say, 3 and 10 pixels). The magnitude in the smaller aperture can be found for many stars, and the magnitude in the larger one measured for selected uncrowded stars to get a magnitude that includes all the stellar light in the wings of the profile. These two corrections can then be combined to provide a single aperture correction. DAOGROW (Stetson 1990) takes this procedure one step further. It derives a "total magnitude" for a star using a combination of the empirical curve of growth and an analytical function fitted to the curves of growth of all the specified stars on the image. In this way it uses all the available information about the stellar profile – not just samples of the data at one or two radii. This total magnitude is then used as the real instrumental magnitude of the star and is compared to the PSF magnitude to derive an offset.

2.4.2 Standard stars

Table 2.3 lists standard star magnitudes and $V - I$ colours. Reference 1 is Landolt 1992; reference 2 is from the Kitt Peak consortium standards in M92 (Christian *et al.* 1985, Heasley and Christian 1986). Instrumental aperture magnitudes were obtained using DAOGROW and corrected for exposure time and extinctions (using CFHT standard values). Extinction coefficients were hard to measure due to the paucity of

Table 2.3: List of standard star magnitudes

Standard	V	σ_V	$V-I$	σ_{V-I}	Reference
Feige 16	12.406	0.0013	–0.001	0.0021	1
SA93–317	11.546	0.0007	0.592	0.0008	1
SA93–424	11.620	0.0009	1.058	0.0008	1
SA113–492	12.174	0.0033	0.684	0.0053	1
SA113–493	11.767	0.0039	0.824	0.0039	1
SA113–495	12.437	0.0024	1.010	0.0057	1
PG1633+099	14.397	0.0025	–0.212	0.0111	1
PG1633+099A	15.256	0.0036	1.015	0.0111	1
M92–4	14.618	0.0140	0.950	0.0380	2
M92–5	16.052	0.0090	0.590	0.0090	2
M92–6	16.331	0.0210	–0.123	0.0110	2
M92–7	16.437	0.0200	–0.127	0.0220	2
M92–8	15.932	0.0210	0.653	0.0240	2
M92–9	16.986	0.0100	1.311	0.0300	2
M92–10	14.036	0.0100	0.933	0.0200	2
M92–11	15.146	0.0230	1.152	0.0280	2
M92–12	15.982	0.0270	0.844	0.0180	2
M92–13	15.078	0.0180	0.681	0.0240	2
M92–21	17.925	0.0090	0.636	0.0170	2
M92–22	17.542	0.0150	0.680	0.0260	2
M92–23	16.791	0.0230	0.771	0.0430	2

standards. Plotting the magnitude offset as a function of airmass showed that the standard CFHT values of the extinction coefficients were at least consistent with the data. There is no convincing evidence for a colour term on any of the three nights. The number of M92 standards that were usable depended on the precise field and seeing conditions and therefore varied from night to night.

Night 1

Standard stars available on this night included SA93–317, SA93–424, Feige 16, and six of the M92 standards (6, 7, 8, 9, 12 and 23). The plot of standard magnitude (V) minus aperture magnitude (measured using DAOGROW , V_{ap}) against standard $V - I$ is shown in figure 2.2. M92 standards are plotted as filled circles, the SA93 stars as triangles and Feige 16 as a square. Panel (c) of the figure shows that there is no significant colour effect. The zero points are $\langle V - V_{ap} \rangle = -0.9471 \pm 0.0281$ and $\langle I - I_{ap} \rangle = -1.0712 \pm 0.0936$.

Night 2

Available standards on night 2 included SA113–492, SA113–493, SA113–495, PG1633+099, PG1633+099A and 11 M92 standards (4, 5, 7, 8, 9, 10, 11, 13, 21, 22 and 23). Figure 2.3 shows the plot of standard minus instrumental magnitude as a function of standard $V - I$. M92 standards are plotted as filled circles, the SA113 stars as squares and the PG1633+099 stars as triangles. M92 standard 21 was not measured in V; standard 10 was not measured in I (that is, the star was either too crowded or the neighbours did not subtract cleanly enough for a good curve of growth to be measured). Again there is no significant colour term. The zero points are: $\langle V - V_{ap} \rangle = -1.0044 \pm 0.0734$ and $\langle I - I_{ap} \rangle = -1.0873 \pm 0.0386$.

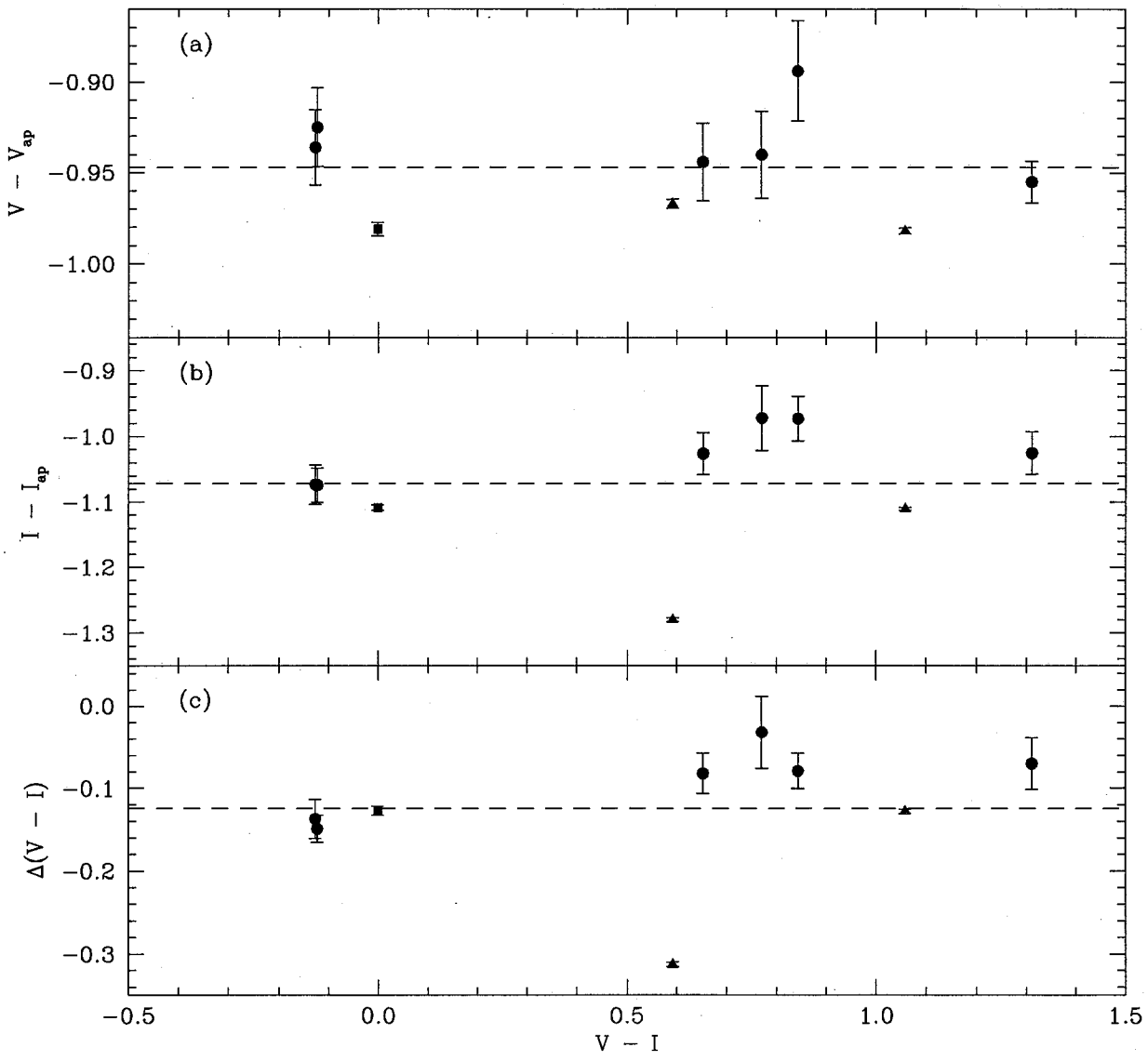

Figure 2.2: This figure shows the zero point shifts (the difference between standard magnitude (V) and instrumental aperture magnitude (V_{ap})) for the standard stars for night 1, plotted against standard $(V-I)$ for the V and I measurements (panel (a) and (b) respectively). Panel (c) plots the colour difference $\Delta(V-I) = (V-I)_{ap} - (V-I)$. The M92 standards are plotted as filled circles; SA93 stars as triangles and Feige 16 as a square. The broken horizontal line shows the mean value in each case.

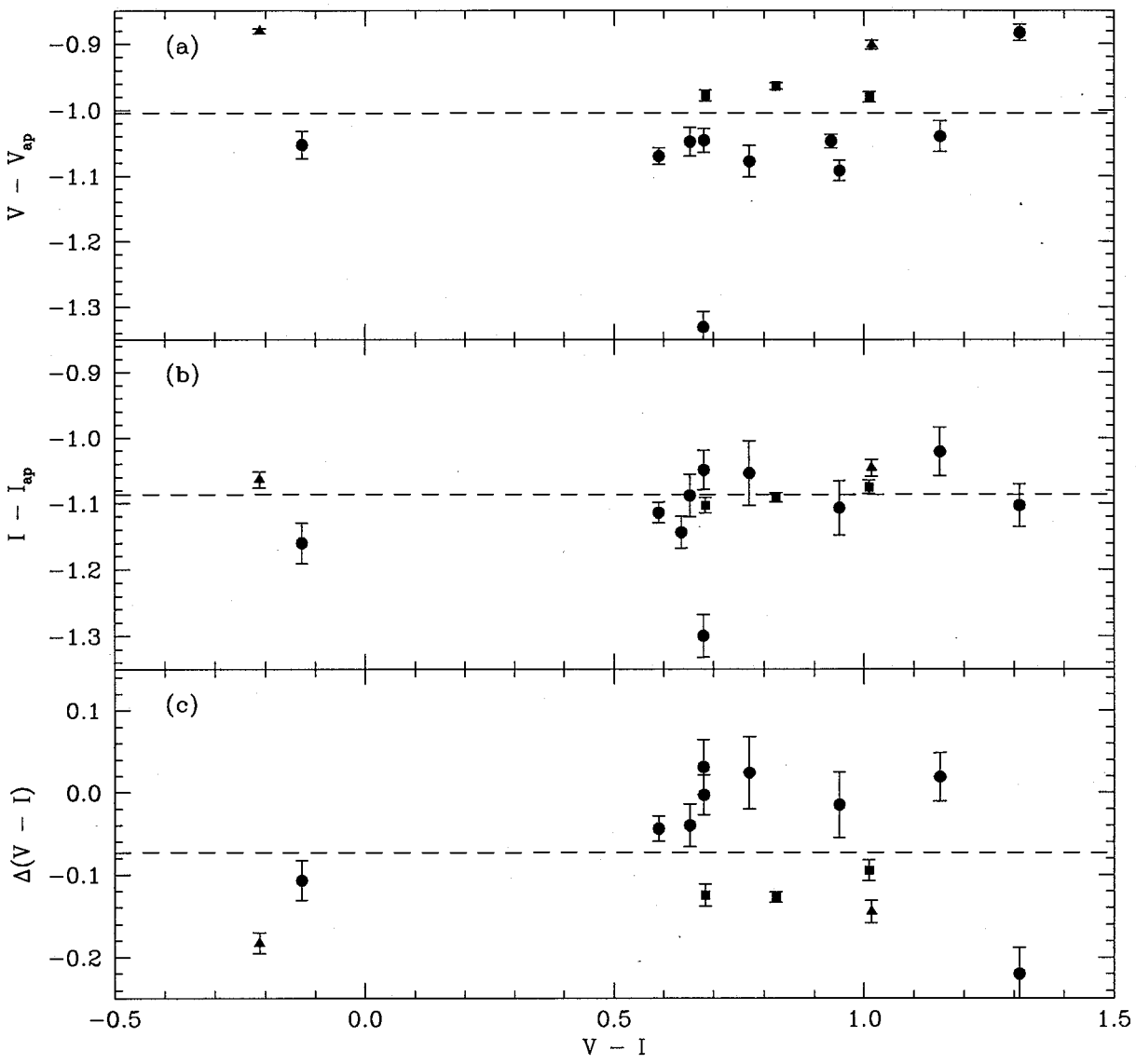

Figure 2.3: This figure shows the zero point shifts for the standard stars for night 2, plotted against standard $(V-I)$. The M92 standards are plotted as circles; SA113 stars as squares and PG1633+099 stars as triangles. The broken horizontal line shows the mean value in each case.

Night 3

Only 3 standards were available this night: Feige 16, SA93–317 and SA93–424. No colour term is evident in figure 2.4, which shows the zero point shift as a function of $V-I$. The zero points are: $\langle V - V_{ap} \rangle = -0.9600 \pm 0.0164$ and $\langle I - I_{ap} \rangle = -1.1243 \pm 0.0652$

2.4.3 Secondary Standards

For each frame secondary standards were selected from the final photometry lists using the criteria that they were relatively uncrowded and bright but not saturated (a selection method similar to choosing PSF stars). All the stars in the photometry list except these ones were then subtracted from the frame using DAOPHOT. The instrumental aperture magnitudes of these stars on the subtracted frames were measured using the DAOGROW program for several radii. The sample was further "pruned" by selecting stars with curves of growth that flattened out reasonably well at large radii. Typically 7 or 8 stars survived this process to provide well measured aperture magnitudes. These aperture magnitudes were then compared with the profile fitting magnitudes (from ALLSTAR) to provide corrections from the one to the other. Once again, no colour term was found to be significant. By summing these corrections (PSF magnitude to aperture magnitude) with the shifts from equations 2.1, 2.2 and 2.3 (aperture magnitude to standard magnitude) and adding terms for the extinction with air mass and for the exposure time, a set of final zero point shifts was derived. These are shown in Table 2.4, for both the V and the I frames, along with the formal errors.

2.5 Incompleteness Tests

The final observed luminosity function for each field will suffer from incompleteness, *i.e.,* not all stars that are actually there may have been found and photometered. This

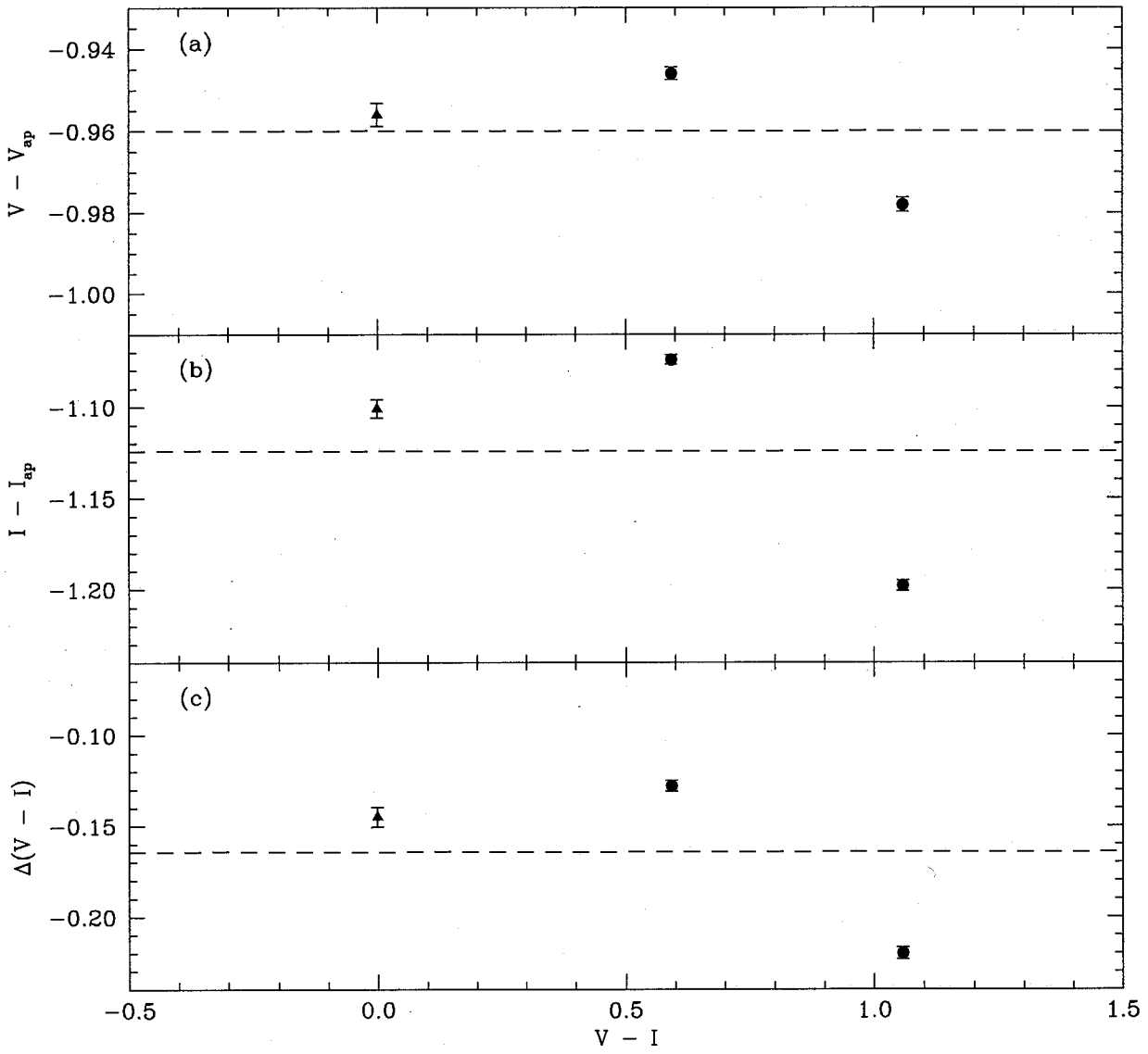

Figure 2.4: This figure shows the zero point shifts for the standard stars for night 3, plotted against standard $(V - I)$. SA93 stars are plotted as filled circles and Feige 16 as a triangle. The broken horizontal line shows the mean value in each case.

Table 2.4: Final calibration zero points

Field	z_V	σ_{z_V}	z_I	σ_{z_I}
G213	4.1972	0.0536	—	—
G263	4.8804	0.0523	4.5339	0.0840
G302	5.6647	0.0919	4.6389	0.0989
G312	5.2903	0.1021	4.4936	0.0599
G352	5.0670	0.0792	4.0952	0.1227
G355	4.7995	0.0623	—	—

problem gets worse with fainter magnitudes but can be partially alleviated by adding artificial stars to the image and re-reducing it in exactly the same way as the original. By comparing the number of artificial stars added in to those recovered it is possible to estimate how many stars are being missed as a function of magnitude. A small number of stars are added to the original image to keep the crowding problems at the same level. This procedure is then done several times to build up a statistically significant test sample. Typically in this work 20 sets of 100 stars were added independently to each frame so that errors in the incompleteness ratios could be found. These incompleteness ratios can be used to correct the observed counts. A very thorough description of the process is found in Drukier *et al.* 1988 and also in Bergbusch 1993.

2.6 Observed Luminosity Functions & Colour-Magnitude Diagrams

The observed luminosity function will be contaminated by two effects – foreground stars belonging to our own Galaxy and background galaxies in the field. The latter is not a large problem in disk fields due to the increased absorption and much larger numbers of stars, but visual inspection of such images often revealed large, obvious background galaxies. These were masked out of the data reduction in the same way as the globular clusters.

The number of foreground stars in various fields has been estimated by Ratnatunga & Bahcall 1985 using the standard Bahcall and Soneira Galaxy model (Bahcall & Soneira 1980). Figure 2.5(a) shows this model calculation compared to a version of the code (called BSM) written during the development of the External Galaxy Model described in Chapter 3. The new BSM code reproduces the Ratnatunga and Bahcall results very well. An attempt was made to run this model using exactly the same parameters but because of the large number of parameters this was not possible. This may account for the slight discrepancies between the two models.

Figure 2.5(b) compares the same BSM model used above with background field data from the study of the halo of M31 by PvdB94. The BSM model fits the data *very* well for magnitudes $V < 22.25$ and is used to generate all the estimates of foreground contamination in this work.

At fainter magnitudes the chief source of contamination is from background galaxies that have been mis-identified as stars. An attempt was made to remove galaxies explicitly using a variety of image classification methods. This was found to be unsatisfactory due to the low signal to noise ratio at these faint magnitudes.

It was decided to remove background galaxies from the luminosity functions (LFs) in a statistical sense, rather than from the images themselves. There have been several studies of galaxy counts but the majority of them utilize the I and R bands – for this work V data is required. Fortunately deep galaxy counts in V have recently been made by Woods, Fahlman and Richer 1995 who give the following relation for the number of galaxies per 0.5 magnitude bin per square arc minute:

$$\log N = 0.41V - 9.19 \tag{2.1}$$

This relation is plotted in figure 2.6, together with the BSM model prediction for the foreground stars, and with the PvdB94 background field data. The fit of this relation to

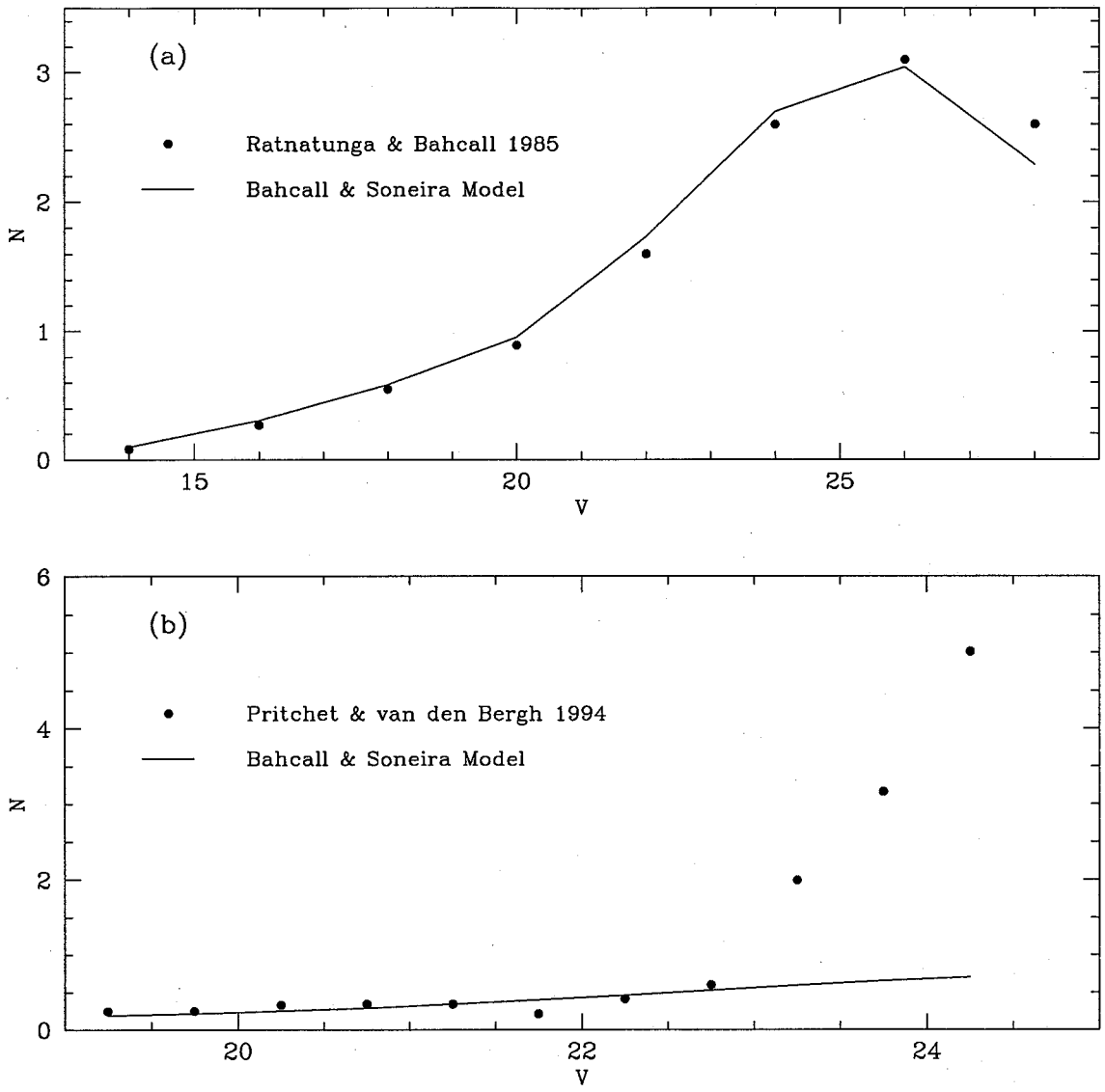

Figure 2.5: (a) A comparison of the Ratnatunga and Bahcall 1985 model (filled circles) and the BSM model described in the text (solid line). N is the number of stars per 2 magnitude bin. (b) A comparison of the PvdB94 background data with the BSM model. The fit to the brighter magnitudes ($V < 22.75$) is very good. N is the number of stars per 0.5 magnitude bin.

Table 2.5: Contaminant levels for M31

V	Stars	Galaxies	V	Stars	Galaxies
17.0	0.53	0.03	22.5	2.32	5.07
17.5	0.61	0.05	23.0	2.62	8.13
18.0	0.69	0.07	23.5	2.92	13.03
18.5	0.76	0.12	24.0	3.19	20.89
19.0	0.84	0.19	24.5	3.41	33.50
19.5	0.95	0.30	25.0	3.56	53.70
20.0	1.10	0.48	25.5	3.63	86.20
20.5	1.27	0.77	26.0	3.62	138.04
21.0	1.49	1.23	26.5	3.52	221.31
21.5	1.74	1.97	27.0	3.33	354.81
22.0	2.02	3.16	27.5	3.05	568.85

the faint end of the PvdB94 data is quite good.

Table 2.5 lists these galaxy counts (scaled to the area of the "G" fields of 4.68 square arc minutes) along with the foreground star counts. In the analysis of the spheroid component (Chapter 4) the galaxy corrections are only applied for bins $V > 20.5$ (where there is more than one galaxy to account for). In the disk analysis (Chapter 5) it is assumed that no faint galaxies can be seen through the disk, and this correction is not applied. It should also be noted that in Chapter 4, when the External Galaxy Model is compared against these corrected LFs, the "goodness of fit" criterion includes a correction for these contaminants. Since the bins that have been corrected for galaxy contamination are also those with a large errors in the number counts (because they are faint) these corrections do not play a large role in the analysis.

Figure 2.7 shows the observed V luminosity functions for the six fields. The thick vertical line in each panel indicates the magnitude at which the completeness of the sample is 50%, as obtained from incompleteness tests. These luminosity functions are tabulated in Table 2.6, which does *not* incorporate the foreground and background subtractions. The

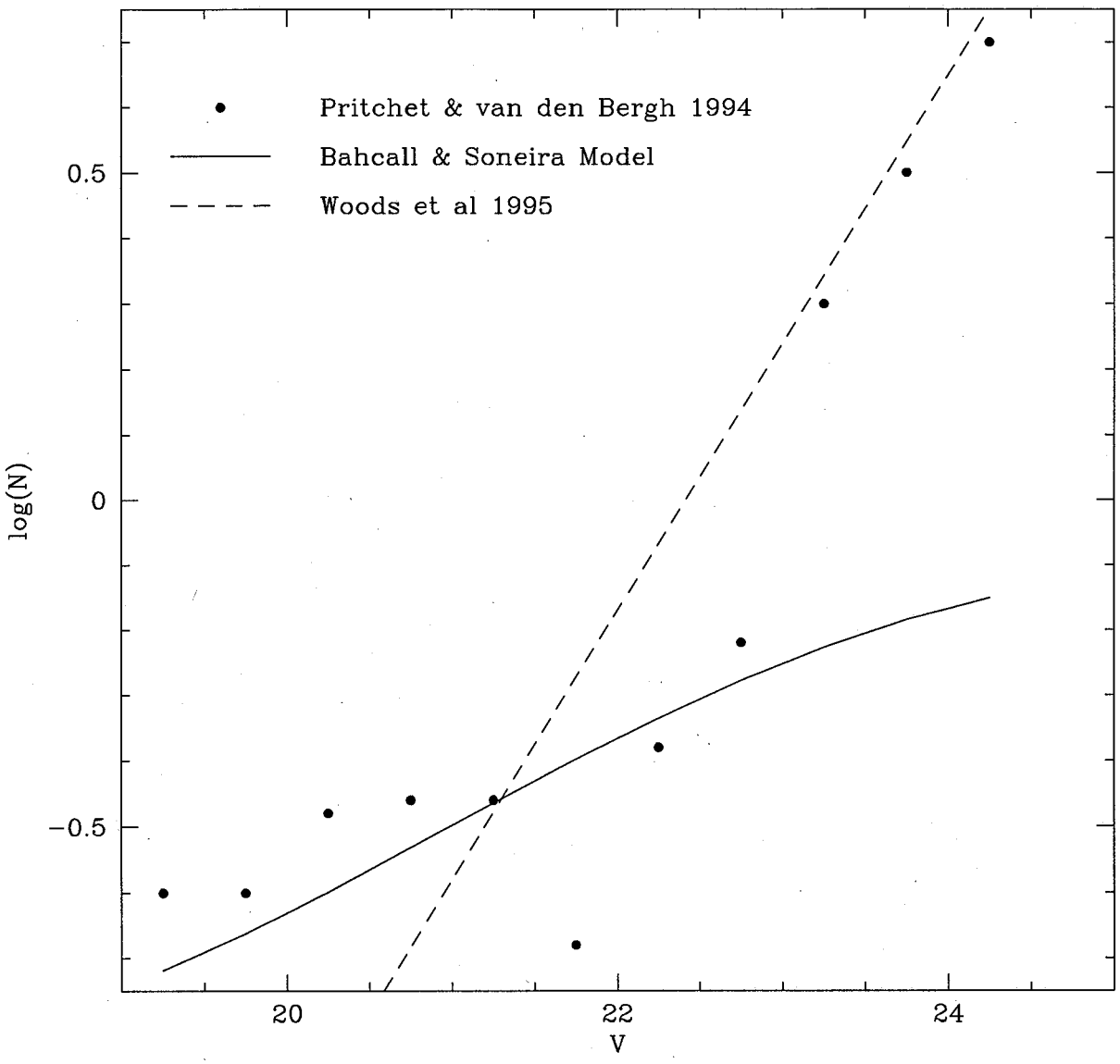

Figure 2.6: Estimate of background galaxy counts (per square arc minute) (dashed line) from Woods, Fahlman and Richer 1995, together with the PvdB94 background data (filled circles) and the BSM model prediction (solid line). At $V \approx 21.25$ there are equal numbers of foreground stars and background galaxies.

counts in this table are the completeness corrected counts in that field (0.0013 square degrees) in a 0.5 magnitude bin centered at the magnitude given in column (1). The corresponding errors (σ) are a combination of (a) the standard deviation of the mean of the counts in each bin, as measured over the 20 incompleteness tests, (b) the Poisson counting errors in each bin for each test, and (c) the error in the incompleteness fraction.

Figure 2.8 shows the colour-magnitude diagrams for the four fields with the best V and I data: G263, G302, G312 and G352. These diagrams were constructed by matching together the V and I photometry lists of each field. Similar diagrams for the G213 and G355 fields are not shown. In the former case there is too much crowding and background variation across the frame; in the latter no I frame was obtained.

2.7 The Brewer Major Axis Fields

To facilitate the analysis of the disk parameters Brewer (private communication) kindly made available V and I data from five fields along the major axis, taken at CFHT using FOCAM. These "B" fields (as they will be referred to) are approximately ten times larger than the "G" fields at $7' \times 7'$ in size. Additional information is given in Table 2.2. Data is also available in two narrow band filters centered around CN and TiO absorption features respectively. Only stars with a measured V and I magnitude are included in this discussion – the additional selection procedure of including stars only measured in *all* of the four filters was not applied as it was felt this would place unnecessary restrictions on the data sample.

Figure 2.9 shows (I,$V-I$) CMDs for each of the five Brewer fields. The B1 and B4 CMDs show a fairly "clean" disk population – the tip of the giant branch is clearly delineated, as is the form of the giant branch down to $V \approx 22$. The situation is more complex for B2 and B3 – there appears to be a substantial blue component at $V-I < 0.6$.

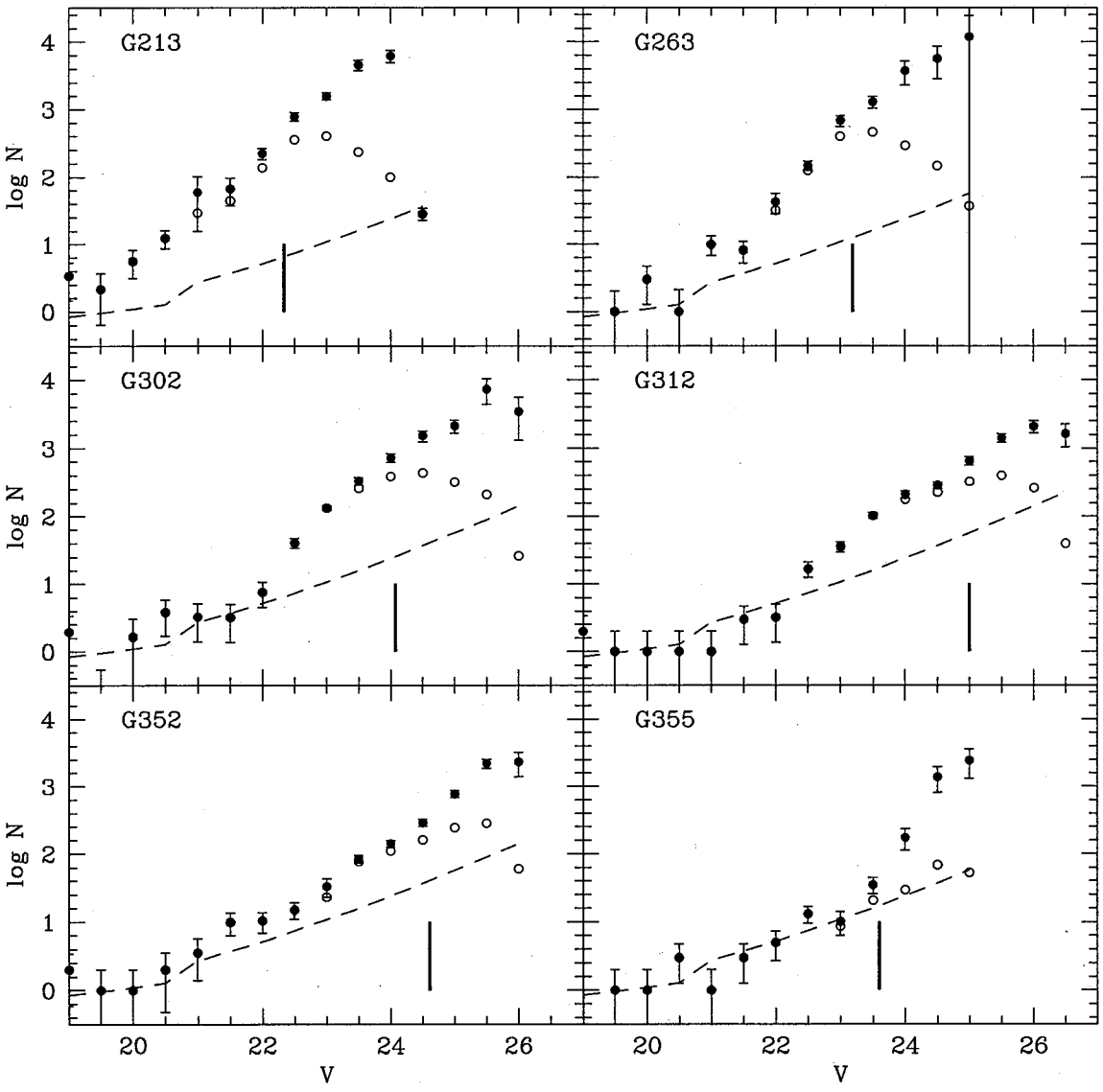

Figure 2.7: The observed V band luminosity functions for the fields G213, G263, G302, G312, G352 and G355 (filled circles). The bins are 0.5 mag wide and the ordinate is the logarithm of the number of stars in the fields per 0.5 magnitude bin at that magnitude. The open circles are the raw counts, not corrected for completeness. The dashed line is the contribution from foreground stars and background galaxies as described in the text. The thick vertical bar indicates the 50% completeness level.

Table 2.6: Observed "G" field V luminosity functions.

V	G213	σ	G263	σ	G302	σ
19.0	3.40	1.94	0.00	0.00	1.95	1.45
19.5	2.15	1.51	1.00	1.00	0.10	0.44
20.0	5.65	2.50	3.00	1.73	1.65	1.41
20.5	12.40	3.69	1.00	1.10	3.80	2.10
21.0	59.00	43.20	10.00	3.20	3.25	1.86
21.5	66.67	29.15	8.15	2.90	3.20	1.84
22.0	225.40	42.75	42.73	14.55	7.65	3.08
22.5	790.23	114.01	148.93	23.52	40.75	6.73
23.0	1579.01	196.32	682.94	125.90	132.75	11.77
23.5	4580.08	791.44	1302.23	261.00	330.97	44.47
24.0	6246.87	1280.88	3765.73	1491.29	728.43	106.60
24.5	28.50	5.89	5709.30	2850.74	1520.52	277.75
25.0	—	—	12032.26	12202.14	2123.33	445.03
25.5	—	—	—	—	7356.38	2993.94
26.0	—	—	—	—	3440.79	2122.12
26.5	—	—	—	—	—	—

V	G312	σ	G352	σ	G355	σ
19.0	2.00	1.41	2.00	1.41	0.00	0.00
19.5	1.00	1.00	1.00	1.00	1.00	1.00
20.0	1.00	1.00	1.00	1.00	1.00	1.00
20.5	1.00	1.00	2.00	1.52	3.00	1.73
21.0	1.00	1.00	3.55	2.16	1.00	1.00
21.5	3.00	1.73	10.00	3.60	3.00	1.73
22.0	3.20	1.84	10.40	3.46	5.00	2.31
22.5	16.75	4.14	15.05	4.08	13.10	3.71
23.0	35.95	6.11	33.29	9.97	10.15	3.83
23.5	103.20	10.28	84.27	10.57	35.14	9.51
24.0	210.65	25.36	140.61	16.00	172.57	59.53
24.5	288.62	32.57	292.46	35.11	1389.11	578.15
25.0	657.88	94.63	771.09	97.26	2465.12	1141.90
25.5	1420.03	205.56	2208.30	349.19	—	—
26.0	2096.40	414.36	2330.77	924.33	—	—
26.5	1647.30	608.11	—	—	—	—

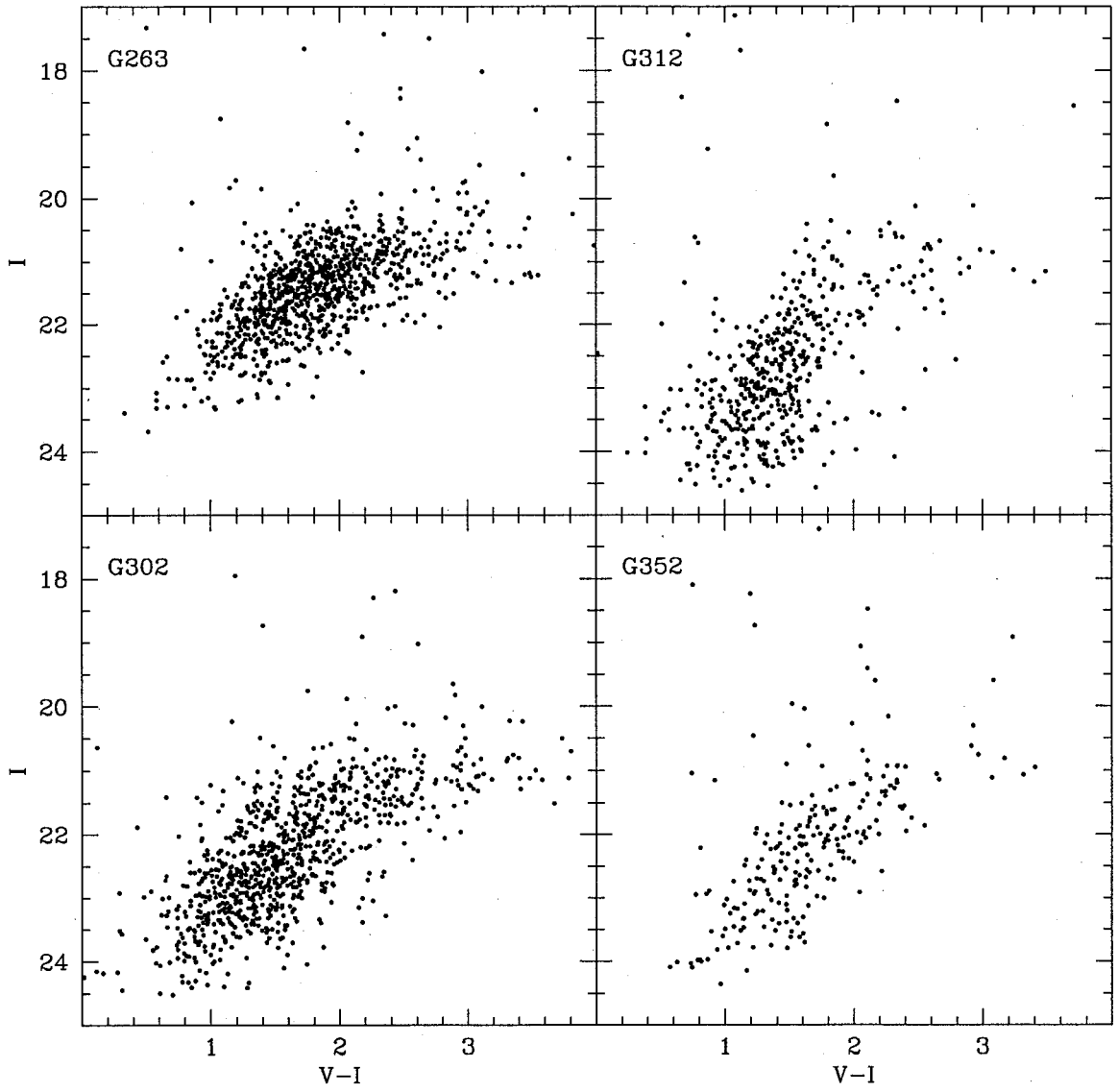

Figure 2.8: Colour magnitude diagrams in $(I, V-I)$ for the G263, G302, G312 and G352 fields.

This is especially noticeable in B3 where there is also a comparative excess of stars slightly above the giant branch at $I \approx 20$, $V-I \approx 1.8$. This may be attributed to the presence of a younger spiral arm component which may be hard to remove in the modelling described in Chapter 5. WK88 avoid this problem by excluding these regions from their fit to surface brightness, an option that is not available here. The B5 field has many fewer stars, appearing to be very much like a spheroid field. However appearances can be deceptive as the analysis in Chapters 4 and 5 will show.

Table 2.7 lists the observed LFs for the B fields, corrected for the difference in areas between the FOCAM and HRCAM fields by a factor 0.10022, but not corrected for foreground or background contamination. The units are stars per 0.5 magnitude bin per 0.0013 square degrees at a magnitude centered on the magnitude given in column (1). Figure 2.10 plots these LFs along with the foreground correction from Table 2.5. The background galaxy counts are not included in this plot – it is assumed that faint galaxies cannot be seen through the disk, a fact borne out by examination of the images. In the B2 and B3 fields the removal of the component blueward of $V - I = 0.6$ did not lead to a substantial reduction in the number of stars. These modified LFs are also listed in Table 2.7 (columns 4 and 6) as "B2(R)" and "B3(R)". They are plotted in figure 2.10 as open circles. Incompleteness fractions were not available for this data set.

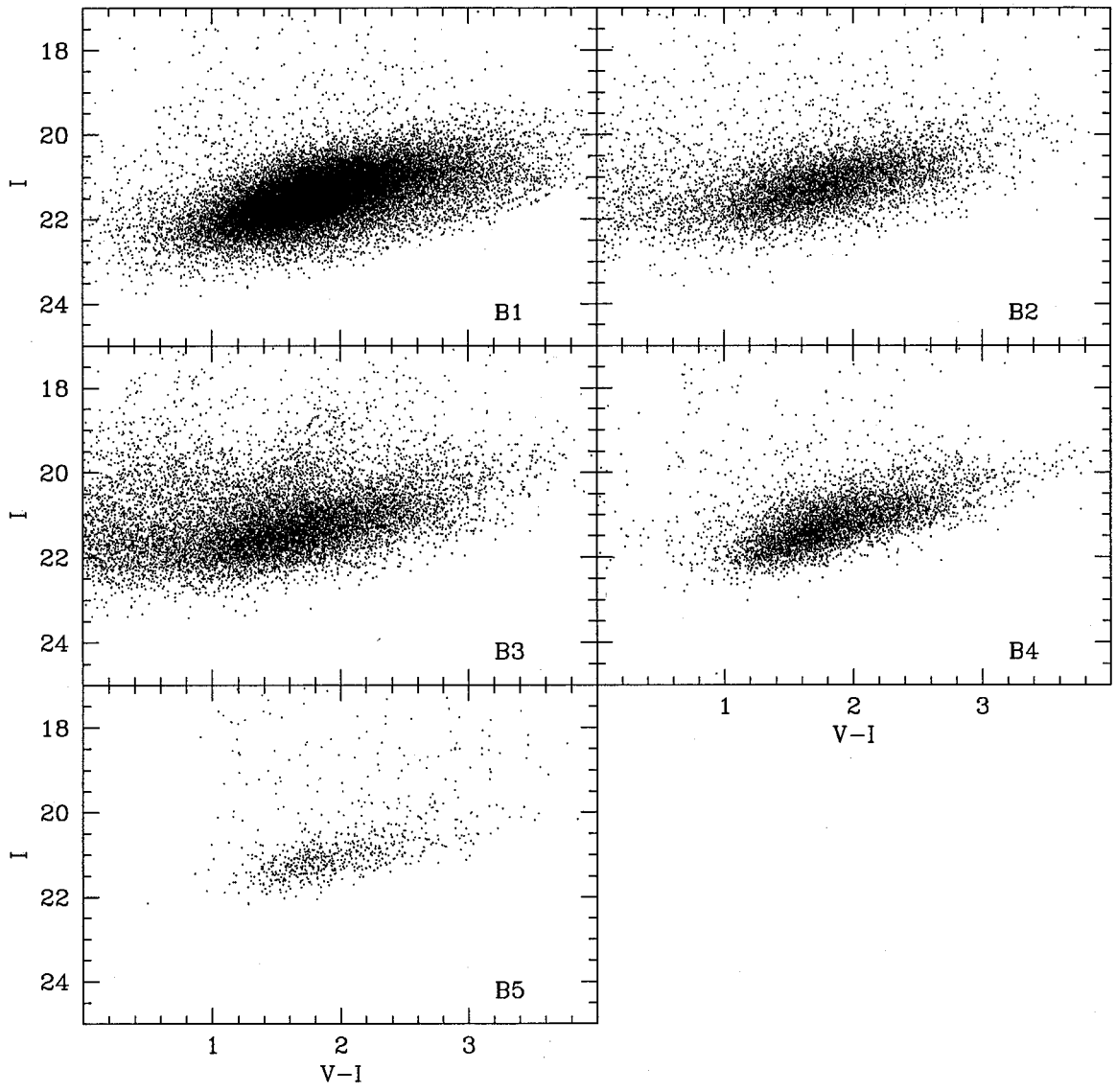

Figure 2.9: Colour magnitude diagrams in $(I, V-I)$ for the B1, B2, B3, B4 and B5 fields. The blue $(V-I < 0.6)$ components can be clearly seen in the B2 and B3 diagrams.

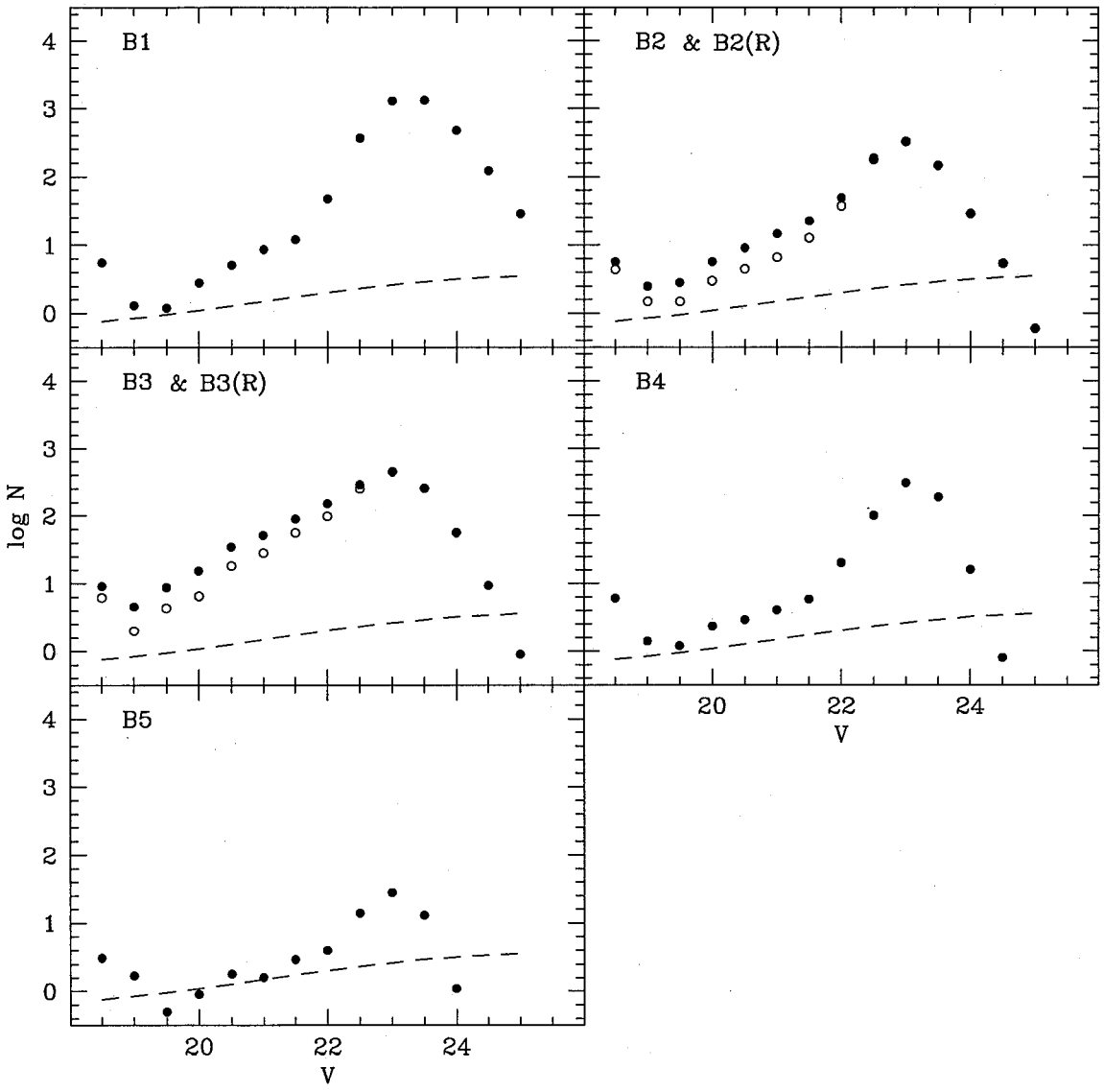

Figure 2.10: V band luminosity functions for the B1, B2, B3, B4 and B5 fields. The open circles in the B2 and B3 panels indicate the counts with the blue ($V-I > 0.6$) component removed. The dashed line show the level of field star contamination predicted by the BSM program. The units are the logarithm of the number of stars per 0.5 magnitudes per 0.0013 square degrees.

Table 2.7: Observed "B" field luminosity functions.

V	B1	B2	B2(R)	B3	B3(R)	B4	B5
19.0	1.30	2.51	1.50	4.51	2.00	1.40	1.70
19.5	1.20	2.81	1.50	8.72	4.31	1.20	0.50
20.0	2.81	5.71	3.01	15.43	6.51	2.31	0.90
20.5	5.11	9.12	4.51	34.48	18.44	2.91	1.80
21.0	8.62	14.73	6.72	51.81	28.26	4.01	1.60
21.5	12.23	22.55	12.93	89.80	55.82	5.91	2.91
22.0	47.81	49.51	37.48	150.03	97.01	20.45	4.01
22.5	369.31	187.81	177.79	286.33	252.15	100.02	13.93
23.0	1299.65	329.22	326.12	451.99	442.17	301.76	28.16
23.5	1315.29	147.22	146.82	256.06	254.76	187.31	13.13
24.0	478.55	29.16	28.96	56.02	55.92	16.14	1.10
24.5	121.57	5.41	5.41	9.32	9.32	0.80	0.10

Chapter 3

The External Galaxy Model

3.1 Introduction

To predict star counts in M31 a mathematical model, similar to that of Bahcall & Soneira 1980, has been developed. In this chapter this external galaxy model and its implementation will be discussed.

Although a version of the Bahcall & Soniera code (written in FORTRAN 77) was available in source form, it was quite basic in operation, and was not very flexible in terms of changing parameters and running extensive sequences and grids of models in "batch" mode. In any event a number of modifications would have been necessary to apply it to an external galaxy.

It was decided to write the External Galaxy Model program (referred to hereafter as EGM) in the ANSI C programming language (Kernighan & Ritchie 1988), rather than in FORTRAN. It was felt that the improved I/O and memory management facilities of C offset the slight advantages in coding formulæ in FORTRAN. The computations required for this modelling are not excessive or complex – however, there is a substantial amount of array management, "book-keeping" tasks and parsing of input parameters, for which C is eminently suitable.

The EGM code was written from scratch using the Bahcall & Soniera Export Code (Bahcall 1986) only as a reference. The final code, approximately 3000 lines of ANSI C, bears little resemblance to the latter except in algorithms, especially in terms of how it

is actually used.

This chapter will first describe the Bahcall & Soneira model used to predict star counts in our own Galaxy, and will then go on to detail how EGM uses the same kind of techniques for an external galaxy. The modifications that must be made and the assumptions implicit in the model will be described. Finally a detailed description of the operation of the core modules of the code will be given.

3.2 The Bahcall–Soneira Model

Bahcall & Soneira 1985 developed a model to predict star counts for a run of magnitudes along a given line of sight in our Galaxy. For a given galactic longitude and latitude, ℓ and b, the model computed the number of stars per unit magnitude per unit area for a range of apparent magnitudes. There are, of course, several important factors that need to be considered. Chief among these are the density distribution of the Galaxy (*i.e.,* number of stars per cubic parsec as a function of $\mathbf{r}$) and the luminosity function (LF, the number of stars as a function of absolute magnitude, M). The Bahcall & Soneira model performs numerical integration on the fundamental equation of stellar statistics (equation 1.1, which is repeated below).

$$A(m_1, m_2, \ell, b)d\Omega = \int_{m_1}^{m_2} dm' \int_0^{\infty} R^2 \rho(\mathbf{R})\Phi(M)d\Omega dR \tag{3.1}$$

where $M = m' - 5\log R + 5 - \Theta(R)$ and the volume element is of size $R^2 dR d\Omega$. Any dependence of ρ on spectral type or luminosity class will be ignored. Except for very simplistic (and unrealistic) forms of Φ and ρ this equation has no analytic solution, requiring the use of numerical integration for its solution. The Bahcall & Soneira model, and its variants, has been used with considerable success by Bahcall & Soneira 1985 and Ratnatunga & Bahcall 1985 as described in Bahcall 1986 and by Pritchet 1983. There are several practical points that may be raised here.

1. The integration does not have to be carried out to $r = \infty$. In practice (and for sensible models for ρ) the integration is stopped at some distance $r_{\max}$ where the contribution to the counts becomes negligible.

2. It is possible to obtain a predicted colour distribution for the model if one has a colour – absolute magnitude diagram. As the integration proceeds (see §3.7) through each magnitude bin in the LF , the colour can be found using a look–up–table of colours and magnitudes. The number of stars with that colour is given by equation 3.1. By convolving the final colour distribution with a Gaussian having a width of the typical observed colour error, an expected colour distribution can be found.

3. Φ does not have to be an analytic function because discrete steps in M are being taken. LFs taken from real data can be used.

4. One can integrate in any order (R then M, or vice versa). However it can be useful to integrate Φ "inside" the integration of ρ so that the distribution along the line of sight can be obtained.

5. Absorption effects are important and must be calculated for each step in R.

6. There are usually a sufficient number of parameters that a change in one can be compensated for by changing one or more *other* parameters, resulting in the same predicted number counts. However it should be noted that this approach is, in essence, *predictive* – it does not try to recover ρ and Φ from an inversion of the data set.

7. There is some evidence for a triaxial bulge – the position angles of the bulge and the disk are offset by some $10°$. The EGM model currently does not model a spheroid

with this shape. Variations of the axial ratio with radial distance are also not modelled.

8. The presence of spiral arms in the disk is not accounted for because there is no convenient functional form to represent them. Neither is any warping of the disk modelled, though it would be possible to include one by modifying the form of the disk density distribution.

9. There is no nuclear bulge component to model fields very close to the centre. However such a component can be easily added to the code if required.

3.3 Geometrical Considerations

As shown in the previous section, the Bahcall & Soneira code integrates the density distribution and luminosity function along a line of sight from the Sun defined by a galactic latitude b and galactic longitude ℓ. This same procedure can be applied to external galaxies if the assumption is made that the observer is in a field in the plane of the (external) galaxy and is looking *back* along the line of sight. By calculating the *effective* b and ℓ for that field almost exactly the same procedure can be used – the chief difference being that the volume element is now a function of the distance along the line of sight *to* the galaxy, rather than the distance from the plane of the galaxy.

The first step is to convert the right ascension and declination of a field to rectangular coordinates, as shown in figure 3.1. The x and y axes are (somewhat arbitrarily) defined to lie along the apparent major and minor axes of the galaxy. The x–axis is inclined to the axis of right ascension by the position angle γ. The transformation of the coordinates of P from (α, δ) to (x, y) is given by equation 3.2.

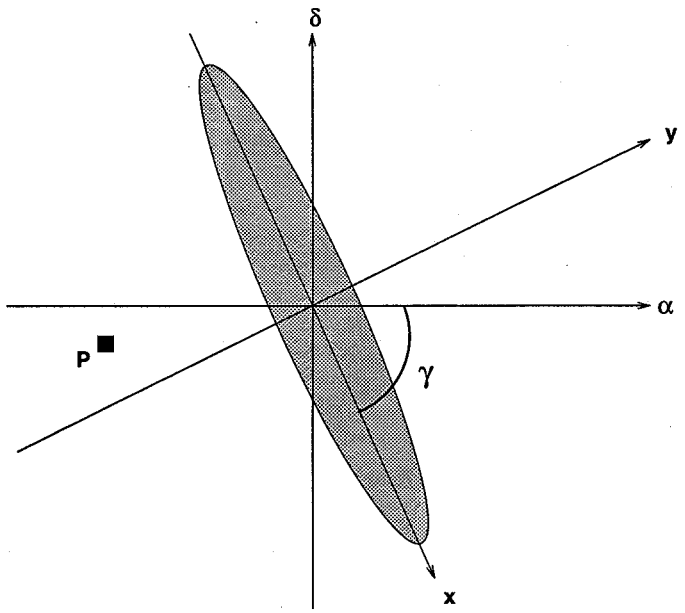

Figure 3.1: Converting the Right Ascension and Declination of the field at P to x and y coordinates. These are defined to lie along the major and minor axes of the galaxy respectively. The shaded ellipse is a schematic representation of an inclined spiral galaxy.

$$\begin{aligned} x &= \alpha\cos\gamma - \delta\sin\gamma \\ y &= \alpha\sin\gamma + \delta\cos\gamma \end{aligned} \tag{3.2}$$

To calculate the effective galactic latitude and longitude of the observer as seen *from* the field (P, in figure 3.1) the procedure is as follows. Figure 3.2 is a side view of the galaxy, looking along the major (x) axis. An observer at O sees a field P in the galaxy whose plane (G) is inclined at an angle i to the plane of the sky (S). The angle b is the "galactic latitude" of O as seen from P. Provided $D >> z$ then $d \approx D$ and $e \approx 0$. Therefore, to a good approximation, $b = 90° - i$.

Figure 3.3 shows a projection of the three dimensional geometry. The x–axis is defined to lie along the line of nodes of the intersection of the galaxy with the plane of the sky.

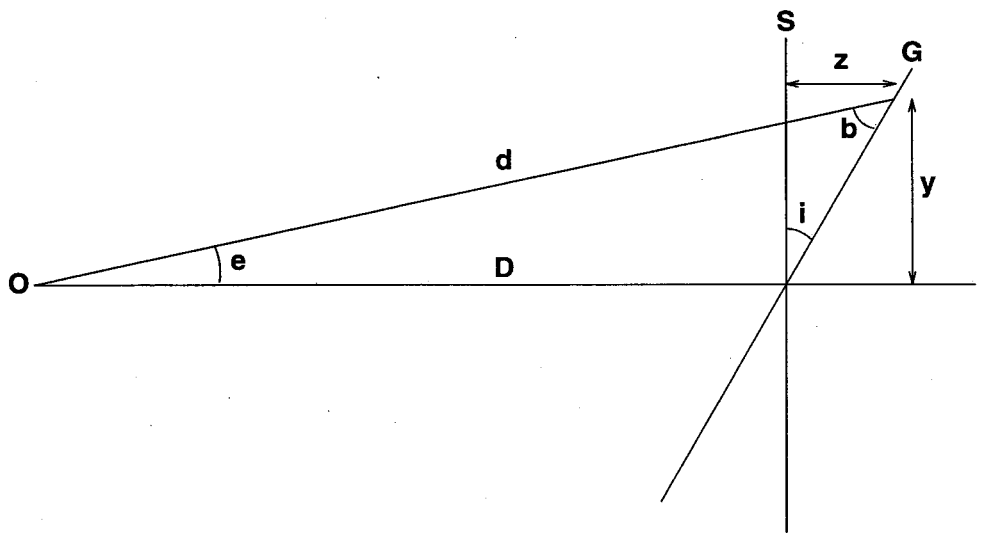

Figure 3.2: A simplified view of the geometry of the situation. The plane of the galaxy (G) is inclined at an angle i to the plane of the sky (S) (as seen from O). Assuming $D >> z$ we have $b = 90° - i$.

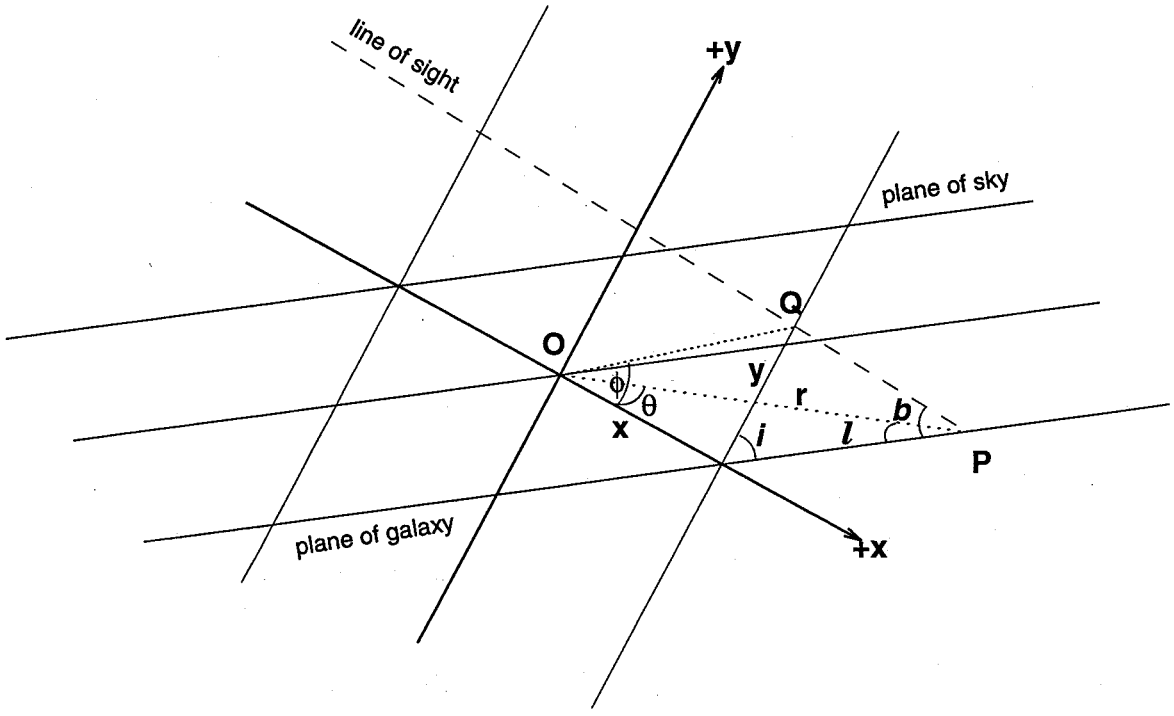

Figure 3.3: As seen by the observer the field Q on the sky projects to P in the galaxy. r and l can be found by geometrical analysis.

The plane of the galaxy is defined by the orientation of the disk component in space. For the spheroid component such a plane has no physical meaning, but does provide a useful reference for the coordinate system – this is the plane about which the spheroid may be flattened by changing the axial ratio. The field Q on the plane of the sky projects to P (in the galaxy). The angle ϕ and the distance of Q from the galactic centre, ρ, are found simply from x and y. r (the distance of P from the galactic centre, in the plane of the galaxy) and ℓ (the effective galactic longitude) are then found from:

$$\begin{aligned} r &= \rho\left(\cos^2\phi + \sec^2 i \sin^2\phi\right)^{\frac{1}{2}} \\ \theta &= \arctan\left(\frac{\tan\phi}{\sec i}\right) \\ \ell &= 90^\circ - \theta \end{aligned} \tag{3.3}$$

Of course this value of ℓ is valid only for this particular quadrant ($x > 0$, $y > 0$ and P being "behind" the plane of the sky, as seen in figure 3.3). Values of r, θ and ℓ for other quadrants and orientations follow easily, and in a similar fashion, once θ has been found.

The EGM program described later in this chapter also calculates the distance PQ in figure 3.3 – the true distance to the plane of the galaxy which is added to the distance derived from the distance modulus (which is taken to be to the centre of the galaxy.) Although small compared to the true distance to M31, the extra calculation is trivial and adds to the completeness of the model.

3.4 Program operation

The major design goals for EGM were to make it easy to use, suitable for batch file processing and to allow for a large number of adjustable parameters. These were accomplished by having EGM being driven only by command line options – no direct interaction by the user is necessary.

The main method of data entry to the program is via "parameter files" – files containing lists of keyword and value pairs. Virtually every parameter in the model is adjustable, though in most cases the program supplied default values are more than adequate. For some of the "key" parameters (inclination, x and y position of the field etc.) these defaults, and the values in the parameter file, can be overridden using command line options. This design makes it easy to change key parameters (e.g. the inclination of the external galaxy) when running several similar models (e.g. with the same input LFs).

The output of the EGM program is a file containing the number counts as a function of apparent magnitude – both differential (number of stars in that magnitude bin) and integral (total counts down to that magnitude). Also given is the colour distribution of the stars for that field. Preceding these data is a header section, listing the values of all the parameters in the model. This feature allows the model parameters to be recovered from a data file.

3.5 Component Description

There are currently only two types of components in EGM – an exponential disk and the spheroidal halo. A third component, the thick disk, is functionally equivalent to the thin disk model and may be optionally included in the model with separate parameters than the thin disk. The functional *forms* discussed below have been hard-coded into the program and cannot be changed without rewriting the appropriate subroutines. The *parameters* in these formulæ can, of course, be set at run-time.

3.5.1 The Disk

The density distribution of the disk stars in the model is represented by the following double exponential function:

$$\rho_d(r) = \rho_d^0 \exp\left[-\frac{z}{h_d} - \frac{x - r_0}{l_d}\right] \tag{3.4}$$

where h_d is the scale height of the disk and l_d is the scale length. r_0 is the distance of the field from the galactic centre (in pc) and z is the height perpendicular to the plane. The h_d, l_d and r_0 parameters can be adjusted in the galaxy model described below. Similar parameters for the thick disk component (h_t and l_t) can also be defined.

3.5.2 The Spheroid

de Vaucouleurs 1959 found that the projected brightness distribution of elliptical galaxies was well represented by:

$$\log \frac{I(r)}{I(r_e)} = -3.3307\left[\left(\frac{r}{r_e}\right)^{\frac{1}{4}} - 1\right] \tag{3.5}$$

where r_e is the spatial distance that projects to an angle containing half the total luminosity. Other functional forms (such as power laws) may be used, however in this work the de-projected form of this will be used. Young 1976 gives an asymptotic approximation for the spatial density of stars which leads to this form of de–projection:

$$\rho_s(r) = \rho_s^0 \frac{e^{-br_j}}{2r_j^3}\left(\frac{\pi}{8br_j}\right)^{\frac{1}{2}} \tag{3.6}$$

where $r_j = (r/r_e)^{\frac{1}{4}}$ and the constant $b = 7.6692$. This formulation is accurate for $r \gtrsim 0.2r_e$. At the distance of M31 this equation can therefore be applied to fields that are more than approximately $1'$ from the centre. Pritchet and van den Bergh 1994, in their study of surface brightness profiles, showed that a de Vaucouleurs profile can fit

the spheroid over a wide range of distances – from 200 pc to more than 20 kpc. Bahcall 1986 presents a similar function with more terms for greater accuracy. The spheroid can also be made oblate by introducing an axial ratio parameter α_s. In this case the new effective radius is $r_e/\sqrt{\alpha_s}$. Note that this is the true, not the projected, axial ratio. Both the effective radius, r_e, and the axial ratio of the spheroid, α_s, can be adjusted in the program.

3.5.3 Absorption

There are three cases where absorption may be included in the model. Absorption from our Galaxy is included as a fixed value to be added in to the apparent magnitude calculations. The model can integrate both sides of the galaxy (*i.e.*, the nearer and the farther sides) – it is possible to include a fixed value of absorption to add to the calculations of the far side integration. This can represent a very thin dust layer throughout the whole disk, or can be applied to a particular field if it is known that there is an excessive amount of absorption in that area.

Three different models for internal galactic absorption are currently supported – no absorption, the "cosecant" law and the Sandage absorption law, the "cosecant" form being the default model. Each case (except for no absorption) requires various additional parameters. The cosecant law calculates absorption based on the formula

$$A(b) = a_1(90°)\csc b \tag{3.7}$$

where $a_1(90°) = 0.15$ magnitudes in V (the default) and $A_V = 0.75A_B$.

The Sandage absorption model (Sandage 1972) in the V band is

$$\begin{aligned} A(b) = &\quad a_2(a_3 - \tan b)\csc b \quad |b| \leq 50° \\ A(b) = &\quad 0 \quad\qquad\qquad |b| > 50° \end{aligned} \tag{3.8}$$

where for the V filter $a_2 = 0.165$ and $a_3 = 1.192$. In the B filter $A_B = 1.33A_V$. This formulation is only defined for the V and B filters.

In both the "cosecant" and Sandage absorption laws, the absorption in magnitudes at distance R from the centre of the galaxy is calculated from

$$A(R) = A(b)\left[1 - e^{(-\sin b/a_0)R}\right] \tag{3.9}$$

where a_0 is the scale height of the absorbing material. The default is 100 pc. It is assumed there is no variation with distance from the galactic centre, only an exponential variation perpendicular to the plane.

WK88 perform a detailed analysis of optical extinction and reddening in M31 using multi-colour surface photometry. A detailed analysis is quite difficult because of the unknown nature of the properties of the dust in the disk, coupled with poor knowledge of the geometrical configuration and sources of illumination. Despite these problems the analysis can be done and results in a reddening law very similar to that of the Milky Way. They derive a reddening law of $A_B/A_V = 1.35 \pm 0.03$, $R_V = 2.8 \pm 0.3$ for a dust lane in the inner region of M31. One may assume that, at least to a first-order approximation, the reddening laws are the same for both the Milky Way and M31.

3.5.4 Density Normalization and Luminosity Functions

One item of program input that needs careful consideration is the density normalization to choose for the disk, thick disk and spheroid components. The initial source of this information is the luminosity function used by the program (and specified by the input parameters) for each component. The LF used for input into EGM is simply a file containing magnitude and number information. Each LF is normalized to some number of stars per cubic parsec in some magnitude range. Also specified is the distance from the galactic centre at which that normalization is valid. For example, Bahcall & Soneira

1980 use a Wielen LF that is normalized to the local density of the disk: 0.13 stars pc^{-3} between $M_V = -6$ and $M_V = 16.5$ at a distance of 8 kpc.

The LF is then scaled (using equation 3.3) to r_0, which is the reference point for the integration (recall that this is the distance, in the plane of the galaxy, from the centre to the projection of the field onto the plane).

Different LFs can be specified for the disk, thick disk and spheroid components. These LFs are stored in files and are read by EGM at runtime. Thus the user can specify any LF desired. It is usually necessary to have these LFs normalized to a value appropriate to the density normalization being used.

3.5.5 Colour–Magnitude Diagrams

EGM uses CMDs to calculate the expected colour distribution for the stars in the field in question. These CMDs are also stored in files and may be specified in a parameter file. EGM uses them to calculate, at each absolute magnitude in the LF, the colour of the stars in the volume element. At the end of the computation the colours are convolved with a Gaussian of some width σ_{ce} (the typical error in colour measurement) to simulate the effect of magnitude errors in measuring colour. Further complications arise if a main-sequence component is included (in the majority of cases it is not, as external galaxies are in general too far away, however the capability is included in EGM). In this case a file giving the fraction of stars on the main-sequence as a function of absolute magnitude must be given. EGM then uses this file to distribute stars in the volume element amongst the giant branch and main sequence components. This only affects the colour distribution.

3.6 Parameter List

There are over 50 parameters in the model that may be set by the user – however this also includes some of the more mundane "management" parameters, such as setting limits on the output apparent magnitude range and so on. Table 3.1 lists some of the more useful and important parameters (*i.e.,* ones that affect the model in a meaningful sense, such as the inclination of the disk, rather than parameters used to define output, such as the faintest magnitude to carry the integration down to), together with a brief description. Note that all distances are in parsecs. In the following text "parameter" is taken to mean one of these parameters that has some impact on the final result.

3.7 Code Description

The operation of the program is fairly straightforward. The basic procedures followed by the code are shown in the flowchart in figure 3.4. Firstly the model parameters are initialized to default values. Then the parameter file and command line are checked for changes to these parameters. The luminosity functions and colour magnitude diagrams are read in, spline fits are made to them and the results stored in arrays, the size of which is determined by the ranges of absolute magnitudes the user desires. The projection parameters (as described earlier in this chapter) are then calculated, as are the scale factors for the density normalization. This is so that the density normalization radius can be kept constant when running several different models with the same LF in the same way that the Bahcall & Soneira model defines the solar circle to be 8 kpc in radius.

The program then proceeds to calculate the differential number counts for the disk and spheroid, and for the thick disk, if appropriate. If the far side of the galaxy is to be included in the model (the default case in the following chapters) then these calculations are repeated, with the required change of projection parameters. The raw data for the

Table 3.1: The basic model parameters.

Parameter	Description
x_0	the position of the field in arc minutes along the major axis
y_0	the position of the field in arc minutes along the minor axis
Ω	field size in square degrees
D	distance to the galaxy
i	inclination of the galaxy in degrees
r_0	distance of projected field to galactic centre
r_p	distance of peak of distribution from galactic plane
dm	apparent magnitude interval
dM	absolute magnitude interval
ρ_d^0	the density normalization of the disk at r_n^d
r_n^d	the normalization radius for the disk LF
l_d	scale length in the plane for the disk component
g_d	scale height of the disk giants
n_d	calculated disk normalization at r_0
ρ_t^0	the density normalization of the thick disk at r_n^t
r_n^t	the normalization radius for the thick disk LF
l_t	scale length in the plane for the thick disk component
g_t	scale height of the thick disk giants
n_t	calculated thick disk normalization at r_0
ρ_s^0	the density normalization of the spheroid at r_n^s
r_n^s	the normalization radius for the spheroid LF
r_e	the de Vaucouleurs effective radius of the spheroid
α_s	the spheroid axial ratio
n_s	calculated spheroid normalization at r_0

colour distribution are collected during the calculations of the differential number counts – the next step for EGM is to collate this information, and to convolve the raw colour distribution with a Gaussian function to represent the "colour error" of the data to be compared. Finally the integral counts are found by accumulating the differential counts, the results are written out and the program ends.

Program use

The first thing EGM does is initialize all the parameters to default values. Then it scans the command line for either parameter files or options. If it finds and can read a parameter file it does so, one line at a time. Each line of this file is parsed for a keyword which is checked against an internal list of valid keywords. If it comes across an invalid keyword it will stop with an error message, otherwise it will overwrite the default value of that parameter with the value in the parameter file. If it detects a valid option on the command line it updates the appropriate parameter directly. A typical invocation of the program may look like this:

```
$ egm m31.pm -x 23.0 -y 45.0 -i 77.0
```

This tells the program to read the keyword – value pairs in the file "m31.pm", set the x_0 and y_0 parameters to 23.′0 and 45.′0 respectively, and to set the inclination of the model to 77°. If the parameter file "m31.pm" sets any of these three parameters itself their values will be overwritten by the subsequent command line options. Full program documentation and the source code can be obtained from the author upon request.

Initialization

EGM obtains values for LFs and CMDs by reading in the appropriate file (specified in the parameter file or on the command line) and using spline interpolation to fill in a

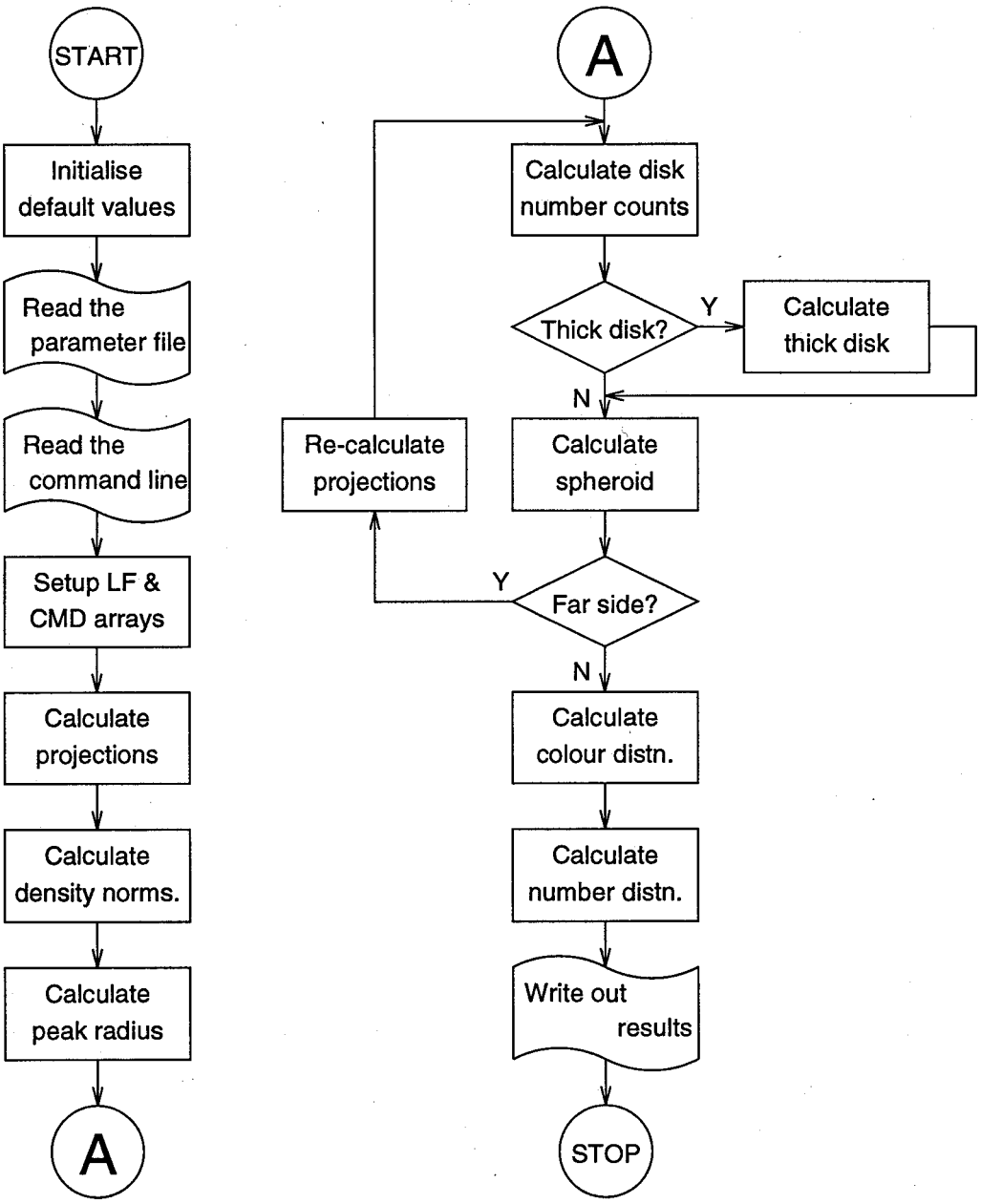

Figure 3.4: A flowchart for the EGM code showing the principle logical steps in constructing a model.

"look up table" (LUT). This is done so that the input LF need not be regularly sampled, or sampled at the same intervals as any other LF . It then uses this LUT to obtain information needed when calculating the star counts. Initialization of the various LUTs occurs after the parameters have been read because the LUT sizes and limits depend on input parameters, such as the brightest and faintest apparent magnitude to calculate the model for. For example, if the brightest and faintest absolute magnitudes for the model to consider are set to -3 and 4 respectively then a LUT of 15 entries is needed if the interval is set to 0.5 magnitudes. The input LF specified in the parameter file is spline fit to this array between these limits.

Several LUTs (which are dynamically allocated at run–time) are needed – one each for the disk and spheroid LFs and the disk giant and spheroid giant color-magnitude diagrams and possibly two more for the main sequence CMD and for the fraction of stars on the main-sequence (FMS) data. These latter two are only needed if the main-sequence component is being modelled. Corresponding arrays will also be needed for the thick disk if it is to be included. Other arrays used to hold the results of the integration (number counts and colour distribution) are also set up at this time but are merely initialized to zero.

EGM now calculates the "projection" parameters – the effective galactic latitude and longitude based on the input parameters (as described in section 3.3) as well as r_0. The density normalization is calculated at this point based on the normalization radius (given on the command line or parameter file). As a convenience it is possible to indicate that the normalization radius is equal to the distance in the plane from the galactic centre to the field. EGM will then calculate and use the appropriate value.

Integration Procedure

The best way to understand how the program works is to examine the source code but since there are approximately 3000 lines of it a shortcut will be taken! In this section considerable reference will be made to figure 3.5, which is a listing of the module for calculating the disk number counts. This is taken directly from the source code, with minor modifications made to the layout and variable names for clarity. In particular, variable declarations have been left out. The bracketed numbers down the left hand side of the code listing denote key points and will be referred to in the following discussion in brackets. Variable names will be typeset in teletype font. Functions are indicated by a set of parentheses containing a number of arguments, such as `obscure(amode, b, r, a)`, or more conveniently, `obscure()`.

The procedure starts ([1]) with the calculation of the area of the field in steradians `farea`. `SQD2ST` is a macro defined to be 0.0003046174 (in square degrees per steradian). `r_max_d` is the maximum distance to carry the integration out to and `dr_d` is the size of the distance step (default is 25 pc) – both may be set by the parameter file. The number of steps to take along the line of sight is derived from these two parameters.

The main integration starts at point [2]. `tot` holds the total number of stars computed, at any point in the integration. (Its main use is at point [17]). The integration proceeds from $r = 0$ to $r =$ `rmax` in steps of `dr_d` ([3]). If r is less than some minimum radius (`r_min`, also specified in the parameter file) then that distance step is skipped. The default value for `r_min` (and the value used in subsequent chapters) is 0 pc, so this never usually occurs.

The statement at line [4] computes the distance of the volume element from the observer along the line of sight, `d`. The value of `DIR` is either $+1$ (integrating from the "plane" away from the observer – the far side of the galaxy) or -1 (towards the observer

```
      void calc_dsk() {
[1]     farea = omega * SQD2ST;

[2]     for (tot = 0.0, j = 0; j < (int) r_max_d / dr_d ; j = j + 1) {
[3]       r = j * dr_d; if (r < r_min) continue;

[4]       d = dist + (DIR * r);
[5]       absmag = obscure(amode, b, r, a) + abs;

[6]       z = r * sin(b);
          x = sqrt(r0 * r0 + r * r * cos(b) * cos(b) - 2 * r * r0 * cos(b) * cos(l));
          vol = d * d * farea * dr_d * dm_abs;
          tmp = vol * exp(-(x - r0)/ psl_d) * exp(-z / gsh_d) * dn[DSK];

[7]       for (znm = 0.0, k = 0; k < nl; k = k + 1) {
[8]         m_abs = m_bri + (k * dm_abs);
            m_app = m_abs + 5.0 * log10(d / 10.0) + absmag;

[9]         if (DIR == FAR) m_app += dabs;
[10]        if ((m_app > ma_dim) || (m_app < ma_brt)) continue;

[11]        if (doms == TRUE) {
              fms = fms[k]; fg  = 1.0 - fms;
            } else {
              fms = 0.0; fg  = 1.0;
            }

[12]        dnms = tmp * lfd[k] * fms; dng = tmp * lfd[k] * fg;
            dnt = dnms + dng; znm = znm + dnt;

[13]        ind = (int) ((m_abs - m_bri) / dm_abs) + 1;
[14]        if (doms == TRUE)
              col_dist(DSK, m_abs, m_app, dnms, ms[ind], dng, dg[ind], pm, nm);
            else
              col_dist(DSK, m_abs, m_app, 0.0, 0.0, dng, dg[ind], pm, nm);

[15]        ind = (int) floor((m_app - (ma_brt - dm_app / 2.0)) / dm_app);
            if (ind >= 0 && ind <= nn) num[DSK][ind] = num[DSK][ind] + dnms + dng;
          }

[16]      tot = tot + znm; if (znm < c_fac * tot) break;
        }
        return;
      }
```

Figure 3.5: The source code listing for the calculation of the disk component. Function prototypes and variable declarations have been removed for clarity.

– the near side). In this way the same routine can be used to determine counts on both the near and far side of the galaxy. `dist` is the distance to the external galaxy in parsecs. The default is 725000.0 (which, by no coincidence, is appropriate for M31).

At this point the amount of absorption affecting the volume element is calculated ([5]) in the `obscure()` function. This uses the galactic latitude, `b`, and `r` to calculate the absorption at that point. `amode` tells it to use no absorption, the cosecant law or the Sandage model, as discussed in §3.6.3. `a` is an array containing the various absorption parameters. Then any fixed value of absorption (`abs`) is added to the value returned by `obscure()`.

At [6] a number of variables whose values remain fixed for that distance step are calculated: `z` is the distance above the "plane"; `x` is the "horizontal" distance in the plane from the galactic centre; `vol` is the size of the volume element; and `tmp` is a temporary variable used to hold the product of the volume element and the scale factors arising from the exponential nature of the disk (the `exp(-x/psl_d)` and `exp(-z/gsh_d)`). Also included is the scaling due to the density normalization, `dn[DSK]`, which is computed as `exp(-(r0 - rn) / psl_d)` where `rn` is the normalization radius. Strictly speaking the `r0` term in both these expressions is redundant, but it is calculated this way so that relative density values may be investigated directly if desired. By including all these factors into one variable the function executes faster.

The program then loops through the disk luminosity function ([7]), which has been initialized in a previous function. The array `lfd[]` contains a look up table of `nl` elements, where `nl` is calculated from the LF limits (`m_bri` and `m_dim`) and the desired absolute magnitude interval `dm_abs`. These are set by the user to cover the desired range over which the LF is used. To ensure that the correct magnitude bins are used this array is a spline fit to the input disk luminosity function. Steps in absolute magnitude are taken, starting at `m_bri` ([8]). At each step the apparent magnitude `m_app` is calculated from

m_abs, **d** and **absmag**. If the integration is taking place on the far side then the value of **dabs** is added ([9]). This is to account for any absorption taking place in the disk of the external galaxy (a very thin dust component, for example, and is in addition to the absorption calculated by **obscure()**).

ma_dim and **ma_brt** define the apparent magnitude desired for output. If the calculated apparent magnitude is outside this range then that step through the LF is skipped ([10]). One point to note is that the integral counts at a particular magnitude are the sum of the differential counts (per magnitude bin) up to that magnitude. Thus if the magnitude range is too restrictive (for example, if **ma_brt** is set too faint) the integral counts will not include all the stars that they should. For models run in this work the limits on apparent magnitude were set at a level to avoid this effect.

[11] For most models of an external galaxy such as M31 one may expect to see only the giant branch, the main sequence turn-off being at $V \approx 27$. However the model does allow the user to include a main-sequence component in the CMD if desired. At a given absolute magnitude bin (**k**), the proportion of stars on the main sequence is given by **fms[k]** (a number between 0 and 1), where **fms[]** is an array used as a LUT and filled at program initialization using spline fitting to a user defined table specified as a parameter. The fraction of stars on the main-sequence and giant branch, **fms** and **fg**, are then used in step [12].

dnms and **dng** are the counts contributed by the main-sequence and giant branches for the volume element at that absolute magnitude (**k**). **dnt** is the sum of these two variables and **znm** is the total for that volume element.

The next step ([13]) is to fill in arrays holding the colour distribution in the model. This is done in the **col_dist()** function ([14]). **ind** is an index into the main-sequence and giant branch CMD arrays (**ms[]** or **dg[]**) which hold the colours for a particular absolute magnitude bin.

The final step in the LF loop is to store the number counts ([15]). `num[] []` is a two dimensional array containing the differential counts (*i.e.,* counts per magnitude bin, `k`) for the disk, thick disk and spheroid components. The macro `DSK` is defined to point to the correct column for storage of the disk counts. `ind` is now set to be an index into the `num[] []` array. The somewhat baroque looking formula for `ind` ensures proper alignment of bin boundaries.

Before proceeding to the next volume element a check is made ([16]). `tot` is the total number of counts so far for the integration of this component. If the counts from the current volume element, `znm`, are less than some fraction of the total (`tot`), the procedure finishes. The fraction `c_fac` has a default value of 1×10^{-6}, which is sufficient for most purposes.

Post-Integration

The integration procedure for the thick disk and spheroid is very similar, differing only in the choice of parameters (in the former case) and density distribution (in the latter).

The far side of the external galaxy is integrated separately after the near side – this is also the default mode of operation. The calculations for the far side of the galaxy proceed in an identical manner, except for the possible inclusion of extra absorption and the fact that now as distances from the galaxy increases, so do the distances from the observer.

In the final steps the computed colour distribution is convolved with a Gaussian error distribution to obtain the predicted colour distribution. Various other statistics of the colour distribution (mean colours of each component and of the total distribution, etc.,) are also worked out. The cumulative number counts in each magnitude bin for each component is calculated from the differential counts. The results are then written out on the standard output stream or to a file.

3.8 Source Code Availability

A copy of the source code and full documentation may be obtained from the author, or via anonymous FTP from `ftp.astro.ubc.ca:/pub/hodder/`. ZIPped and compressed TAR files are available for the External Galaxy Model (`EgmSrc17.zip`, `EgmSrc17.tar.Z`), a version of the Bahcall & Soneira Model developed during the first stage of EGM (`BsmSrc32.zip`, `BsmSrc32.tar.Z`), and a set of utility programs useful in creating and normalizing LFs and CMDs (`GmuSrc12.zip`, `GmuSrc12.tar.Z`).

Chapter 4

Modelling the Spheroid

4.1 Introduction

This chapter will detail the results of using the EGM model to obtain various parameters of the M31 spheroid. The sensitivity of the model to these parameters (mainly the axial ratio of the spheroid and its effective radius) will also be discussed. The observed V band luminosity functions (hereafter abbreviated to "LFs") of the fields G302, G312, G352 and B5 will be used and the limitations of this data set will be explored. It was thought that the B5 field might be a pure spheroid field – this turns out not to be the case, but part of the B5 analysis will be discussed here as well as in Chapter 5.

The intent is to determine spheroid parameters first using fields uncontaminated by the disk. These model parameters can then be used to "subtract" spheroid counts from the disk field observations. Deconvolution of the disk and thick disk counts (if modelled) would be more problematical because the two systems are physically coincident.

4.2 The Input Luminosity Function

One of the most important input parameters to the EGM model is the luminosity function (LF) – *i.e.,* the number of stars per unit volume (cubic parsecs for example) per magnitude bin. However, all that is known initially is the *observed* LF of the field (*i.e.,* the number of stars per unit area (square parsecs) per magnitude bin). To get the actual density of stars one must either deconvolve the observed LF and density distribution,

or select an assumed LF and density normalization, compare the resulting model prediction to the observations and iterate to a solution. This density normalization must be specified at some normalization *radius* – the distance from the galactic centre where that density applies. However, because the form of the density distribution follows (or is assumed to follow) the $r^{\frac{1}{4}}$ law they are in fact coupled and can be taken as a single parameter.

Figure 4.1(a) shows the spheroid contribution from points along the line of sight for a typical (the default) model. As might be expected most of the counts originate from a comparatively small region where the spheroid peaks in density but because the distribution still has some finite width it is not possible to easily convert from the observed LF to a density. If the LF has simple linear form (such as a power law) then adding the contributions from different densities along the line of sight will not distort the shape of the final LF. However if the LF is not a simple function, or is a combination of linear pieces of different slopes, then the final LF will *not* be the same shape as the input LF. In practice, because the main contributions to the final observed LF all come from a narrow region around the peak, any such distortion is minimal. In addition, if the normalization is restricted to a narrow *magnitude* range then this effect is greatly reduced. This is shown in figure 4.1(b), which compares the DaCosta 47 Tuc LF (discussed below) to the predicted number counts resulting from running it through the EGM model. As can be seen there is a small amount of overall distortion introduced by the integration process, and the effect at brighter magnitudes (of interest in this work) is even smaller.

The problem is then deciding upon the density normalization of the LF. One possibility is to assume the observed LF has the correct *shape* of the actual LF (with the caveats mentioned above) and choose some arbitrary normalization for it. When run through the model this will produce a set of predicted counts that can be scaled to the original normalization. This scaling factor can give the density normalization that will

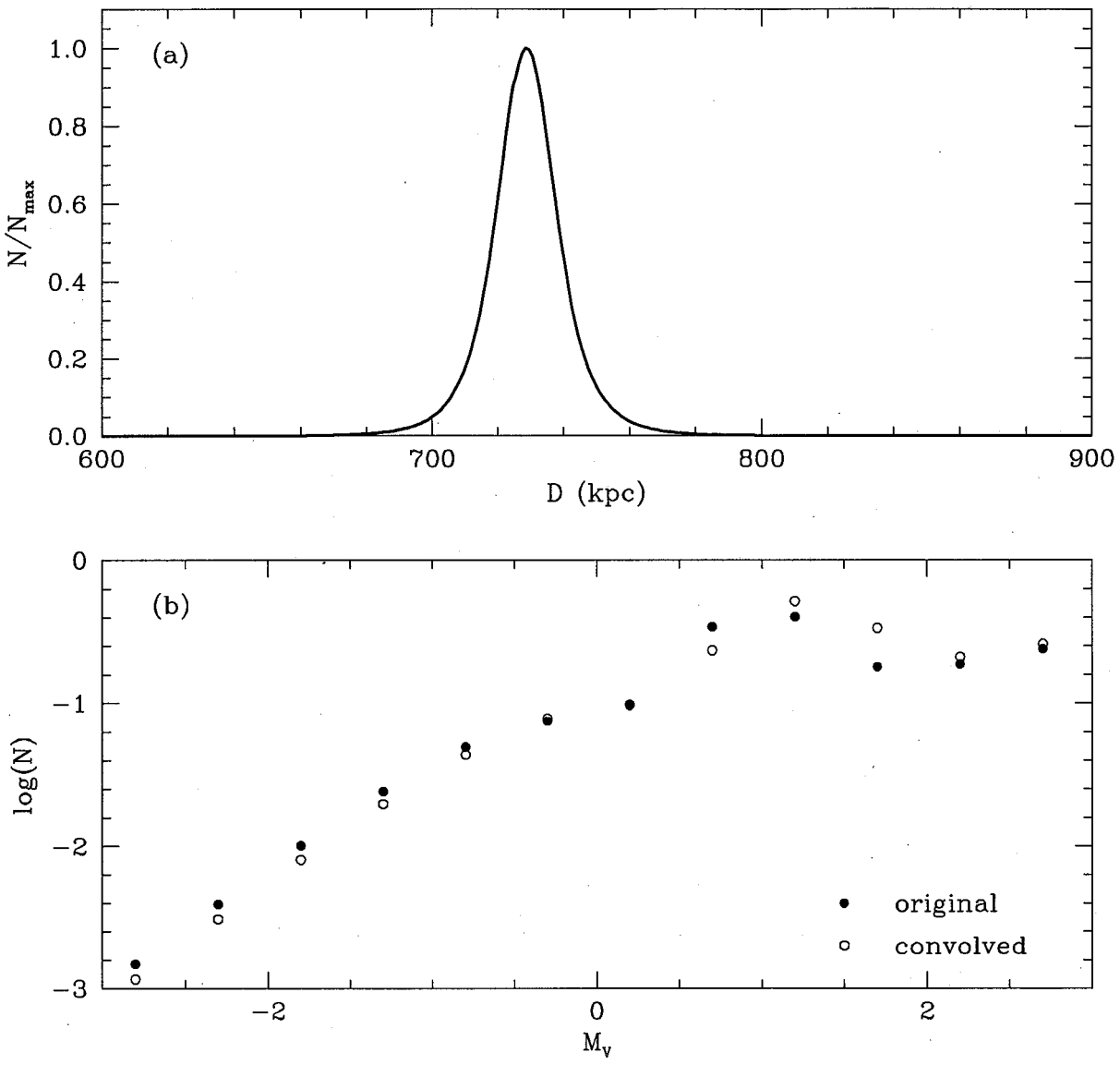

Figure 4.1: (a) The spheroid counts for a model 50′ along the minor axis is plotted against distance from the observer. The counts have been normalized to the maximum value. (b) The input DaCosta 47 Tuc LF (filled circles) plotted with the final number counts (open circles) resulting from "convolving" the input LF with the density distribution in figure 4.1(a).

return the correct number counts, and can be used to investigate the effect on the number counts of a particular field for various model parameters. This works because the number counts reported by EGM scale directly with the density normalization of the input LF. That is, if the number of observed counts in a particular magnitude range is N_o and the observed LF is scaled to n stars pc^{-3} , then if the model results in a predicted count of N_p the actual density normalization is nN_o/N_p. One interesting result of this is that foreground absorption "drops out" of the calculation in the sense that if the observed LF is de-reddened by, say 0.1 magnitude, this must be added into the model in order that the same LF is recovered. This is not to say that it is not important in converting apparent to absolute magnitudes.

Alternatively, a known LF can be used – provided that the properties of the object from which it was derived are similar to those assumed for the spheroid in the model. The difficulty then is finding a LF corresponding to that metallicity from, say, a suitable globular cluster. Pritchet and van den Bergh 1988 derive a metallicity of the halo of M31 of [Fe/H] ≈ -1. A reasonable approximation to this is to use the 47 Tuc LF presented by DaCosta 1982. 47 Tuc has an [Fe/H] of -0.71 (Lang 1991) and its LF has been successfully used in the original Bahcall & Soneira model, although that was for the Milky Way. Figure 4.2 plots the DaCosta 47 Tuc LF together with the observed number counts of the G302, G312 and G352 fields. Also shown is the mean observed LF for the three "G" fields. This was derived by normalizing each LF to some arbitrary value and taking the mean. The resulting LF represents the mean *shape* of the LFs, not the number counts. In the figure some of the "mean G" points lie outside all three G field LFs – this is because of the arbitrary normalization used to compare the shapes. The observed LFs are somewhat steeper than the 47 Tuc LF at brighter magnitudes – this implies that even the best fitting model may not fit very well. Figure 4.1(b) shows that there is little distortion introduced by assuming the observed LF has the same shape

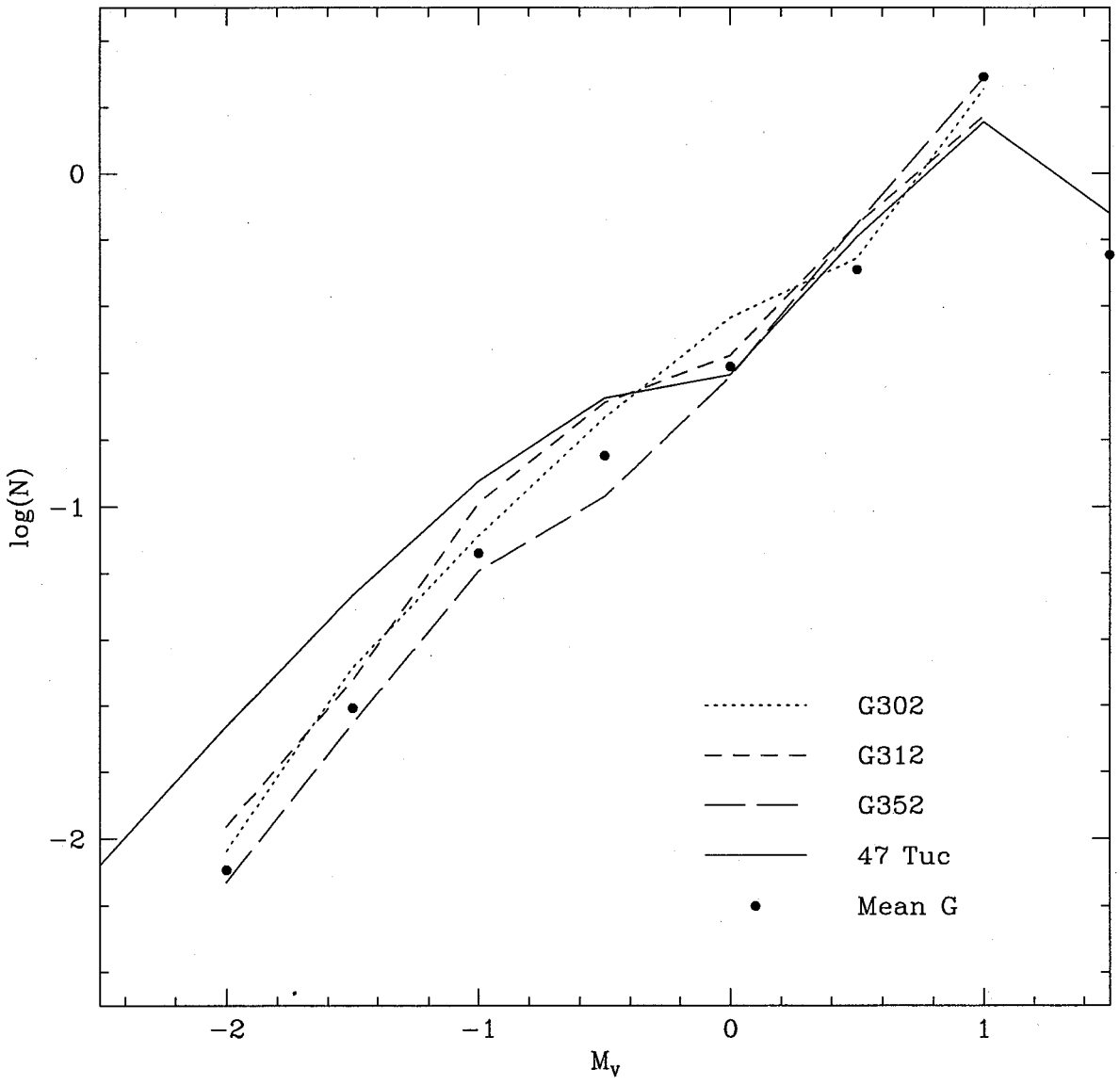

Figure 4.2: The observed LFs for the G302, G312 and G352 fields are shown together with the 47 Tuc LF from DaCosta 1982. The observed LFs have been shifted by the M31 distance modulus and reddening and all the LFs have been arbitrarily normalized to the same value between $-2 \leq M_V \leq +1$ so the shapes can be compared.

as the underlying luminosity function: it is therefore possible to use the "mean G" LF as one of the input parameters. It should be noted that this method is guaranteed to achieve a better fit between the model and observations than using the 47 Tuc LF, and this should be borne in mind during the following discussions. Note also that the "mean G" LF has been extended to faint magnitudes by using a standard Wielen 1974 LF for magnitudes $M_V > 1$. This has been done for completeness and does not affect the results significantly – the contributions of these faint stars (below the main-sequence turn off) is negligible given the type of observations available. For the majority of the analysis performed in this chapter the "mean G" luminosity function will be used.

All density normalizations have been performed at a distance of 10 kpc and between the magnitudes $-1 \leq M_V \leq +1$. These choices are arbitrary but normalizing at different radii and magnitude ranges merely serves to scale the input LF – the actual values are not important as long as they are consistent.

4.3 A Default Model

To facilitate the discussion of the response of the model to different parameters it is useful to define an initial model using a default set of parameters. Some of these parameters are collected from a variety of previous works which use studies of the galaxy's integrated light rather than star counts. This default model can be used as a starting point for each field.

The two most important spheroid parameters are the axial ratio (α_s) and the effective radius (r_e). Pritchet & van den Bergh 1994 use measurements of integrated light of star counts to derive values of these parameters. (see Chapter 1 for a more complete description). They derive $\alpha_s = 0.55 \pm 0.05$ and an effective radius of the minor axis of $b_e = 1.3$ kpc. It is interesting to compare these values to the results by WK88 derived

using surface photometry: $\alpha_s = 0.63$ and $r_e = 2$ kpc. It should be noted that in the model the parameter α_s refers to the *true* axial ratio, not the *projected* axial ratio as measured by surface brightness studies. At the low inclination of M31, however, there will be little difference between the two.

A third parameter important in the model is the inclination, i, of the galaxy. Although this strictly speaking refers to the inclination of the disk relative to the plane of the sky any non-spherical halo is assumed to be oblate – that is, flattened about the plane of the disk. The inclination of the model is set to 77°.5 (van den Bergh 1991). The other parameters for the default model were chosen to be $\alpha_s = 0.6$ and $r_e = 2$ kpc.

van den Bergh 1991 reviews foreground reddening estimates of M31. He adopts a value of $E_{B-V} = 0.08$, consistent with Burstein & Heiles 1984 ($E_{B-V} = 0.08$), Walterbos & Schwering 1987 ($0.06 \leq E_{B-V} \leq 0.09$) and Massey, Armandroff & Conti 1986 (from the minimum reddening for OB associations, $E_{B-V} = 0.08$). A value of $E_{B-V} = 0.08$, leading to an absorption in V of 0.248 magnitudes will be assumed in the following work. It is also assumed that there is no reddening in the M31 halo itself.

As a final point the final field size is set to 0.0013 square degrees (or 4.68 square arc minutes). This is slightly smaller than the CCD area discussed in Chapter 2 because it accounts for the masking out of regions of the image containing the guide star, globular cluster and bright galaxies from the incompleteness tests.

4.4 A Problem with the G352 field

The data from the G352 field presented something of a problem at the very outset: even using an approximate $r^{1/4}$ law calculation there are too many stars by a factor approximately 2 to 3!

One possible reason for this was an error in the data reduction procedure. The

final image used in the analysis for the G352 field was an average of 3 separate frames. As a check each of the three V frames was re-reduced, calibrated and incompleteness corrected separately. All three frames gave the same results as each other and with the combined frame (to within the calculated errors), reducing the possibility of an error in the reduction process.

During this procedure it was noted that there were a large number of fairly bright and obvious galaxies on the frame, indicating possible contamination by a background cluster (in excess of the normal background field galaxies). An attempt was therefore made to remove these galaxies from the observed LF using image shape statistics. This works well for the brighter objects but becomes increasingly difficult at fainter magnitudes. The numbers of galaxies indicated by this method could not account for the excess.

A search for galaxies and cluster of galaxies in the region of G352 was made using the NASA Extragalactic Database. [1] There are several individual galaxies and galaxy clusters in the region but none is near enough to account for the excess objects.

Another possibility is that the area is being contaminated by some other unknown object external to M31 (e.g. a dwarf galaxy captured by M31, a stellar stream or other exotica). However a contour plot (not shown) of the number of stars per unit area showed no indication of any other "physical" component – but given the small size of the field this is hardly surprising. The CMD also does not reveal any additional components.

4.5 Comparing the Model and Observations

When comparing a particular model to a set of observed number counts it is necessary to define some sort of "goodness-of-fit" criterion. A simple χ^2 test is quite suitable.

[1]The NASA/IPAC EXTRAGALACTIC DATABASE (NED) is operated by the Jet Propulsion Laboratory, California Institute Of Technology, under contract with the National Aeronautics and Space Administration

The model predictions m can be compared to the observed number, n, noting that in each magnitude bin there are some foreground and background contaminants, c, to be subtracted. The χ^2 statistic used in the remainder of this analysis is:

$$\chi^2 = \sum \frac{(m_i - (n_i - c_i))^2}{\sigma_{n_i}^2 + c_i} \tag{4.1}$$

where the sum is taken over i (all the magnitude bins where $n_i > 0$). Here σ_{n_i} has been taken from Table 2.6 and is the quadratic sum of the Poisson counting errors for each incompleteness test, the standard deviation in the mean of each bin for each test and the error in the incompleteness fraction. It is then possible to find the probability, $Q(\chi^2|\nu)$, that the observed chi-squared exceed the value χ^2 even if the model is correct. Note that this definition of χ^2 assumes that all the errors are Gaussian. This is not quite the case here, which has the effect of increasing the minimum χ^2, but does not change its position is parameter space.

Using this χ^2 statistic has the effect of giving the bins at the faint end of the LF only a small influence over the quality of the fit but fortunately this is also the region in which the background galaxy contamination becomes large and possibly uncertain. The final estimate of how well the model matches the observed counts is therefore only weakly influenced by these corrections.

4.6 Model Sensitivity

This chapter is principally involved with trying to determine the effective radius, axial ratio and density of the spheroid. The EGM model was tested to see if it was possible to determine these parameters to sufficient accuracy. For example, one could take an assumed spheroid density and vary r_e or α_s and see what effect this has on the resultant number counts. If the variation is much less than the errors in the observed LFs it may be difficult to obtain a unique result.

These sensitivity tests will be presented for sets of test fields along the major and minor axes. All the fields discussed here are close to one of these axes and it is useful to see the general trends of the model. In all these tests the "mean G" luminosity function was used with a normalization of 3.1×10^{-6} between the magnitude range $-1 \leq M_V \leq +1$. This normalization value provides the best fit to the G302 and G312 data in the $V = 22.5$ to $V = 24.5$ range using the standard model. See §4.7 below for a detailed discussion of the density normalization estimates.

4.6.1 Tests with Spheroid Axial Ratio

In this test the sensitivity of the minor axis counts to the spheroid axial ratio were investigated. The default model was run for 20 minor axis fields at distances of 10′, 20′, ... , 190′, 200′ on the same side of M31 as the observed minor axis fields (which have a positive value of y_0 as defined by the coordinate system given in Chapter 3). The G312 field (at x_0 = -4.′473, y_0 = 49.′648) is sufficiently close to the minor axis that comparison can be made directly.

In the first test the axial ratio was varied from 0.1 to 1.0 in steps of 0.1. The $\alpha_s = 0$ case is not physical and was not considered. Figure 4.3(a) shows a large variation in the counts in the 0.5 magnitude wide bin centered at $V = 22.5$ with α_s, over the whole range of the minor axis. [2] Also shown are the counts in that bin for the G302, G312 and G355 fields (corrected for foreground and background contamination) – there are 33.36 ± 6.73, 19.36 ± 4.14 and 5.72 ± 3.71 stars respectively. The G302 and G312 counts both fit the model quite well, though not exactly because these fields are not aligned precisely along the minor axis. The G355 field shows a poor fit – this may be attributed to the poorer quality of the data (see Table 2.1) and the fact that the counts at this distance from

[2] All figures of this nature have been plotted with the same axis scales for each of the major and minor axes, to facilitate comparison.

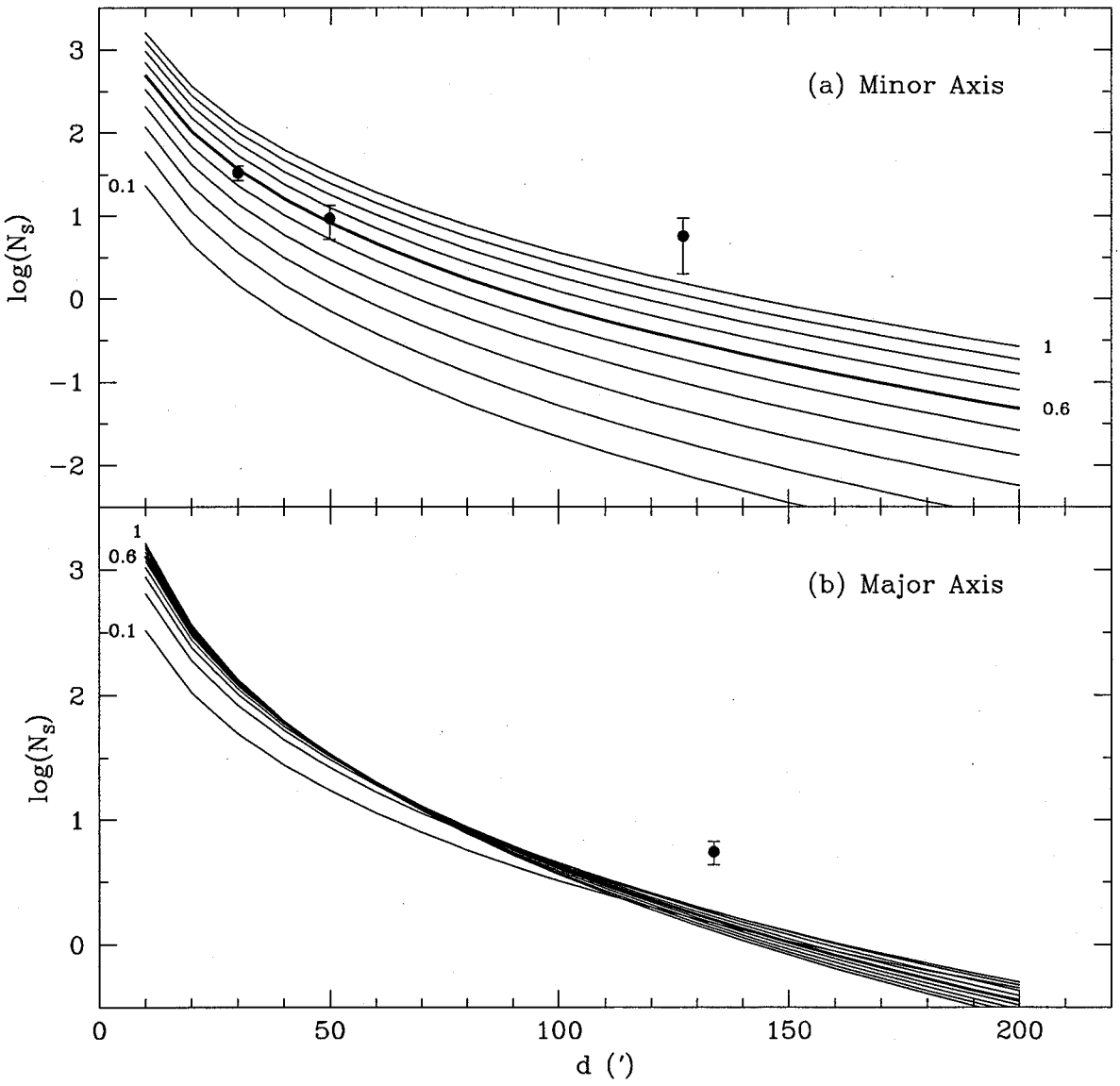

Figure 4.3: This figure shows the variation of spheroid counts with axial ratio, α_s, for the minor axis (panel (a)) and the major axis (b). The remaining parameters used the default values. The heavy line shows the default models. (a) There is a large variation in number counts with α_s. The points represent the number counts in the $V = 22.5$ bin from the G302, G312 and G352 fields. (b) There is much less of a variation along the major axis, even over the whole range of α_s. The counts from the B5 field are also shown here.

the centre of M31 ($\approx 127'$) are very close to the contaminant levels. At the $50'$ field the counts are 0.3 for $\alpha_s = 0.1$ rising to 33.1 for $\alpha_s = 1.0$ – a factor of approximately 110. Of course it seems unlikely that the spheroid of M31 has an axial ratio as flat as 0.1 but even taking $\alpha_s = 0.4$ (where the number count equals 3.0) as a reasonable lower bound there is still a possible variation by a factor of 10. The error in the counts is such that any change in axial ratio by more than 0.1 could be detected (although this may be masked by changed in r_e and the normalization). Furthermore, the variation of the number counts is approximately equal over the whole minor axis range, implying that this parameter may be tested at fields closer to the centre, where the number counts are higher and are less susceptible to foreground and background contamination.

Figure 4.3(b) shows the variation of major axis number counts with spheroid axial ratio. The models were run at the same galacto-centric distances as above but along the major axis. There does not appear to be a great deal of change from one model to the next. This is because the flattening of the spheroid with decreasing α_s is not "foreshortened" along the major axis as it is along the minor axis (and as a disk would be). The counts (corrected for foreground stars *and* background galaxies) for the B5 field are also shown on this diagram – the agreement is poor because of the significant disk contribution at this position in the galaxy. At $x_0 = 130'$, which corresponds closely to the B5 field (see Chapter 2) the spheroid counts change from 2.0 (at $\alpha_s = 0.3$) to 1.4 at $\alpha_s = 1$. Note the slightly peculiar behaviour of the $\alpha_s = 0.1$ and $\alpha_s = 0.2$ models which intersect the rest of the curves.

4.6.2 Tests with Effective Radius

The effect of the effective radius, r_e, on the minor axis counts was tested next. Values ranged from 1 kpc to 4 kpc in steps of 250 pc – otherwise the same set of fields and default parameters were used. The results are presented in figure 4.4(a). The crossing

point of all the models is at $y_0 \approx 24'.3$, which corresponds to a distance of 4639.1 pc on the sky and 21433.7 pc in the plane of the galaxy. On close examination it was seen that the curves did not all intersect at the same point – in this region they are just closest together.

The larger the effective radius of the spheroid (which, recall, is the half light radius), the higher the counts at a particular field. Changing r_e has much less of an effect at small distances but quite a large one further out in the halo. At $y_0 = 50'$ the counts only change from 11.6 (for $r_e = 4$ kpc) to 5.7 (for $r_e = 1$ kpc). However at distances of more than approximately $150'$ the number counts become small enough that they can be affected greatly by foreground contamination regardless of r_e. (Note that increasing the field size to try and compensate for this will also scale both the number counts and the contaminants.)

The G302, G312 and G355 data for the $V = 22.5$ bin are also shown on figure 4.4(a). It can be seen that, for the default model, the ability to detect a deviation in r_e is poor. This implies that it will be difficult to derive an exact value for the effective radius of the spheroid.

Similar tests were performed for the major axis – although there is no available data for halo fields along the major axis it may be useful to know how the halo behaves in that region. These results may also be used in the analysis of the disk fields where subtraction of the spheroid counts may be important. Models were generated for fields at 10, 20, ..., 190 and $200'$ along the major axis. Note that the EGM model is symmetrical about the minor axis (*i.e.*, models run at x_0 and $-x_0$ will be identical.)

The changes in counts due to changes in effective radius (figure 4.4(b)) can, on the other hand, be more substantial along the major axis than the effects of axial ratio. At $x_0 = 130'$ the observed spheroid counts change from 0.9 when $r_e = 1$ kpc to 3.1 when $r_e = 4$ kpc – a factor of 3.4. However the effect of changing r_e when the effective radius is

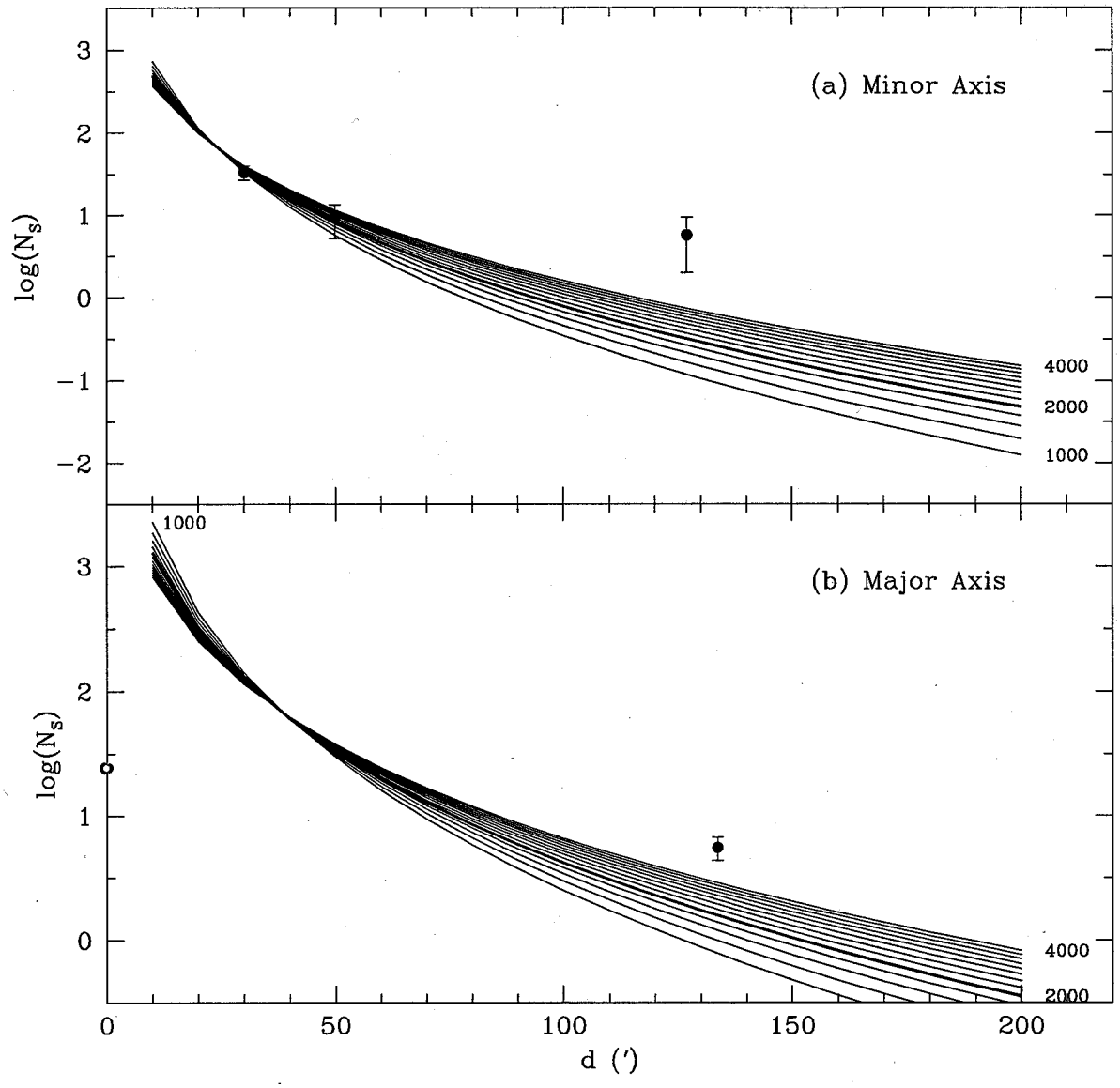

Figure 4.4: This figure shows the variation of the spheroid counts with effective radius, r_e, for the minor axis (panel (a)) and the major axis (b). The remaining parameters used the default values. The heavy line shows the default models. The variation is approximately equal for both axes, and is not as large as the variations caused by axial ratio (figure 4.3). In (a) the counts in the $V = 22.5$ bin for the G302, G312 and G355 fields are shown; in (b) the B5 counts are plotted.

already large is minimal. Again note the apparent crossing point of the models at $x_0 \approx 38'.4$ corresponding to a distance of 7330.9 pc.

4.7 Initial Density Estimates

There are three parameters that have to be determined for the spheroid model: the axial ratio of the spheroid (α_s), its effective radius (r_e) and the density normalization ρ_0^s at some radius r_n^s. Accordingly data from at least three different fields is needed. Unfortunately, as noted above, the G352 field shows a large excess in the number counts, and the B5 has a significant contribution from the disk. However an attempt will be made to at least set out the problem and describe a method for solving for a unique parameter set.

In order to make some initial estimates of the density normalization, one can conduct the following experiment using the scaling method discussed above: normalize the input LF to some arbitrary value (1.0, say) between some magnitude range and use it in the EGM model. The ratio of observed to predicted counts gives the scaling factor for the normalization. This scaling factor value can be used to compute the normalization that would predict the same number of stars as is actually observed, for that field and set of parameters α_s and r_e.

Using this procedure for the four spheroid fields at 10 kpc and normalizing to counts using the bins from $V = 22.5$ to $V = 24.5$ (except for B5 which was to be normalized over the range 22.5 to 23.0 to avoid using data from faint magnitudes) the following densities ($-1 \leq M_V \leq +1$) are obtained:

G302: 3.11×10^{-6} stars pc^{-3} G352: 5.00×10^{-6} stars pc^{-3}

G312: 3.07×10^{-6} stars pc^{-3} B5: 1.81×10^{-5} stars pc^{-3}

Note that the densities for the G302 and G312 fields are very similar, the value for the

G352 field is too high by a factor of approximately 1.6, and that density returned by the B5 data is a factor of approximately 6 too large because disk stars are being included in the calculation. A spheroid density normalization of 3.1×10^{-6} will be used as a default in the tests that follow.

This procedure was also carried out for the four fields G302, G312, G352 and B5 over a grid of α_s (varying from 0.1 to 1.0 in steps of 0.1) and r_e (varying from 1 kpc to 4 kpc in steps of 250 pc). The results are shown in figure 4.5. It was assumed that the B5 field is a pure spheroid field – this is not the case (see Chapter 5) but it is still instructive to run the test. In these tests the "mean G" LF was used and was normalized to a value of 1.0 between $-1 \leq M_V \leq +1$. For each "G" field the number counts between the $V = 22.5$ and $V = 24.5$ bins were used to derive the required density normalization (at 10 kpc). For B5 the counts in the $V = 22.5$ and $V = 23.0$ bins were used. These values are plotted as contours in figure 4.5. The contour values range from 1×10^{-6} stars pc^{-3} to 1×10^{-4}. Heavy lines indicate contour values of 10^{-6}, 10^{-5} and 10^{-4} and are labelled.

Figure 4.5 can also be viewed as a plot of density surfaces – at each value of α_s and r_e on the grid the height of the surface gives the density normalization. The set of parameters (α_s, r_e, r_n^s) that results in the correct densities for all the fields concerned can be found where two of these surfaces intersect. This line of intersection when projected onto the (α_s, r_e) plane will determine the set of values that gives the same density normalization for each field. Therefore at least three fields are needed: two pairs of fields will give two lines which will themselves intersect at the solution (indicating that this pair of (α_s, r_e) values satisfies all three models). However this is not a very rigorous procedure and provides no information on how well this solution fits the data. In figure 4.5 the slopes of these "surfaces" are nearly the same for the G302, G312 and G352 fields which further compounds the problem.

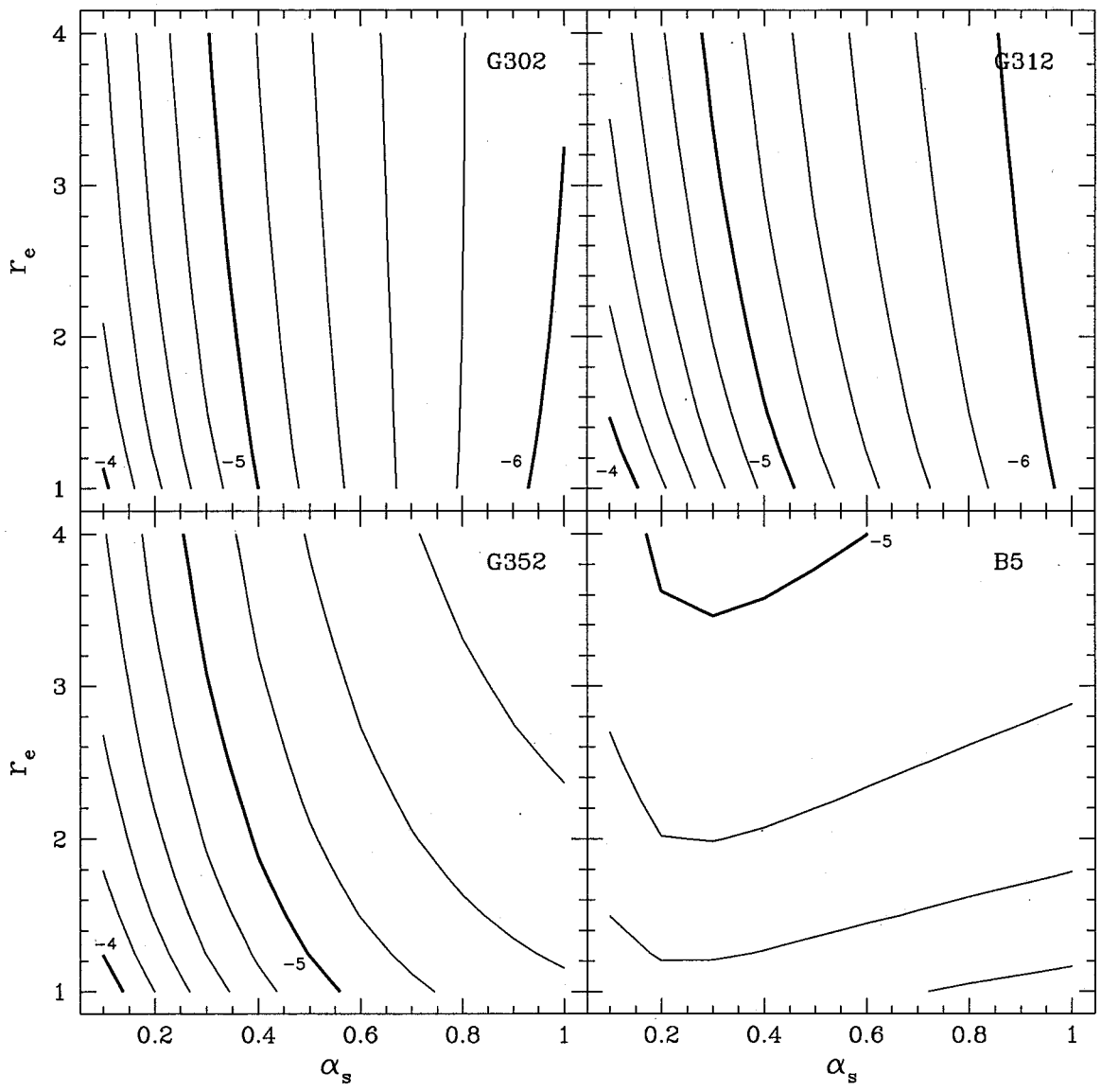

Figure 4.5: A contour plot of the $\log_{10}$ of the density normalizations that have to be applied to the data for fields G302, G312, G352 and B5. The contours range from 1×10^{-6} to 1×10^{-4} in steps of 0.2 in the log – the contours at 10^{-6}, 10^{-5} and 10^{-4} are plotted in heavy lines and are labelled.

4.8 Parameter Grids

An alternative to the above approach is to run the EGM model over a grid of density normalizations as well as a grid of α_s and r_e. The "mean G" LFs was normalized to a sequence of values running from 2.1×10^{-6} to 6.1×10^{-6} in steps of 5×10^{-7} stars pc^{-3}, over the magnitude bins centered at $-1 \leq M_V \leq +1$. A grid over α_s and r_e (as described above) was run for each of these values. For each model the χ^2 statistic described in §4.5 was calculated over the range $22.5 \leq V \leq 24.5$ and from this, the probability Q. In essence a three dimensional "data-cube" is built up over parameter pace.

Figure 4.6 shows the observed G312 LF and four different models, one of which – using default parameters and a spheroid normalization of 3.1×10^{-6} stars pc^{-3} – fits quite well indeed. The χ^2 value is shown for fitting the model and observations using the magnitude bins from $V = 22.5$ to $V = 24.5$. Note that a χ^2 of less than 5 (the number of degrees of freedom for this fit) does not necessarily imply a "more than perfect" fit but is indicative of an overestimation of the errors. The chi-square probability, Q, is 0.64 for the first model (the default G312 model) and ranges from 5×10^{-4} to 1.5×10^{-15} number for the other models shown here. The principle effect of changing parameters is to increase and decrease the predicted counts – a situation that can be compensated for by changing the normalization. It can be concluded, then, that it is *possible* to fit almost *any* parameter set.

Figures 4.7 to 4.9 show contour plots of the probability, Q, as calculated from the χ^2 statistic, for each of the G302, G312, G352 fields. The fit can also be computed for combinations of these fields: for each grid point in $(\alpha_s, r_e, \rho_0^s)$ the EGM model is run for each field and the χ^2 statistics added together (*i.e.,* the sum in equation 4.1 extends across magnitude bins in each model). These are shown in figure 4.10 (for G302 and G312) and figure 4.11 (for G302, G312 and G352). In each of the figures the contours

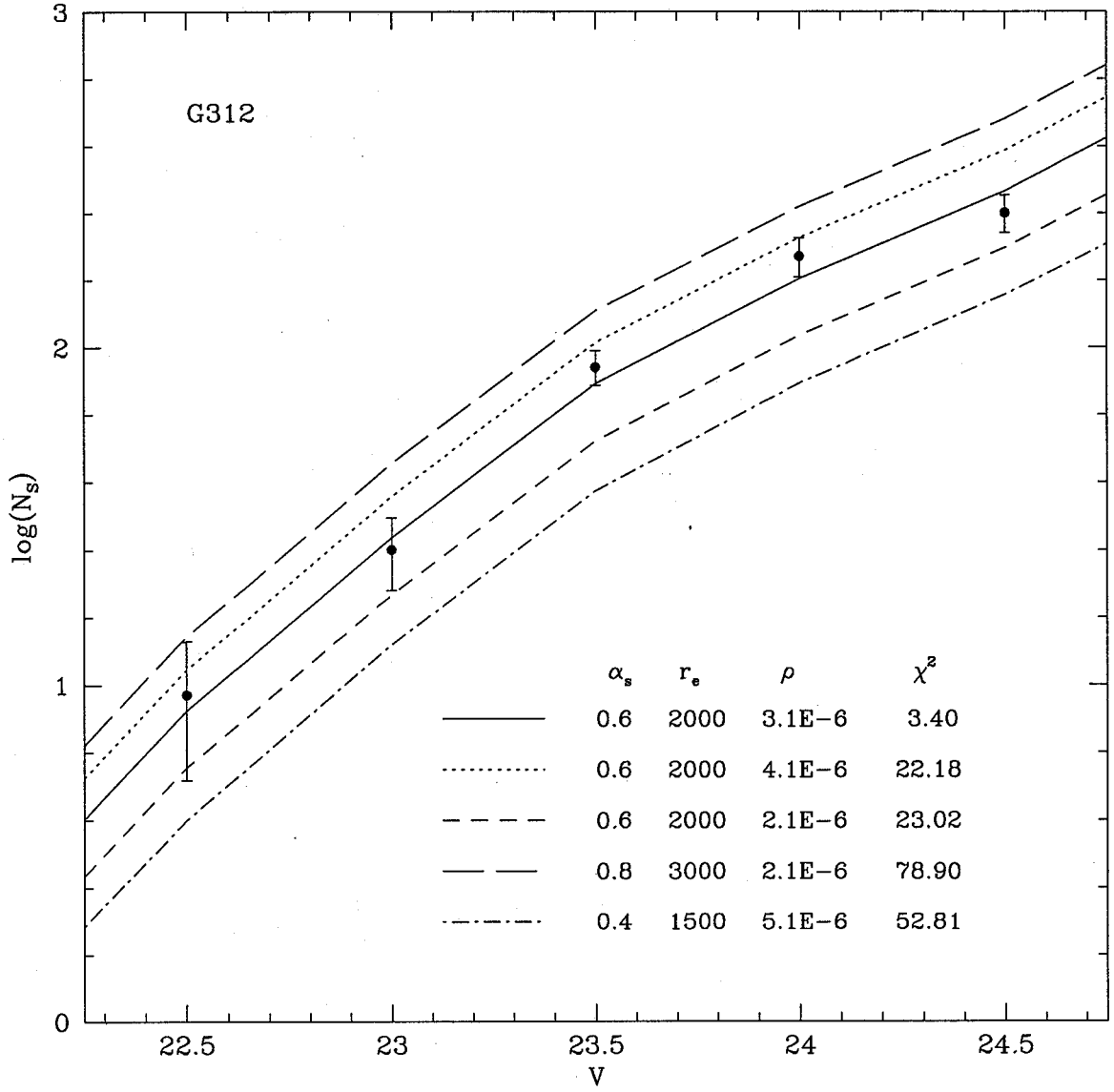

Figure 4.6: This figure shows the fit of four models to the G312 data. χ^2 refers to the chi squared statistic taken over the $V = 22.5$ to $V = 24.5$ bins.

vary from 0.1 in steps of 0.1 and the maximum value of Q for that grid is shown in the upper right-hand corner of each plot.

The models for the G302 field (figure 4.7) show that at all normalizations there is very little sensitivity to r_e. Over the density range shown the axial ratio is constrained to between 0.7 and 0.4 – values close to the default model. r_e is not strongly constrained and there is evidence for more than one best fit for the densities 5.1×10^{-6} and 5.6×10^{-6} where there is more than one peak. It is possible that this reflects the difference between the observed LF and the "mean G" LF. The "best fit" – denoted by the maximum value of Q – is approximately the same for all grids. The large value of Q for these grids is due to an overestimation of the errors.

The G312 models (figure 4.8) typically show two strong peaks – the position of these peaks can be seen to "drift" as the density normalization changes. Again, α_s seems to be constrained to between 0.7 and 0.4. r_e is constrained quite well for any particular model, but overall varies from 1250 to 3500 pc. This reaffirms the conclusions drawn earlier from figure 4.6, and from the sensitivity tests. The best fit is, as for the G302 field, reasonably constant across all the grids. The maximum is lower because the "mean G" LF does not fit the G312 observations as well as the G302 data. This can be clearly seen in figure 4.2.

Figure 4.9 shows the G352 field models. In contrast to the previous plots there is a "ridge" of high Q values containing 2 or 3 individual peaks that "drifts" across the (α_s, r_e) grid as the normalization increases. This makes it difficult to constrain any of the parameters.

The fits to a combination of the G302 and G312 fields, shown in figure 4.10 are more interesting. Comparing the broad features of this plot to previous figures it can be seen that the G302 dominates slightly because it fits the "mean G" LF better. However the addition of the G312 data "sharpens" the peaks (especially in along the r_e axis) and

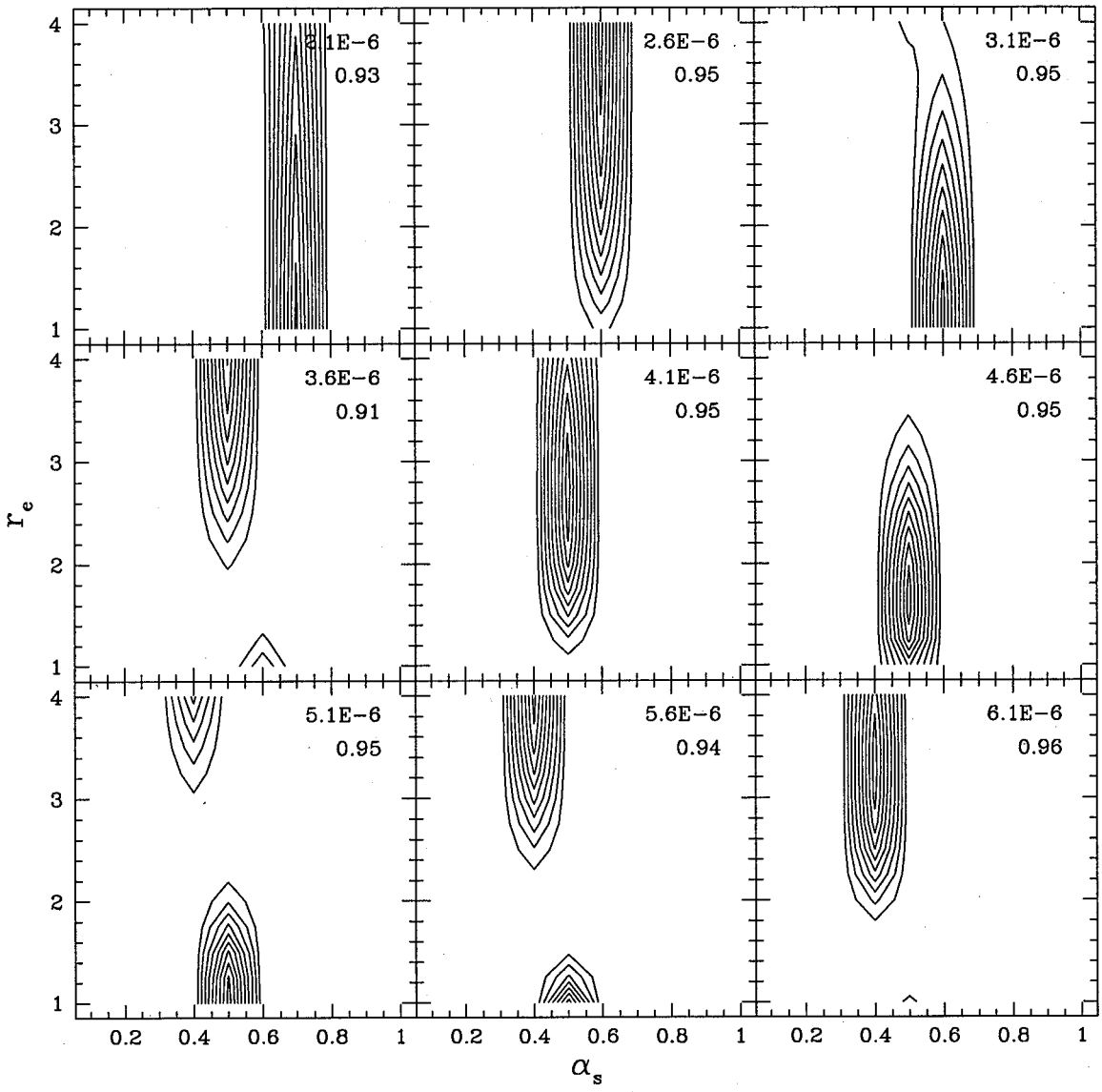

Figure 4.7: Contour plots of Q for the G302 field. Contours start at 0.1 and increase in steps of 0.1. Values of r_e are given in kpc. The "mean G" LF was used – the normalization and maximum value of Q are shown in the top right-hand corner of each plot.

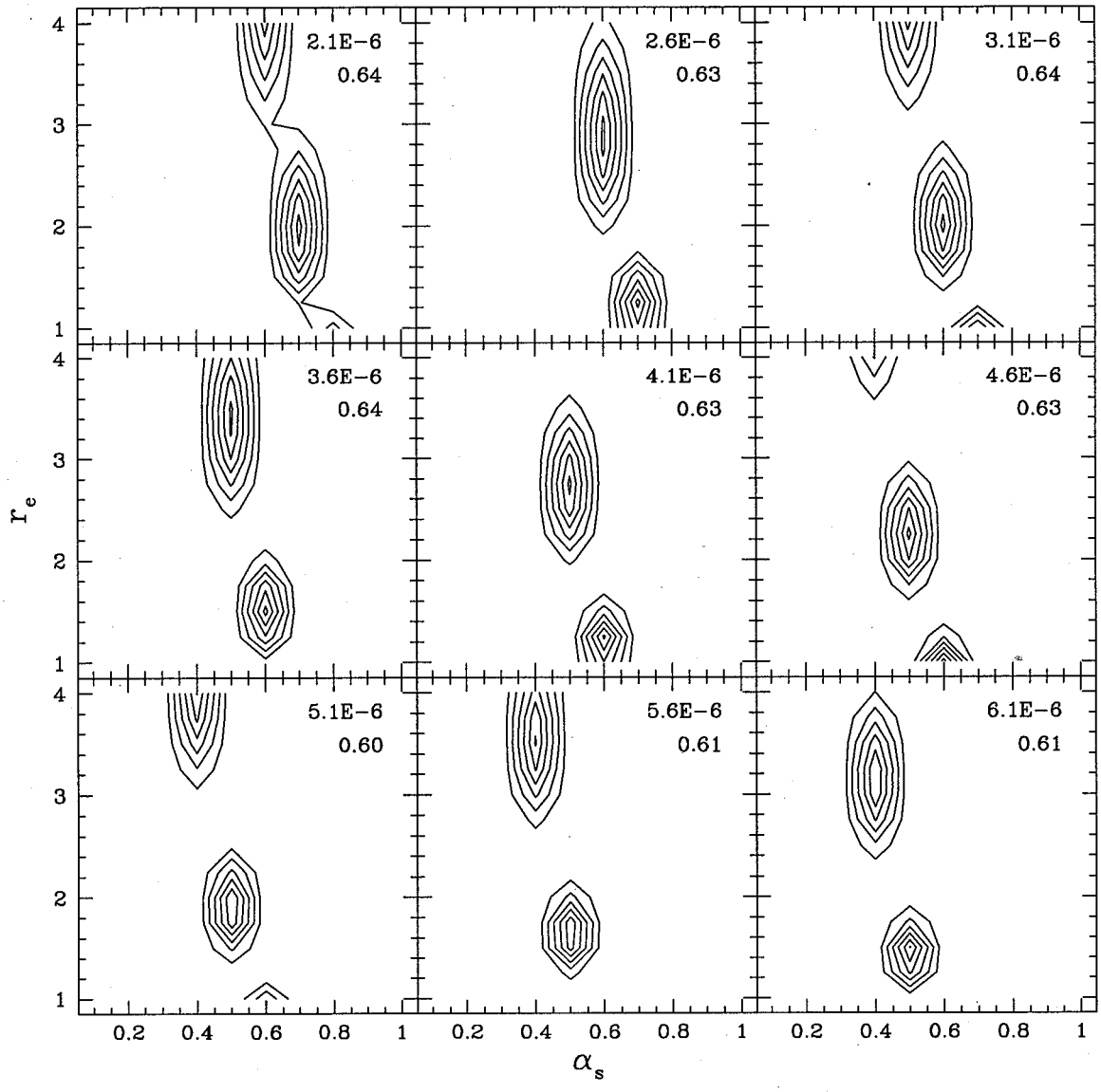

Figure 4.8: Contour plots of Q for the G312 field. Contours start at 0.1 and increase in steps of 0.1. The "mean G" LF was used – the normalization and maximum value of Q are shown in the top right-hand corner of each plot.

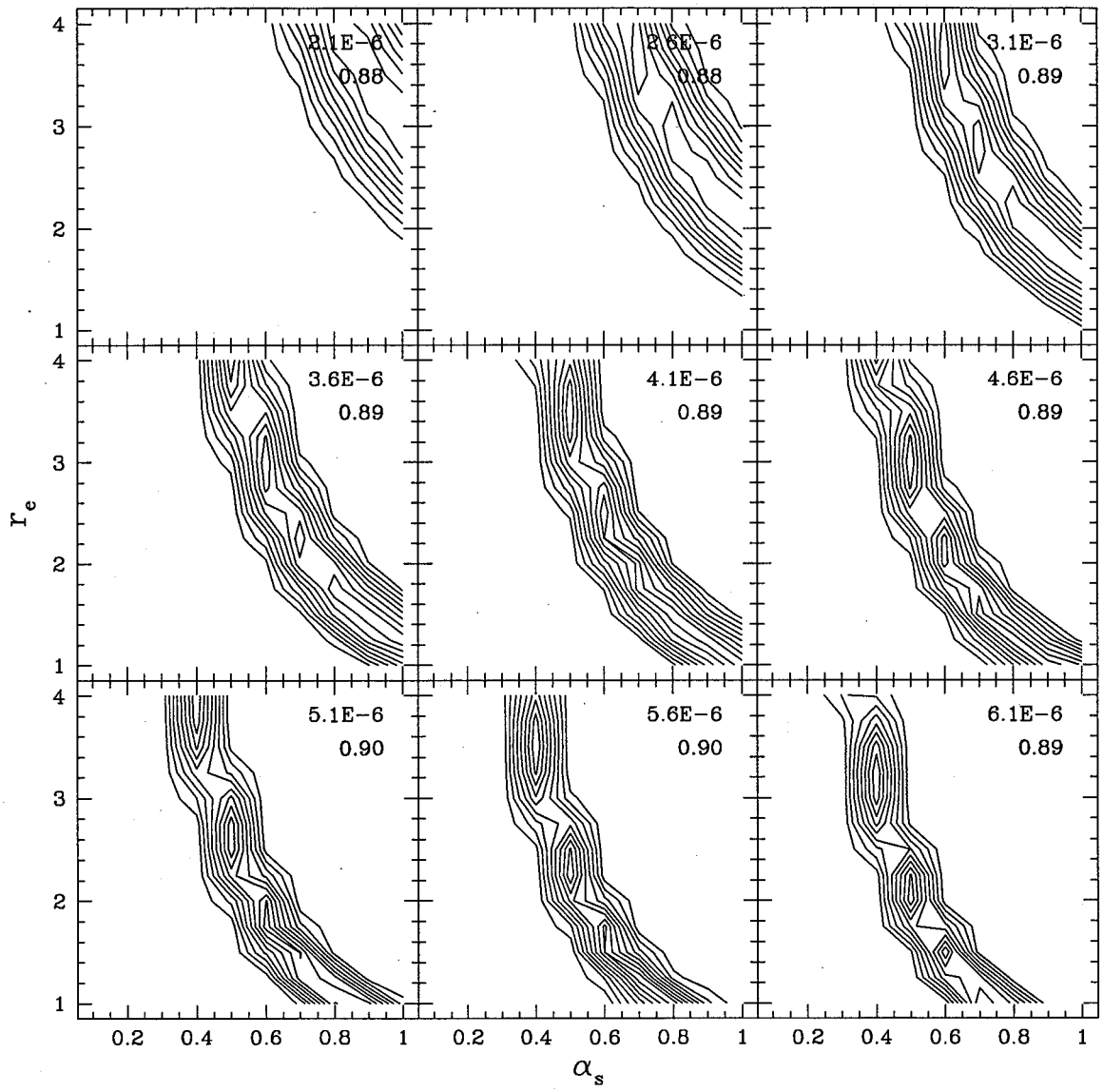

Figure 4.9: Contour plots of Q for the G352 field. Contours start at 0.1 and increase in steps of 0.1. The "mean G" LF was used – the normalization and maximum value of Q are shown in the top right-hand corner of each plot.

typically produces only one maximum. It appears to constrain r_e to between 2000 and 3750 pc.

The fits to a combination of the three fields, G302, G312 and G352, are shown in figure 4.11. This combination favours higher densities because, as has been noted before, there are too many stars in the G352 field, leading to a correspondingly higher density. It also constrains r_e to be larger than 2750 pc, though this figure should be treated with caution due to this excess in the G352 counts.

4.9 Discussion

The results described in the previous sections show that models can be used to predict star counts in external galaxies but that, unfortunately, the available data is not of sufficient quality, *i.e.,* the exposures are not long enough, and the variance between the data in different fields is too great to allow reasonable parameters to be recovered.

In addition it has been seen that changes in parameters can compensate for each other. This is illustrated in figure 4.6 which shows that changes in the density normalization, axial ratio and effective radius the all conspire to change only the magnitude of the final counts, not the shape of the luminosity function. In figures 4.7 to 4.9 the minimum χ^2 value is similar for a particular data set over a wide range of densities – though the α_s and r_e which give this minimum can vary considerably. A similar study using the DaCosta 47 Tuc LF shows a similar effect, with the mean χ^2 value being higher due to the different shapes.

Despite this, because it is possible to place limits on the axial ratio and effective radius (α_s cannot be greater than 1, for example), it is possible to place limits on how much the density normalization can be affected by these other parameters. For example when considering the G312 field, figure 4.3 shows that the density can vary by no more

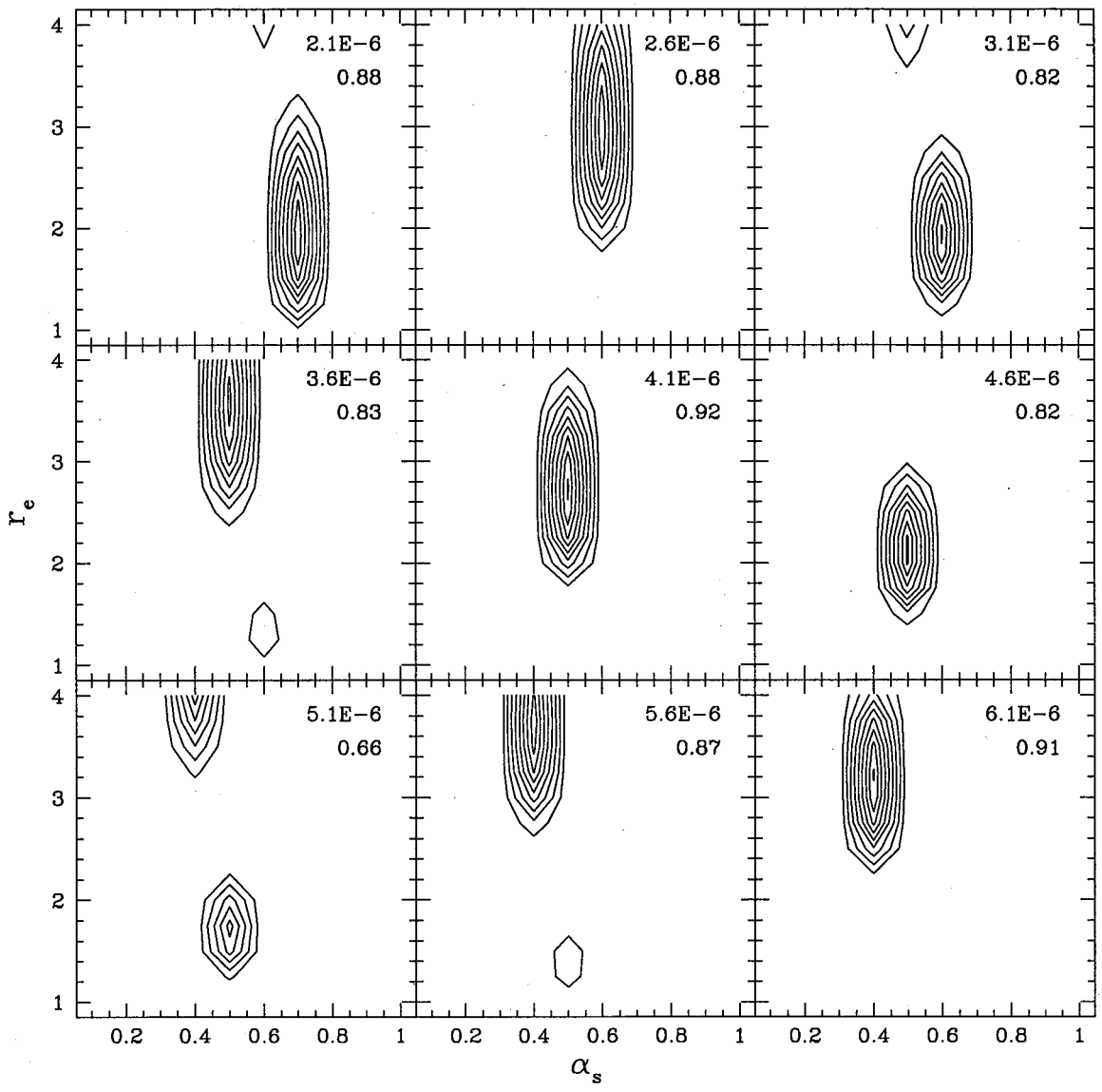

Figure 4.10: Contour plots of Q for the G302 and G312 fields combined. Contours start at 0.1 and increase in steps of 0.1. The "mean G" LF was used – the normalization and maximum value of Q are shown in the top right-hand corner of each plot.

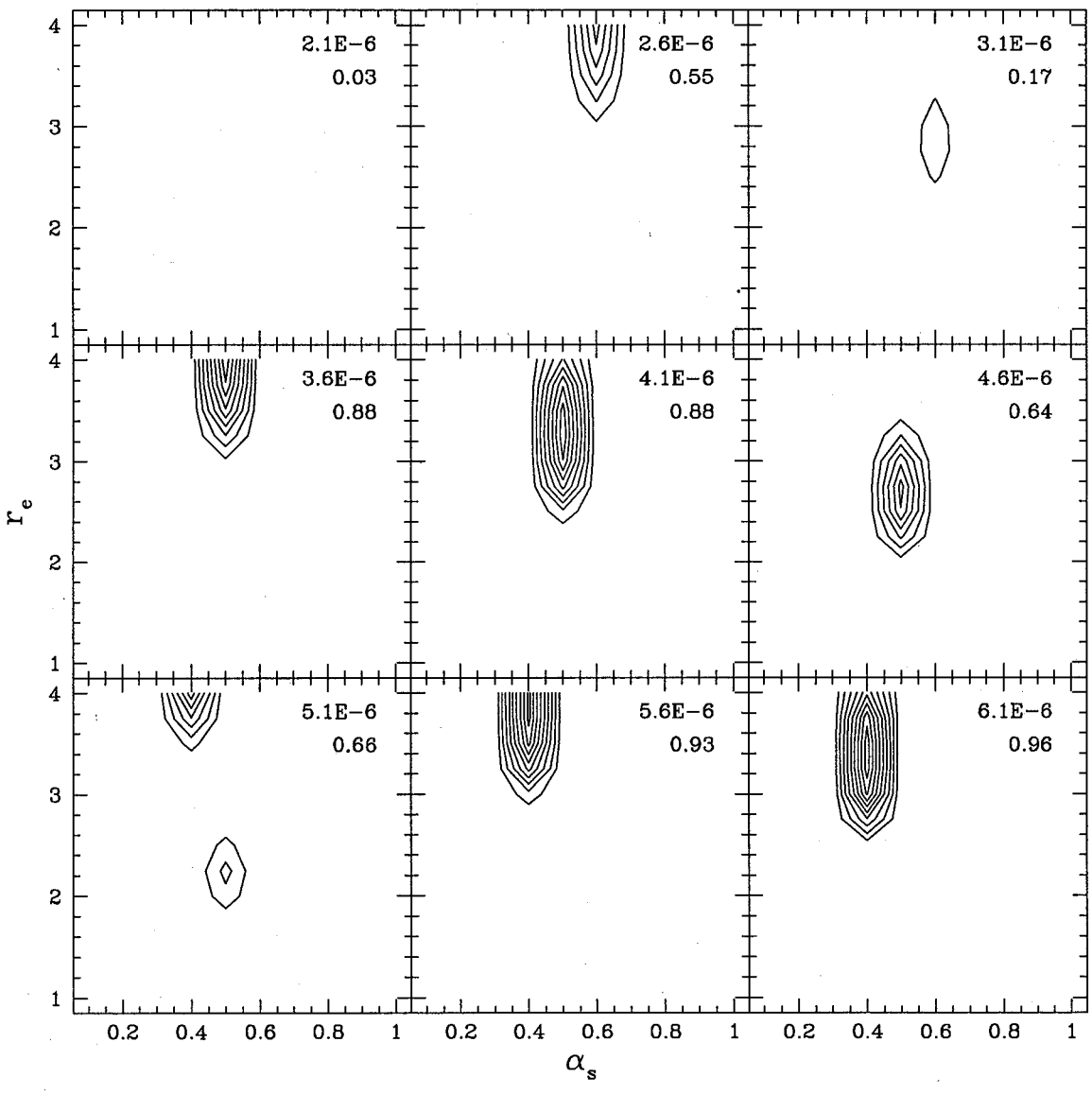

Figure 4.11: Contour plots of Q for the G302, G312 and G352 fields combined. Contours start at 0.1 and increase in steps of 0.1. The "mean G" LF was used – the normalization and maximum value of Q are shown in the top right-hand corner of each plot.

than a factor of 10, if the axial ratio of the spheroid is limited to the range $0.4 < \alpha_s < 1.0$. Similarly the effective radius of the spheroid can change the density by no more than a factor of 2 over the range 1 kpc to 4 kpc if α_s is assumed to be known (and is 0.6). When coupled together (see figure 4.5) the density can vary between approximately 1×10^{-6} and 1×10^{-5} stars pc^{-3}.

The excess of counts in the G352 field is also puzzling. If contamination by background galaxies or galaxy clusters can be ruled out then it appears that the spheroid of M31 may be inhomogenous. Interestingly enough recent work by Majewski 1992 seems to indicate that the spheroid of our own galaxy may contain similar structures – in fact it may be the case that most halo stars are part of stellar "streams", left over from structures formed or captured after the collapse of the disk. It is also possible that the excess may be due to a fluctuation in the background galaxy counts due to large scale structure. Triaxiality in the spheroid is another possibility but the spheroid would have to have an extremely non-spherical shape to account for the G352 discrepancy.

If indeed this is the case for M31 then a possible means of detection would be to obtain data for a series of halo fields covering as many different areas as possible. If the spheroid distribution is smooth (and the G352 field counts are indeed anomalous) then the de Vaucouleurs model should fit the data. Star counts from some fields may lead to a consistent solution, with other fields showing up as excesses or deficiencies in the overall scheme. It may even be the case that *no* consistent model can be found to model the spheroid of M31.

Chapter 5

Modelling the Disk

5.1 Introduction

The analysis of the disk parameters will be discussed in this chapter. From the outset the disk is harder to model than the spheroid for the following reasons:

1. The disk of M31 is known to be warped. Baade 1963 notes an asymmetry in the disk and Walterbos & Kennicutt 1987 show that the isophotes of the southern major axis exhibit a change in position angle at distances beyond 90′.

2. Spiral arms are present in the disk. WK88 compensate for the surface brightness of spiral arms by excluding those regions from the fit of an exponential profile – that luxury is not available in this analysis.

3. The spheroid was assumed to have negligible internal reddening. This is obviously not the case for any reasonable model of the disk. Unfortunately absorption in M31 is poorly known, although WK88 do present some estimates for internal reddening.

4. In some parts of the disk the stars on the far side of the plane of the galaxy from the observer will be shining *through* the disk. The effect of this, in addition to the internal absorption in the disk, is not well understood.

5. In some fields the spheroid counts will be sufficiently high that they will contribute a significant proportion of the total counts and must be subtracted from the observed

LF. However this will have to be done by assuming a density normalization from a spheroid field, assuming a set of spheroid parameters and finding the spheroid counts in that field. This will lead to a dependency of the disk results on the spheroid.

The entire issue is further complicated because the star formation history and relative number of disk and spheroid stars is bound to vary throughout the disk because of different star formation histories in and out of spiral arms.

5.2 Spheroid Contributions in Disk Fields

As noted above it is necessary to subtract the spheroid contribution from the disk counts in order to derive the disk parameters. At this stage it is useful to examine a model of the disk constructed from what are assumed to be plausible default parameters. This may be used as a stepping stone to more complex and realistic models.

The default spheroid model ($\alpha_s = 0.6$, $r_e = 2$ kpc and using the "mean G" LF normalized to 3.1×10^{-6} between $-1 \leq M_V \leq +1$) was used to generate the number of spheroid counts in the B4 field. From an examination of the CMD, this field appears to be clear of spiral arm contamination. The spheroid counts in that magnitude bin were subtracted from the B4 observed LF and the resulting number (presumed to be all disk stars) was used to normalize the Wielen LF [1] so as to reproduce the B4 observed counts at $V = 22.5$. Only the counts on the near side of the galaxy were used. Default values for the scale length and height of the exponential disk were taken to be 5500 pc (from §5.3) and 250 pc (a value comparable with that for giants in the Milky Way) respectively. The "cosecant" absorption model using the default (*i.e.*, MW parameters) was also used.

[1] See §5.4 for a more complete description of the choices for the disk LF – the Wielen LF , while not a perfect fit, is at least a good first order approximation.

Figure 5.1 shows the relative contribution along the major axis from the disk and the spheroid models using these parameters and normalizations. In panel (a) the total counts in the magnitude range $18 \leq M_V \leq 28$ are shown; in (b) only the counts at $V = 22.5$ are plotted. Note how, as might be expected, the disk dominates over the spheroid along most of the major axis (for $10 < x_0 < 150'$).

An interesting experiment can be done by modelling how the Milky Way would appear if it "replaced" M31. The EGM model was run using reasonably standard parameters for the Milky Way (see Bahcall & Soneira 1980): $\alpha_s = 0.8$, $r_e = 2670$ pc, $l_d = 3500$ pc and $h_d = 1200$ pc. The Wielen LF was used for the disk, normalized to 0.13 stars pc^{-3} between $-6 \leq M_V \leq 16.5$ at 8 kpc and the DaCosta 47 Tuc LF was used for the spheroid, normalized to $\frac{1}{750}^{\text{th}}$ of that at the same distance. (Typical values of the ratio of disk to spheroid densities in the solar neighborhood vary between 500 and 1000 to 1). The results are shown in figure 5.2. Again it can be seen that the disk stars significantly dominate the spheroid stars at distances of $x_0 < 200'$. In practice one would expect the disk counts to drop abruptly at a distance corresponding to the physical edge of the disk. M31 has measured disk isophotes out to $\sim 100\ '$ along the major axis. If the radius of the Milky Way disk component is, say, 30 kpc, this corresponds to approximately $150\ '$.

Table 5.1 compares the number of stars seen in each "B" field and in the G213 and G263 fields (and corrected for foreground stars) in the magnitude bin at $V = 22.5$ to the number of spheroid counts predicted using the default spheroid model ($\alpha_s = 0.6$, $r_e = 2$ kpc and the "mean G" LF normalized to 3.1×10^{-6} between $-1 \leq M_V \leq +1$). Also shown are the remaining disk counts and, in the last column, the number of disk stars predicted using the default parameters ($l_d = 5500$ pc, $h_d = 250$ pc) and a Wielen LF normalized to 1.5×10^{-4} (see §5.6). As noted in §3.5.5 values of the absorption parameters appropriate for the Milky Way were used, in the absence of better data.

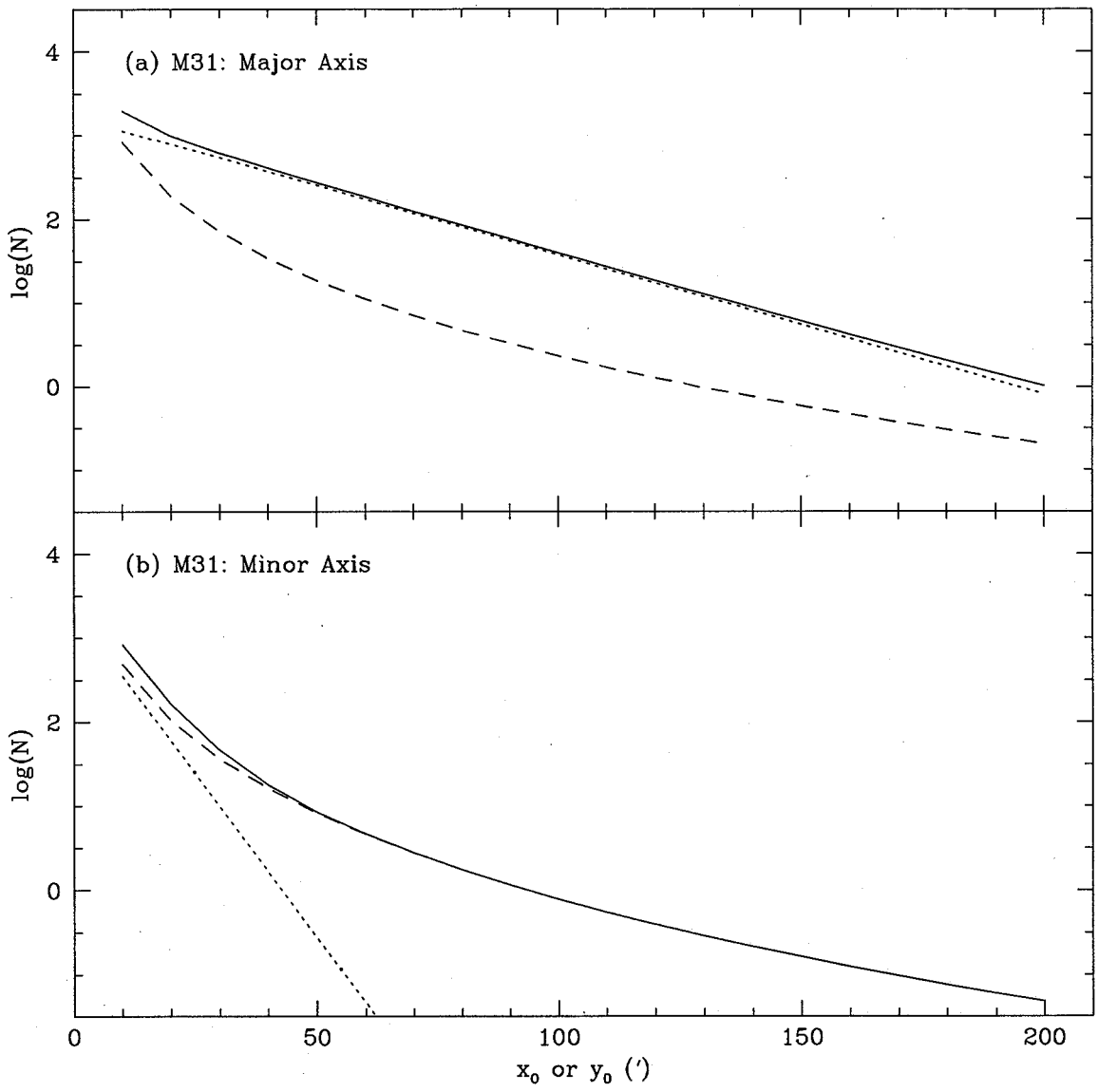

Figure 5.1: The disk (dotted line), spheroid (dashed line) and total (solid line) counts in the $V = 22.5$ magnitude bin for (a) the major axis and, (b) the minor axis. The disk LF was normalized using the B4 counts; the spheroid using the G312 observations as described in the text.

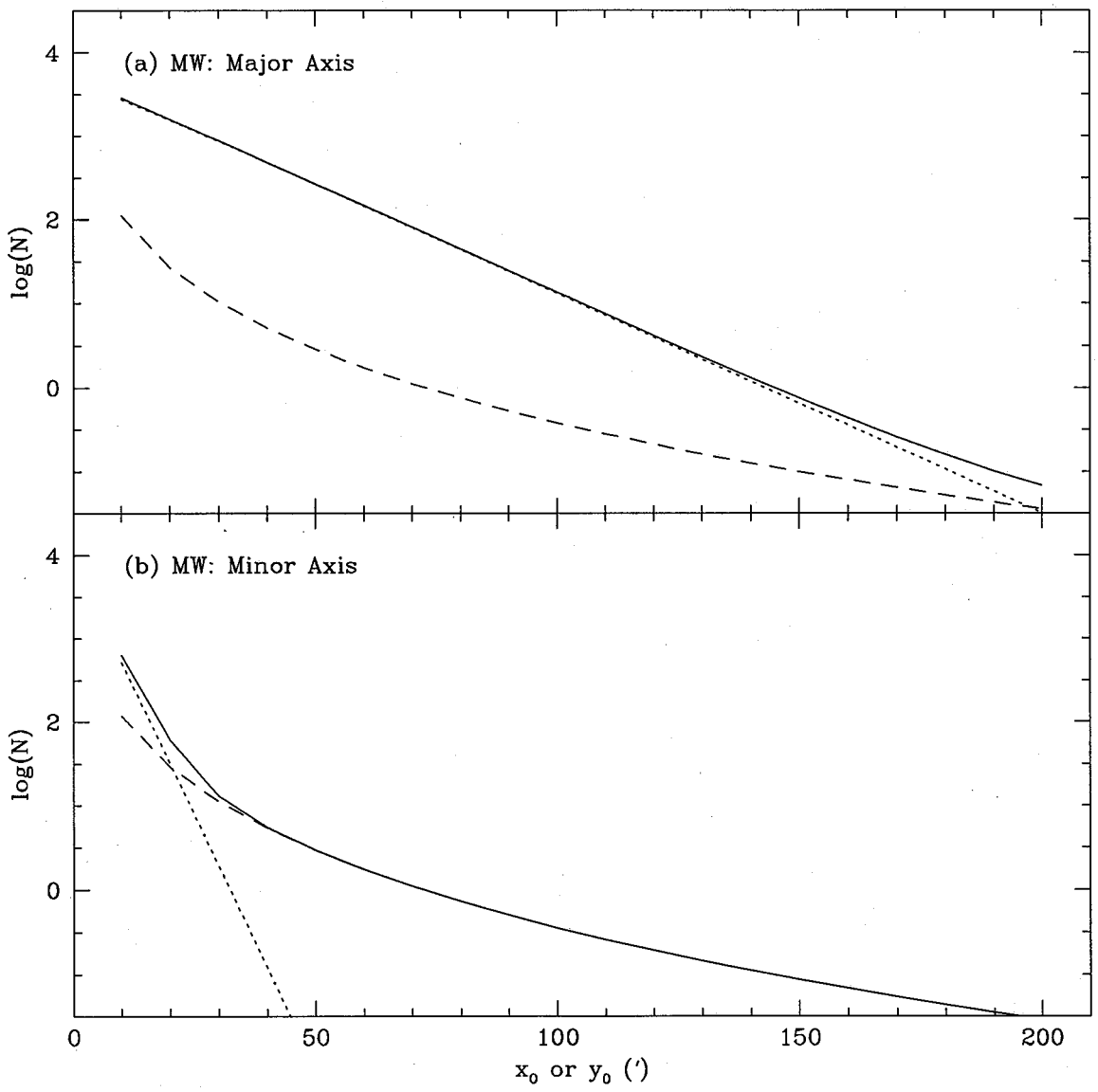

Figure 5.2: The disk (dotted line), spheroid (dashed line) and total (solid line) counts in the $V = 22.5$ magnitude bin for (a) the major axis and, (b) the minor axis for a model of the Milky Way galaxy placed at the distance of M31.

Table 5.1: Spheroid contributions to the disk fields

Field	Obsd.	Sphd.	Disk	Pred.
B1	367.0	191.1	175.9	763.2
B2	185.5	82.2	103.3	518.0
B3	284.0	26.0	258.0	260.9
B4	97.7	8.9	88.8	82.0
B5	11.6	1.0	10.6	10.3
G213	787.9	460.5	327.4	346.2
G263	146.6	121.1	25.5	73.6

5.3 Disk Counts along the Major Axis

Table 5.1 shows that there is a reasonably good match between the calculated and observed disk counts, at least for the B3, B4 and B5 fields – it should be remembered that the spheroid contribution is model dependent and that these figures are for the default model parameters. The disk counts are, by and large, of an exponential nature: figure 5.3(a) shows a plot of the raw counts in the $V = 22.5$ bin (corrected for foreground contamination) against distance from the centre of M31. A scale length of 6600 pc derived when including the B2 data; a value of 5500 kpc is obtained using the B3, B4 and B5 data only. Figure 5.3(b) plots the same counts also corrected for the spheroid contribution given in Table 5.1. This has only a small effect on the scale length if B2 is omitted from the fit (5510 pc) due to the relatively small contribution in those fields. The B1 and B2 data clearly do not fit an exponential, possibly because of the patchy nature of absorption in the disk, inter-arm gaps, and so on. WK88 obtain a value of the scale length of 5300 pc, in very good agreement with this data.

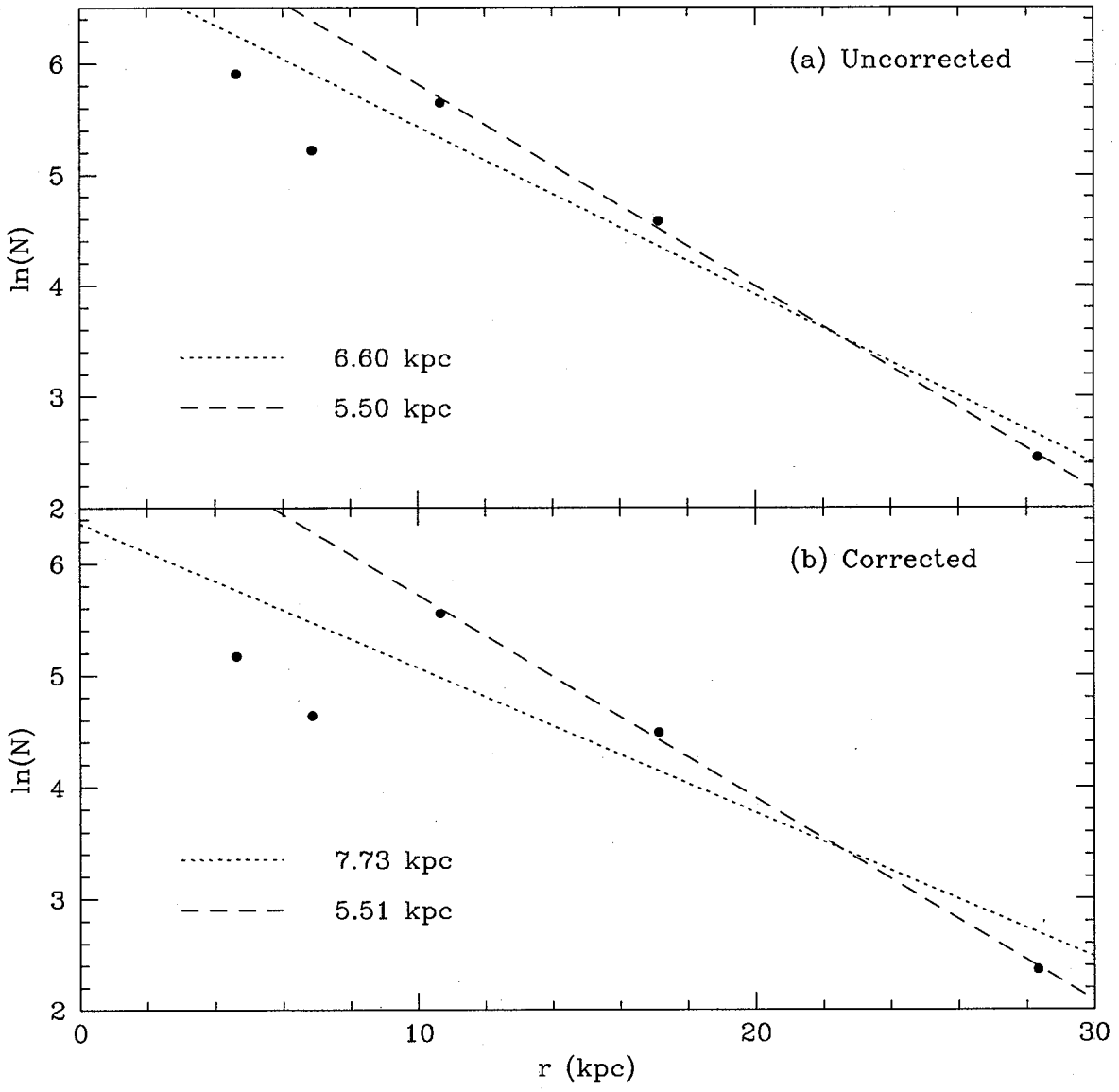

Figure 5.3: A least squares fit to (a) the uncorrected counts and; (b) the B field data corrected by the predicted spheroid counts. In each case dotted lines indicate a fit made ignoring the B2. Dashed lines are fits to only the B3, B4 and B5 data.

5.4 Input Disk Luminosity Function

In the previous sections all the models were calculated using a Wielen LF. The actual data for this LF comes from the original Bahcall & Soneira model code – it amounts to a Luyten 1968 LF based on studies of the solar neighbourhood, modified to incorporate the "Wielen dip" (Wielen 1974), and then extended to fainter magnitudes. In figure 4.5 this function is shown along with the observed LFs from the "B" fields (shifted in magnitude and normalized to the same value as the Wielen LF). The "B" data has been corrected for foreground and spheroid contamination. Bahcall & Soneira 1984 make a good case for using the Wielen LF in preference to the simpler Luyten 1968 LF, finding that it gives a much better fit to Galactic star count data.

It is obvious that the shapes of the observed disk LFs differ much more than the G302, G312 and G352 LFs differ from the "mean G" spheroid LF (see figure 4.2). These differences in shape may represent differences in the star formation history of these regions. However the Wielen LF does provide a moderately good representation of the disk LFs and will be used throughout the analysis in this chapter. This has the implication that any calculated χ^2 values may be unusually large. However the main interest is in the position in parameter space of the *minimum* χ^2, not the actual value.

5.5 Model Sensitivity

The discussion will now turn to the question of the sensitivity of the disk model to its input parameters (scale length, l_d, scale height, h_d, and inclination, i, as well the as density normalization). In a similar fashion to the spheroid tests a default model was chosen. This was the B4 field corrected for spheroid counts (as derived from the default spheroid model) using $l_d = 5500$ pc, $h_d = 250$ pc and $i = 77°.5$ and a density normalization of 1.5×10^{-4} (used to generate the disk counts for figure 5.1(a)). A "cosecant" absorption

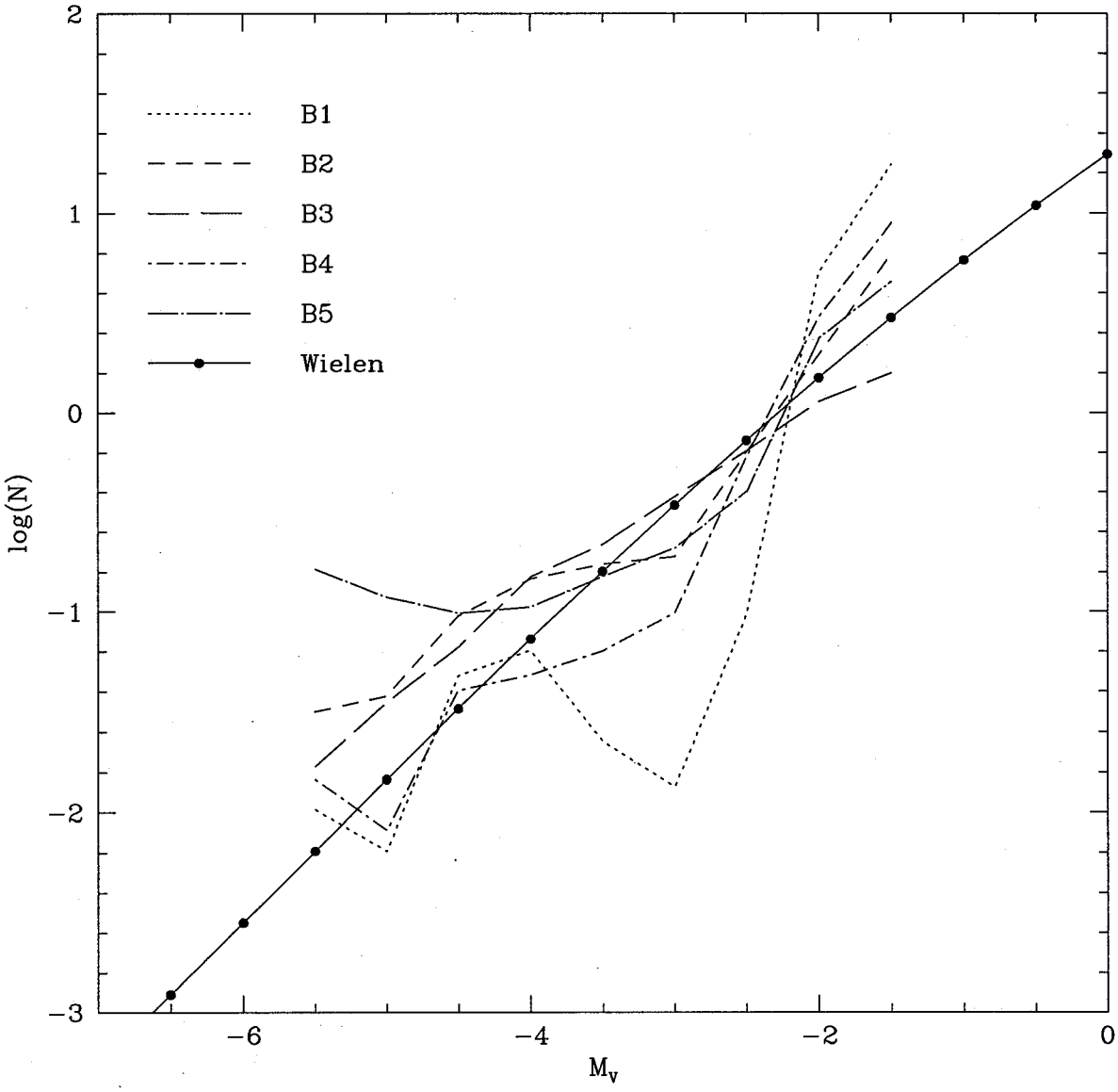

Figure 5.4: The Wielen LF is shown here (filled circles) together with the observed (and spheroid corrected) data from the "B" fields, as indicated in the legend. The observed data have been shifted in magnitude and re-normalized to the same counts in the range $-5 \leq M_V \leq -2$.

model was used in the default model and absorption parameters for the Milky Way were used. The effect of increased absorption will be to reduce the number counts at a given magnitude (as the LF shifts to fainter magnitudes) – as with the spheroid tests the important consideration here is the relative change in the counts as the parameters vary.

5.5.1 Tests with Scale Length

These first set of tests were run over 20 fields along the both axis, ranging from distances of 10′ to 200′ in steps of 10′. The scale length of the disk was varied from 2500 pc to 7500 pc in steps of 500 pc, all other variables being the same.

Figure 5.5(a) shows the variation along the minor axis with scale length. The larger the scale length, the higher the disk counts, and the further the disk extends, as might be expected. At this steep inclination, however, the even a large disk does not extend very far along the minor axis.

For the major axis test (seen in figure 5.5(b)) varying the scale length by has a large effect on the the model at all distances, changing by, for example, a factor of 19.5 at 100′. However changing the scale length a small amount (by a few hundred parsecs, say) may have a minimal effect. The intersection of the models occurs at $x_0 \approx 47'$, or 9870 pc.

5.5.2 Tests with Scale Height

The next test (shown in figure 5.6) shows the variation with scale height, h_d, for the minor axis (a) and major axis (b). The scale height was varied from 50 to 1050 pc in steps of 100 pc.

The minor axis tests, shown in figure 5.6(a), reveal that changes in h_d will have large effect on the observed number counts, but only in a limited range of distances. The variation between $h_d = 50$ and $h_d = 1050$ pc at $x_0 = 20'$ is by a factor of approximately

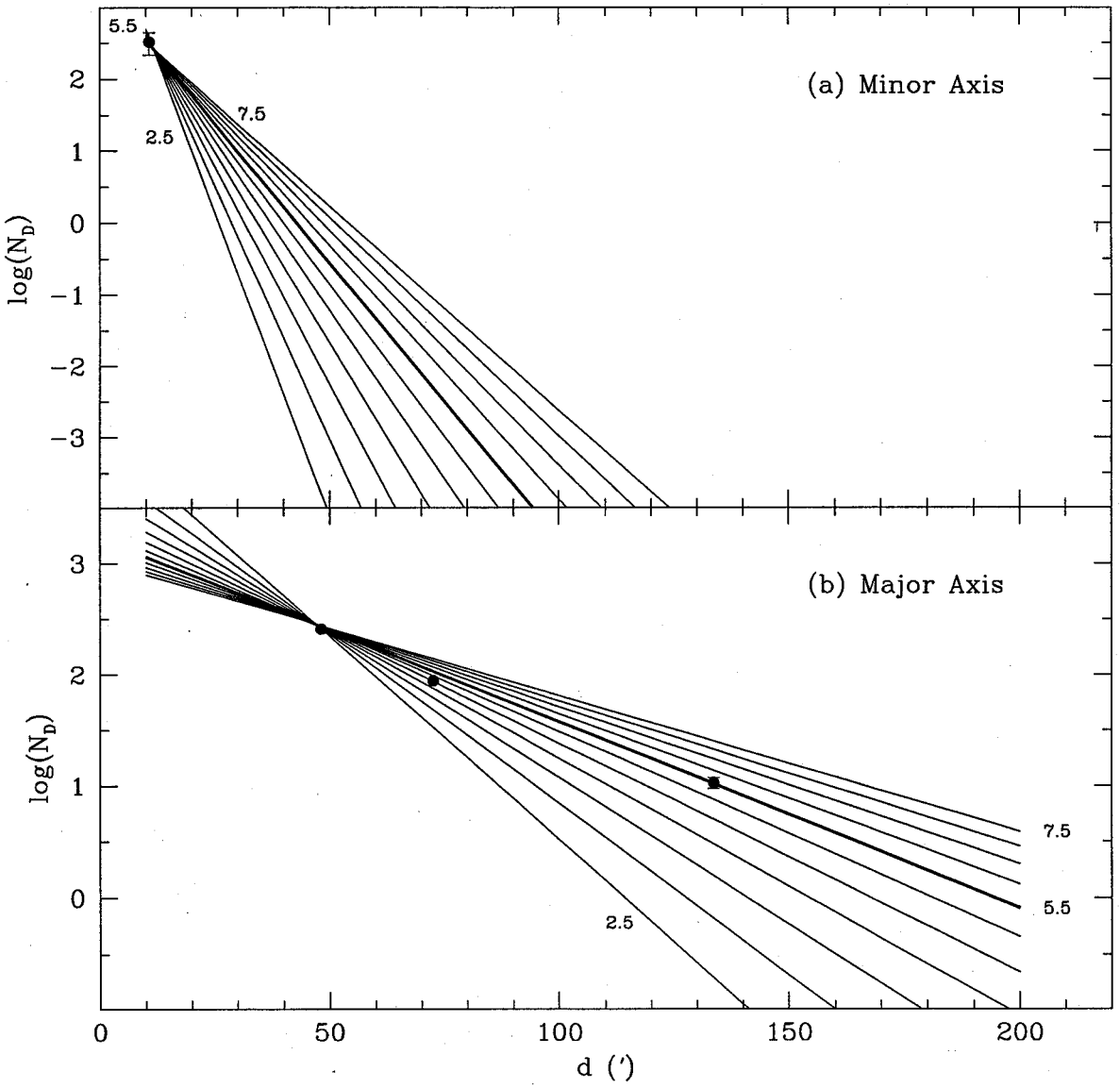

Figure 5.5: The variation of number counts (for the $V = 22.5$ bin) with scale length, l_d, for (a) the minor and; (b) the major axes. The first, last, and default models are labelled with the scale length in kpc. In (a) the counts in the $V = 22.5$ bin for the G213 field have been plotted; in (b) the B3, B4 and B5 counts are shown.

34 but beyond 100′ along the minor axis the disk has effectively vanished because M31 has a small (12°.5) inclination to the line of sight.

The counts along the major axis (at the default inclination) are comparatively insensitive to changes in disk scale height, changing only by a factor of 8 to 10 over the entire major axis. The effect of changing the scale height diminishes as the scale height increases, reflecting the decrease in density of the disk component.

5.5.3 Effects of Inclination and Absorption

The tests for changes in inclination are not shown – the inclination in all the remaining models is set to 77°.5. However the model does behave as expected to changes in i. Along the minor axis the changes in number counts will depend on the scale height as well as the inclination. For the default scale height and at a minor axis distance of 20′ the counts change by a factor of 11.6 over a range of inclinations from 0° (face on to the observer) to 80°. At 40′ this ratio has increased to 460 as the inclination becomes lower (more "face on") the counts increase more further out along the axis as the line of sight travels through more of the disk. Along the major axis the effect is constant (the ratio being 0.4) because there is no scale length in the absorption model

The effects of absorption and internal reddening in the disk of M31 will obviously have an effect on the observed LF . However the determination of the exact absorption parameters (as described in §3.5.3) is not well understood. Noting that WK88 find that M31 has a similar reddening law to the Milky Way, this test is conducted using the same absorption parameters for our own Galaxy. The results will be a reasonable first approximation. Applying this absorption model reduces the counts at a given distance by a factor of 1.97 for "cosecant" absorption and 2.04 for the Sandage model. This is a large effect considering that the scale height is set to 250 pc but it must be remembered that the disk is highly inclined and the line of sight will pass through a significant fraction

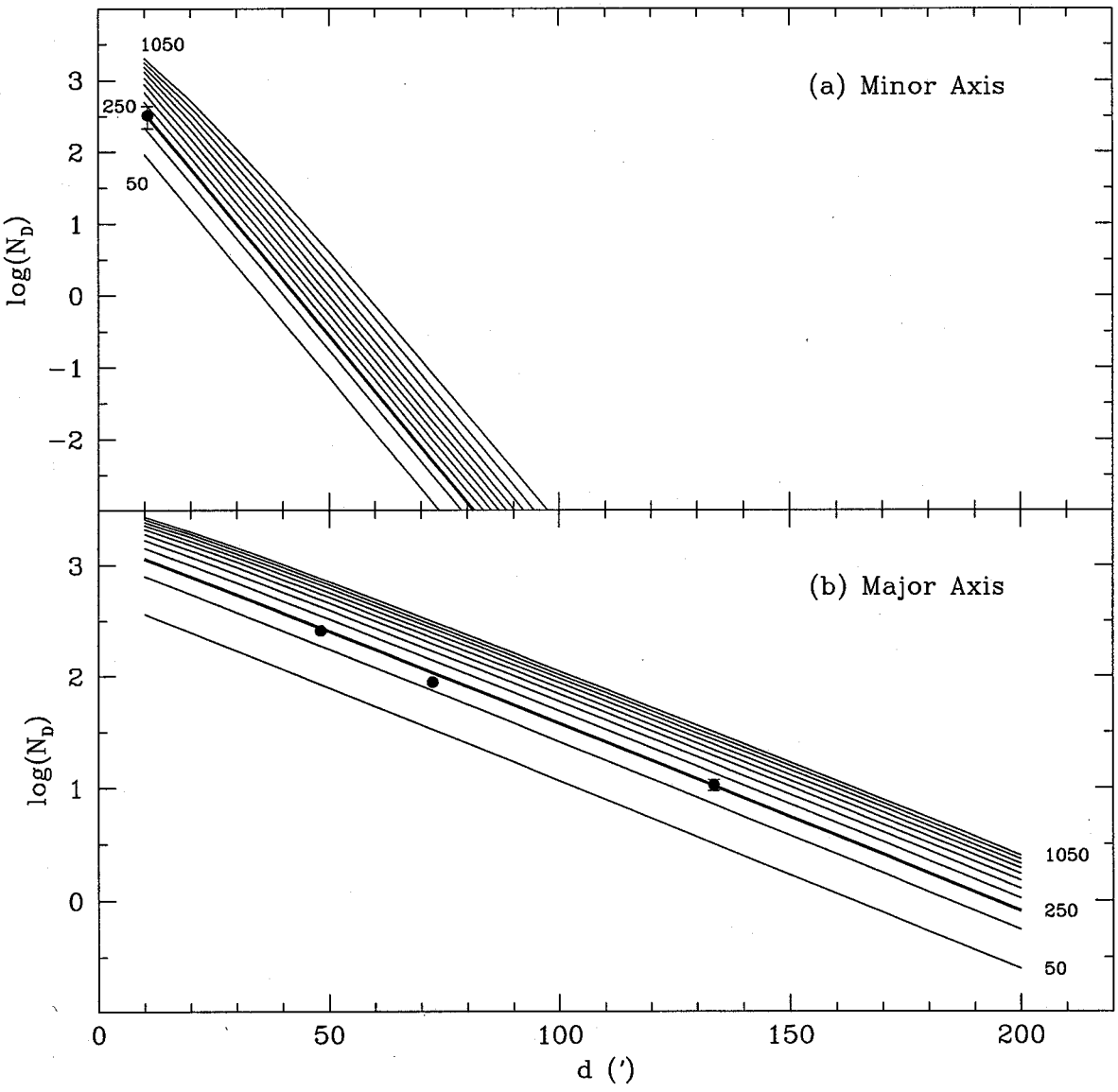

Figure 5.6: The variation of number counts with scale height, h_d, for (a) the minor and; (b) the major axes. The first, last, and default models are labelled with the scale height in pc. In (a) the counts in the $V = 22.5$ bin for the G213 field have been plotted; in (b) the B3, B4 and B5 counts are shown.

of the dust, even if it is confined to regions near the plane. Of course, this does allow for tremendous leeway in fitting the model – in the extreme each disk field could be modelled with a different set of absorption parameters.

Changing the "cosecant" absorption model parameters causes the model to behave as one might expect. For example, halving the absorption scale height, a_0, to 50 pc reduces the counts to 88% of the default model along the major axis. Increasing it to 250 pc increases the counts by a factor of 1.23. Halving the coefficient, a_1, reduces the counts by 57%.

5.6 Initial Density Estimates

As has been mentioned before, the normalization of the input LF is very important to the success of the model fitting the data. An initial estimate of the density normalization for the default model (l_d = 5500 pc, h_d = 250 pc) was made for each field, using the Wielen LF discussed above. As with the spheroid, the normalization was performed over the range $-1 \leq M_V \leq +1$ at a distance of 10 kpc. In each case the LF was scaled to a value of 1.0 over this range and the resulting number counts used to determine the normalization that would return the correct counts in the $V = 22.5$ magnitude bin. The values obtained were:

B1: 3.46×10^{-5} stars pc^{-3}

B2: 2.99×10^{-5} stars pc^{-3}

B3: 1.48×10^{-4} stars pc^{-3}

B4: 1.62×10^{-4} stars pc^{-3}

B5: 1.55×10^{-4} stars pc^{-3}

G213: 1.42×10^{-4} stars pc^{-3}

G263: 5.20×10^{-5} stars pc^{-3}

The values returned by the B3, B4 and B5 fields are quite consistent, the G213 density (along the minor axis) is also in good agreement. In the following discussion a value of 1.5×10^{-4} (between $-1 \leq M_V \leq +1$ at a radius of 10 kpc) will be used as a default

model density.

It is of interest to compare these densities to the values derived for the spheroid, and to compare the ratio of these two to the density normalizations obtained for the solar neighbourhood. The ratio of disk to spheroid density over the magnitude range $-1 \leq M_V \leq +1$ is 48.4 at 10 kpc. The LFs used for each component are, however, of different shapes. Using these density values to normalize the LFs it is possible to calculate the density over the range $-6 \leq M_V \leq +16.5$, *i.e.*, down to the H–burning limit. The spheroid density is then 1.4×10^{-3} and the disk density is 7.5×10^{-2} pc^{-3} leading to a ratio of 53.6.

Wielen 1974 gives a normalization for the Wielen LF of 0.13 stars pc^{-3} down to this limit. Bahcall, Schmidt & Soneira 1983 derive a density of the spheroid of from $(1 - 9) \times 10^{-4}$ stars pc^{-3} depending on the model being used. This leads to a disk to spheroid density ratio, at 8 kpc, of between approximately 1300:1 and 140:1, although the lower limit usually used is about 500:1.

It appears then that the spheroid of M31 is more massive than the Milky Way's whilst the disk is *less* massive, leading to a relative normalization about an order of magnitude lower than that of the Galaxy. However it should be noted that a direct comparison between the Milky Way densities *observed* in the solar neighbourhood (at 8 kpc) and the M31 densities *predicted* at 10 kpc may not be completely meaningful. Possible reasons for this apparent discrepancy may include: the different sizes of the galaxies; the differences in disk and spheroid parameters; possible differences between the MW and M31 luminosity functions (recall that only the giant branch is being observed here); and the difficulty in observing a "clean" disk sample in M31.

5.7 Parameter Grids

To more fully investigate the properties of the B4 field disk counts models were run over a grid of density normalizations, scale lengths and scale heights. The scale length, l_d, was varied from 2500 pc to 7500 pc in steps of 500 pc; the scale height, h_d, was varied from 50 pc to 1050 pc in steps of 100 pc. Nine density normalizations were used for the Wielen LF (in the range $-1 \leq M_V \leq +1$) ranging from 5.0×10^{-4} stars pc^{-3} to 2.5×10^{-4} in steps of 2.5×10^{-5} stars pc^{-3}.

The resulting grids for the B3, B4 and B5 fields are shown in figures 5.7 to 5.9 respectively. Figure 5.10 is a fit to a combination of those three fields. Unlike the spheroid models, these grids plot χ^2, not Q. This is because even the minimum χ^2 values are quite large: the Wielen LF is not as good a fit to the B field data as the "mean G" LF is to the spheroid fields. The contours for each field have been chosen to highlight the "valley" of minimum χ^2 values. The fits were made over the range $21.5 \leq V \leq 23.0$ using equation 4.1. Poisson ($\sqrt{N}$) errors were applied to the raw counts, propagated by the area scaling factor (0.10022) and used as an estimate of σ_N. Foreground star counts and spheroid counts from the default model were used as the contaminants.

The χ^2 fits to the B3 data are shown in figure 5.7. At higher density normalizations the scale height is quite well constrained between 50 pc and 1000 pc. However the entire range of tested scale lengths fits this data. Figure 5.8 shows the results for the B4 field. Unfortunately neither the scale length or the scale height is constrained very well at all, the minimum χ^2 values lying diagonally across the (l_d, h_d) grid. The results for B5 (figure 5.9) are similar, though the fit is generally better with a minimum $\chi^2 \approx 5$.

Figure 5.10 shows the results of fitting all three of the B3, B4 and B5 data simultaneously. Although even the minimum χ^2 is questionably large, it appears to constrain h_d between 50 and 400 pc *and* the scale length, l_d, between approximately 5 and 7 kpc.

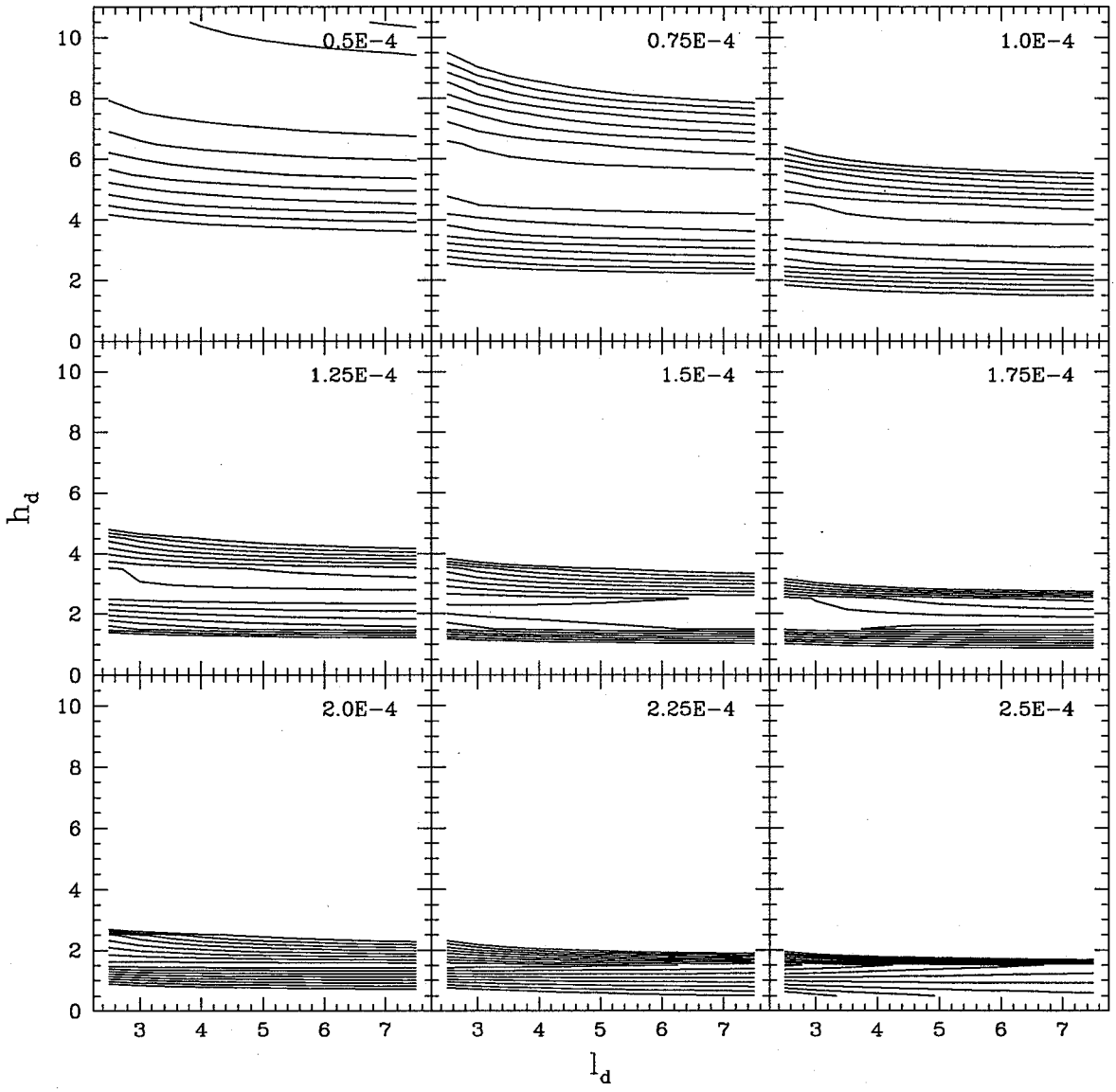

Figure 5.7: This figure shows contours of χ^2 for the B3 field over a grid of scale length in kpc (l_d) and scale height (h_d) in 100 pc units. Contour levels range from 200 to 1000 in steps of 100. The Wielen LF was used – the density normalization is shown in the upper right hand corner of each panel. The fit was made to observed counts in the range $21.5 \leq V \leq 23.0$.

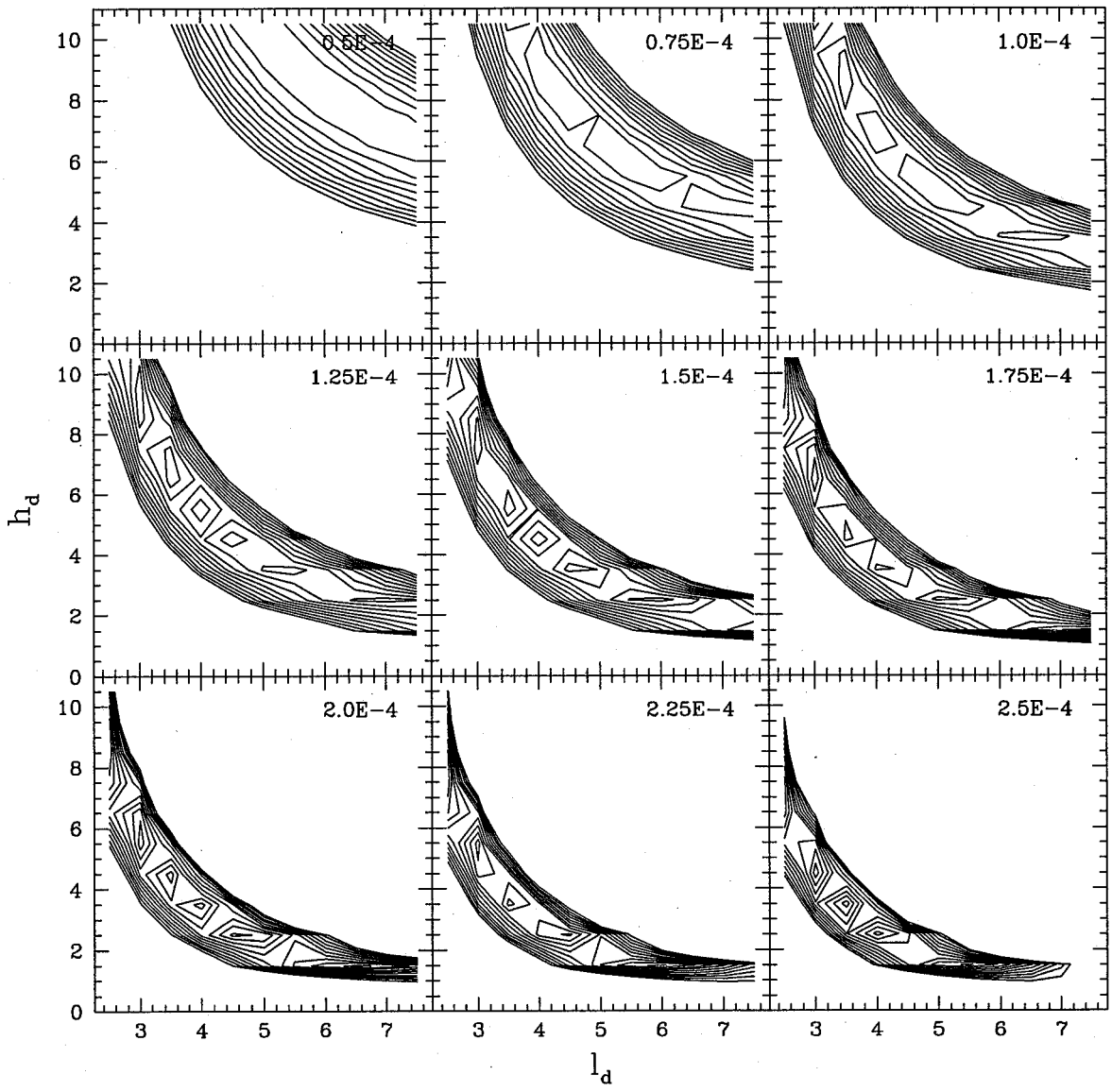

Figure 5.8: This figure shows contours of χ^2 for the B4 field over a grid of scale length in kpc (l_d) and scale height (h_d) in 100 pc units. Contour levels range from 300 to 500 in steps of 20. The Wielen LF was used – the density normalization is shown in the upper right hand corner of each panel. The fit was made to observed counts in the range $21.5 \leq V \leq 23.0$.

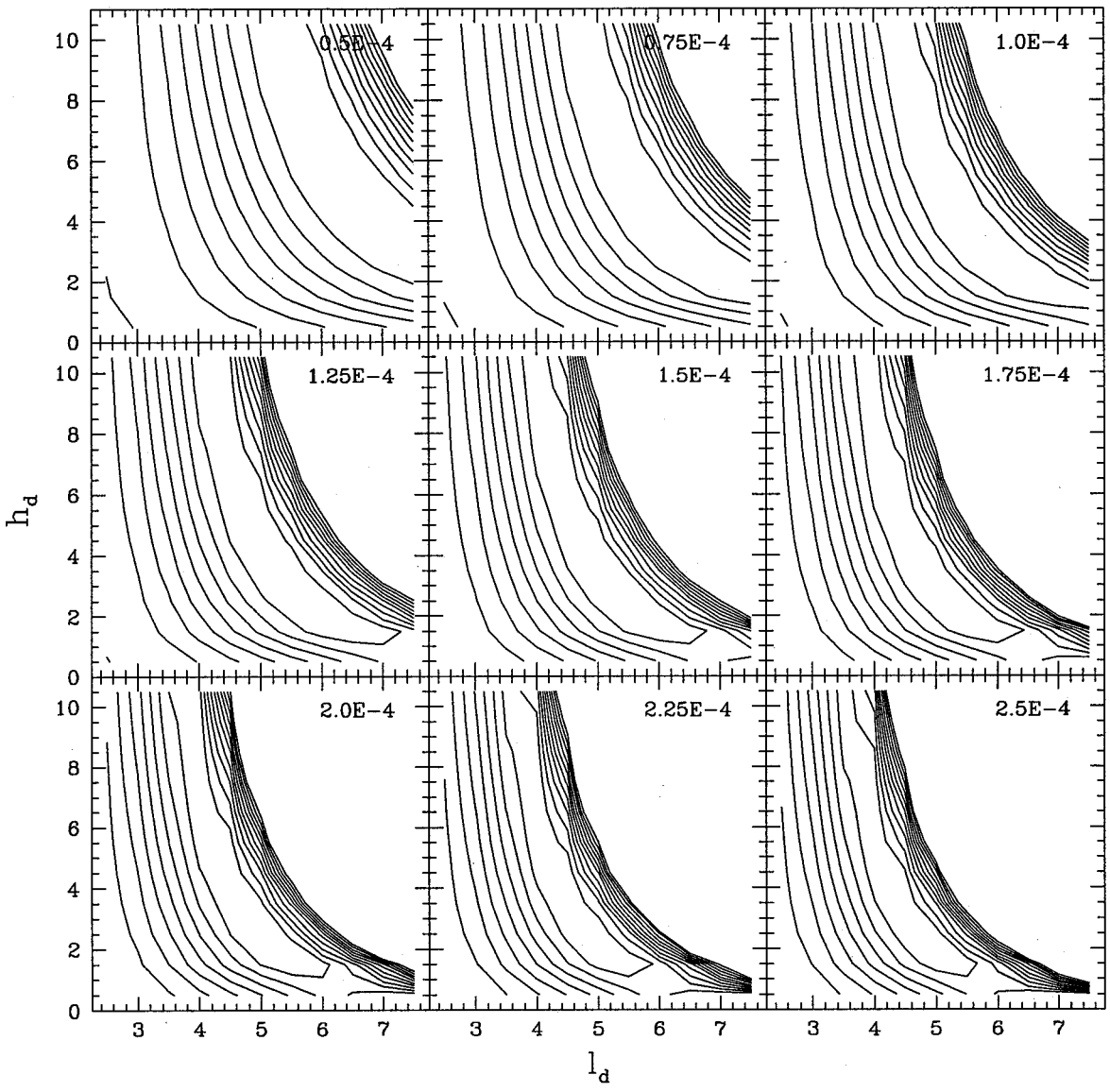

Figure 5.9: This figure shows contours of χ^2 for the B5 field over a grid of scale length in kpc (l_d) and scale height (h_d) in 100 pc units. Contour levels range from 4 to 104 in steps of 10. The Wielen LF was used – the density normalization is shown in the upper right hand corner of each panel. The fit was made to observed counts in the range $21.5 \leq V \leq 23.0$.

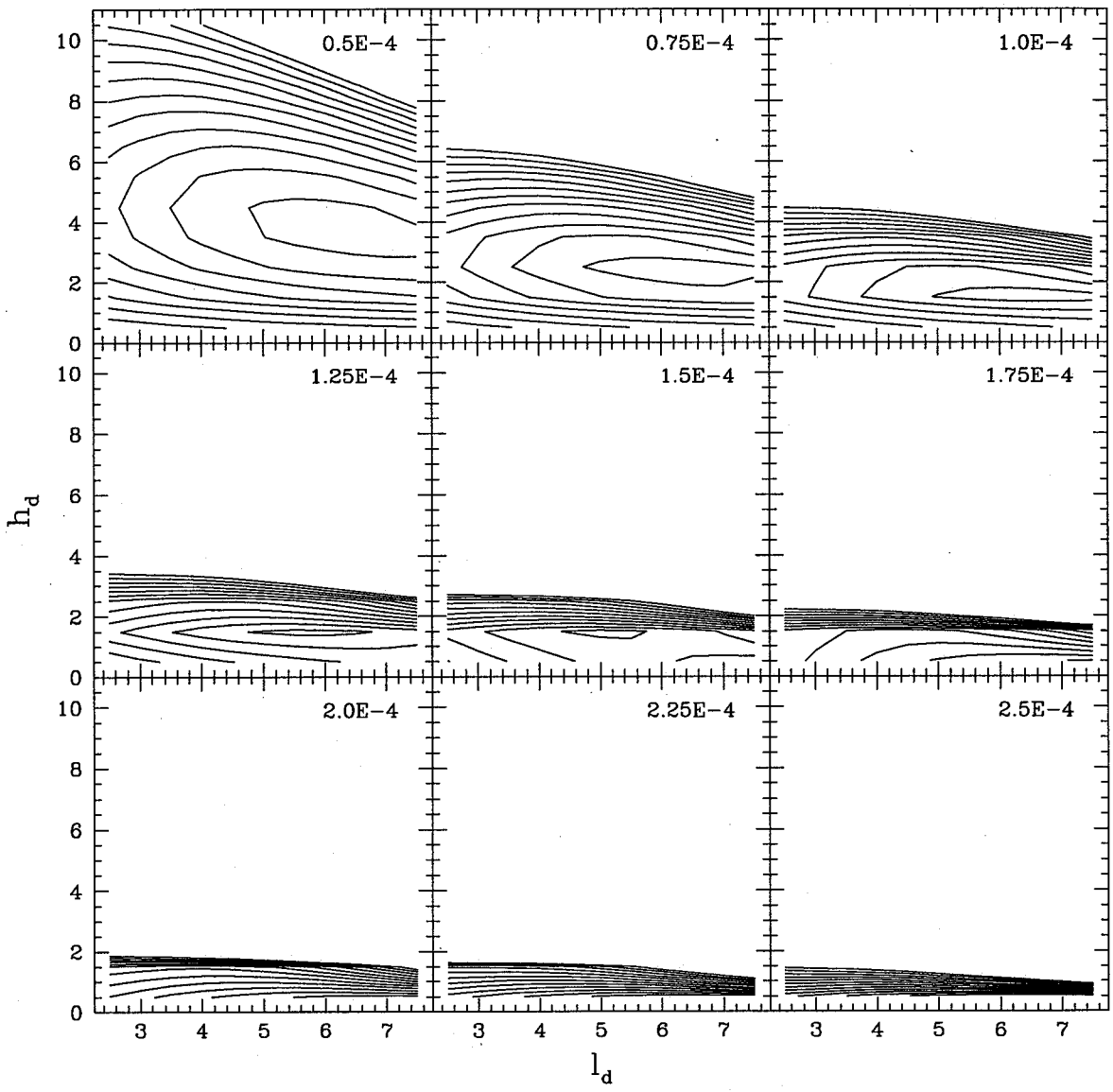

Figure 5.10: This figure shows contours of χ^2 for the B3, B4 and B5 fields combined over a grid of scale length (l_d) in kpc and scale height (h_d) in 100 pc units. Contour levels range from 2500 to 3500 in steps of 250. The Wielen LF was used – the density normalization is shown in the upper right hand corner of each panel. The fit was made to observed counts in the range $21.5 \leq V \leq 23.0$.

5.8 Discussion

The analysis of the disk of M31 can be summed up in one word: difficult! The choice of appropriate spheroid parameters (in order to correct the counts to true disk counts) is critical. In addition, the inhomogenous character of the disk itself conspires to complicate the problem. In some respects studies of the surface brightness distribution rather than star counts may be better suited to the determination of the properties of the disk because a smooth average over large portions of the disk can be taken (see, for example, WK88).

The spheroid counts appear to be so high because the assumption that all, or most, of the giant stars seen in these fields belong to the disk population is not necessarily true. The actual proportion of disk giants to spheroid giants will depend heavily on the star formation history in that region of the galaxy and deconvolving the two populations will require this information. The studies of the disk of M31 that use integrated light and surface brightness profiles do not suffer from this problem because most of the disk light comes from dwarf stars, which considerably outnumber the giants.

In order to effectively use this kind of star count analysis on the disk fields one must either obtain data that reaches extraordinarily faint magnitudes, or one must use a bright "tracer" of the (old) dwarf population whose relative proportion amongst the disk is well known. Rose 1985 has used RHB stars to find evidence for a thick disk in the Milky Way, but this has been criticised by Norris & Green 1989 because it is difficult to distinguish between them and core He burning "clump" stars. These types of studies in M31 are likely to remain technically infeasible for quite some time. It has also been assumed that there is no contribution to the disk counts from stars on the far side of the galaxy shining through the disk. Inclusion of this effect may also improve matters but it will be difficult to derive the parameters for the absorption.

Chapter 6

Conclusions

The EGM code as described in Chapter 3 has been successfully developed and implemented. Tests have shown that it can be used to reproduce and predict counts in various fields in M31. However, the use of the code to derive parameters for the disk and the spheroid depends heavily on the data available. The data on the spheroid counts can be used directly (under the assumption that the spheroid LF , axial ratio and effective radius does not change with radius) because there are few complications involved when looking at this component. Modelling the disk is much more challenging – the disentanglement of the disk and spheroid giants, the knowledge of the proportion of giants to dwarfs in each component, and the effects of different star formation on different fields is a very complex problem and cannot be attempted in this work with the data currently available.

A more precise determination of the spheroid parameters using the EGM code is quite feasible but requires better data. In particular the data set should be as homogeneous as possible – exposure times should be the same in each field to ensure that incompleteness estimates are only affected by crowding. In addition to data along the minor axis a study along a "diagonal" (between the major and minor axes) is required to make a more accurate determination of the spheroid axial ratio. Finally, background fields of the same exposure time should be taken to remove foreground star and background galaxy contamination directly without resorting to modelling their contributions.

Majewski 1992 has studied the dynamics of stars in the Milky Way near the North

Galactic Pole using proper motion measurements. As well as evidence of a thick disk component dominating at heights of 1 kpc to 5.5 kpc above the plane he notes the presence of a "moving group" of spheroid stars. This group of stars occupies a very distinct region in velocity space at a height of $\sim$ 4550 pc above the galactic plane. This seems to indicate that the galactic spheroid is not homogeneous – possibly the result of a formation scenario similar to the Searle & Zinn 1978 model.

To determine if this is indeed the case for the Andromeda Galaxy it would be necessary to conduct a systematic survey of the spheroidal component of M31. Very deep exposures would not be necessary as long as a sufficient number of stars was recorded. The fields would be distributed over the region around M31 in a grid-like pattern – the number of these "grid points" and their spacing would select the scale of structure that could be detected. Because the nature of these inhomogeneities would be essentially stochastic it might be the case that even an extensive survey would miss any deviations from a smooth distribution of stars. However if the "background spheroid" distribution is itself patchy then it may have a reasonable chance of success. Using CFHT, for example, to completely map out the halo in one quadrant of M31 (as seen from the Earth) out to a distance of 100′ would require approximately 150 FOCAM frames if a 2048 $\times$ 2048 CCD was used. Clearly this is a massive undertaking and reducing the coverage of the grid then sets limits on the sizes of deviations that can be detected.

It has been demonstrated that modelling the disk counts is problematic. The contamination of the disk giant sample by the spheroid giants seems to preclude any simple analysis because the relative numbers of giants to dwarfs is likely to change with position in the disk. Varying star formation histories and the possibility of an inhomogenous spheroid compound the problem. It seems as if the only way to successfully determine disk parameters is to sample the dwarf population directly or to discover and use a luminous tracer of the old disk population. In the latter case the relative numbers

of this "tracer" component and the disk component would have to be well known, and variations with star formation history would still have an effect. It should be noted that these problems will be particularly acute if the galaxy is face-on, such as M33, which is another possible candidate for this sort of study. In this case there will be no "pure" spheroid field whose fit can be subtracted from the disk fields. This presupposes that M33 has a significant spheroid.

It was hoped initially to detect and determine the parameters of a thick disk component in M31. With the data currently available this is not possible. The problem of separating two components with a similar scale height is still present. This is compounded with the problem noted for the disk analysis – if a thick disk is present then *three* sets of LFs and density distributions must be de-convolved. This would only be possible if both the spheroid and the disk components were well known in that field so that any deviations from the two component model could be detected. This would require that the spheroid be homogeneous (so that models derived from several areas produce a consistent solution) and that any non-uniformities in the disk (different star formation histories for example) had been accounted for. It is unlikely that the anomalous counts in the G352 field are due to a thick disk – the field is too far away from the disk of M31 for a thick disk with any plausible scale height and density normalization to have such a large effect. Studies of a possible Milky Way thick disk benefit from being able to look straight up through the thin disk and into the regions of interest. Studies of edge on spiral galaxies are also more suited to this task, presenting a profile of both the thin and thick disks. Investigation of other functional forms for the disk (isothermal, with a sech^2 dependence on height) and spheroid (a power law) can be done using the EGM model but are unlikely to solve this problem.

It would be desirable to compare the results of the EGM model to some independent data set. Fortunately such data is available in the form of the Pritchet & van den Bergh

1994 study. Figure 6.1 plots this data, corrected for contamination using the PvdB94 background field data, as connected points (logarithm of the number per square arc minute per 0.5 magnitudes) for four of the PvdB94 fields (M0, M1, M2 and E1). The dashed line is the EGM model results using the "mean G" LF, $\alpha_s = 0.6$, $r_e = 2$ kpc and a density normalization for the spheroid LF required to reproduce the G312 counts (3.1×10^{-6} stars pc^{-3}).

As can be seen the fit to the M0 and M1 fields is very good indeed, especially considering that the spheroid LF density was derived completely independently. The fit to the diagonal field E1 is worse, probably because the axial ratio of the model is not exactly right. The M2 field is approximately 1°.5 from the centre of M31 – at this point the numbers of contaminating objects is becoming relatively large and the fit correspondingly poorer.

It may be concluded that, broadly speaking, this type of analysis – using star counts rather than surface brightness – does work! Given reasonable model parameters and normalizations the EGM code will predict the counts one would expect to see. *Solving* for these parameters, on the other hand, is much more difficult and requires high quality data (and plenty of it). It is hoped that this model can be used in future studies to properly investigate the underlying physical structure of external galaxies as a complement to the method of examining the observed properties using surface brightness profiles.

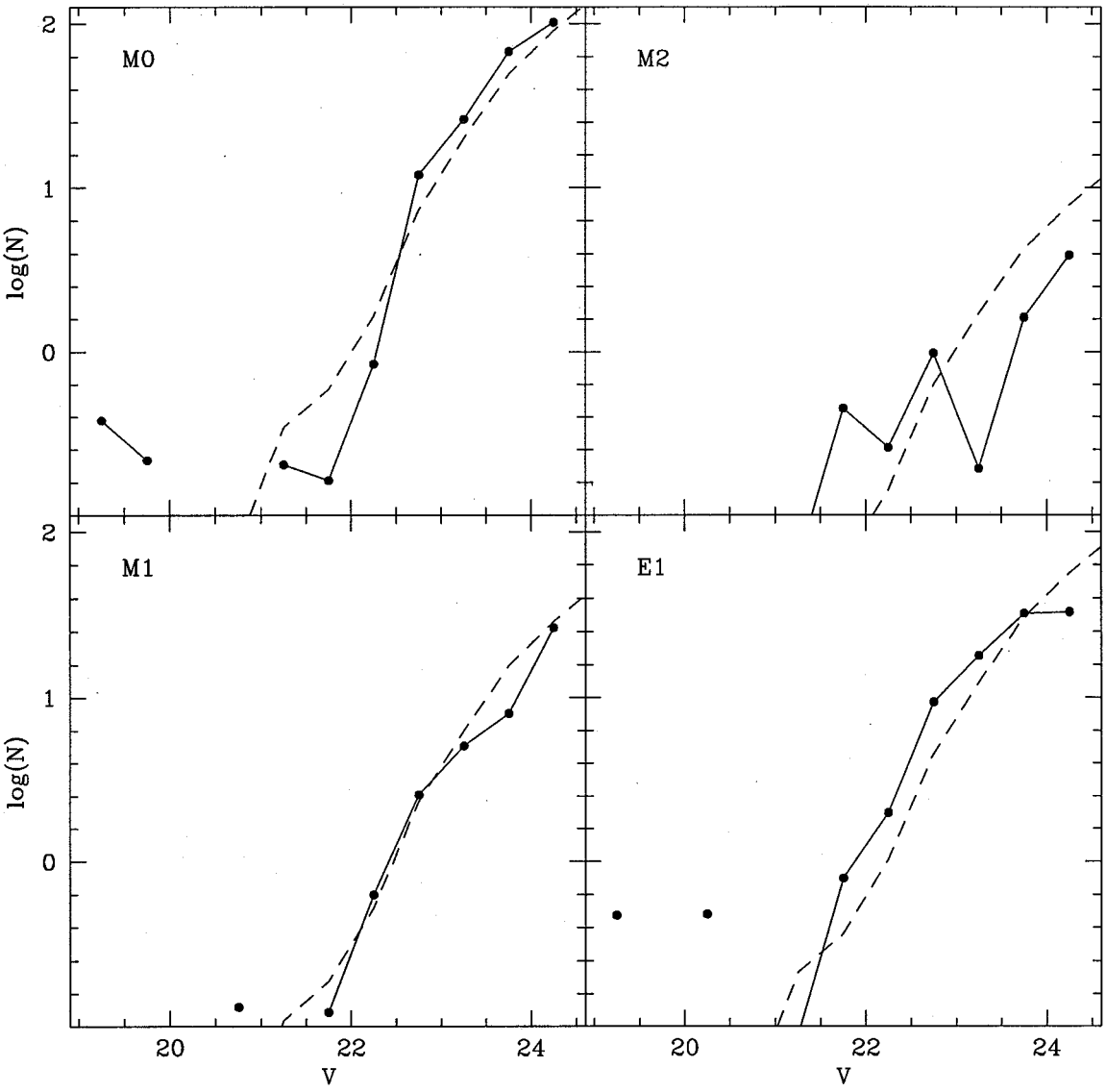

Figure 6.1: A comparison between the EGM model (dashed line) and the Pritchet & van den Bergh 1994 data (connected dots). The latter has been corrected for foreground and background contamination using the PvdB94 background data.

References

Baade, W. 1944, ApJ, 100, 137

Baade, W. 1963, in "Evolution of Stars and Galaxies", Harvard University, Cambridge, Mass., p. 73

Bahcall, J.N. 1986, ARAA, 24, 577

Bahcall, J.N. and Soneira, R.M. 1980, ApJS, 44, 73

Bahcall, J.N. and Soneira, R.M. 1984, ApJS, 55, 67

Bahcall, J.N., Schmidt, M. and Soneira, R.M. 1983, ApJ, 265, 730

Berkhuijsen, E. and Humphreys, R. 1989, A&A, 214, 68

Bergbusch, P.A. 1993, AJ, 106, 1024

Blaauw, A. 1965, in Galactic Structure (Stars and Stellar Systems, Vol. 5), ed. A. Blaauw, M. Schmidt, p. 435. Chicago: Univ. Chicago Press.

Burstein, D. and Heiles, C. 1984, ApJS, 54, 33

Caldwell, J.A.P. and Ostriker, J.P. 1981, ApJ, 251, 61

Carney, B.W., Latham, D.W. and Laird, J.B. 1989, AJ, 97, 423

Christian, C.A., Adams, M., Barnes, J.V., Butcher, H., Hayes, D.S., Mould, J.R. and Siegel, M. 1985, PASP, 97, 363

Christian, C.A. and Heasley, J.N. 1991, AJ, 101, 848

Da Costa, G.S. 1982, AJ, 87, 990

Drukier, G.A.D., Fahlman, G.G., Richer, H.B. and VandenBerg, D.A. 1988, AJ, 95, 1415

Eggen, O.J., Lynden–Bell, D. and Sandage, A. 1962, ApJ, 136, 748

Gilmore, G. & Reid, N. 1983, MNRAS, 202, 1025

Gilmore, G. & Wyse, R.F.G. 1985, AJ, 90, 2015

Heasly, J.N. and Christian, C.A. 1986, ApJ, 307, 738

Kaptyen, J.C. 1922, ApJ, 55, 302

Kernighan, B. W. and Ritchie, D. M. 1988, "The C programming language",
Englewood Cliffs, N.J. : Prentice Hall, 2nd ed.

Lang, K.R. 1991, in "Astrophysical Data: Planets and Stars",
New York: Springer-Verlag, p. 269

Landolt, A.U. 1992, AJ, 104, 340

Lindblad, B. 1927, MNRAS, 87, 553

Luyten, W.J. 1968, MNRAS, 139, 221

Majewski, S.R. 1992, ApJS, 78, 87

Malmquist, K.G. 1924, Medd. Lund. Astron. Obs., Ser. II, No. 32, 64

Malmquist, K.G. 1936, Stockholms Obs. Medd. No. 26

Massey, P., Armandroff, T.E. and Conti, P.S. 1986, AJ, 92, 1303

Mihalas, D. and Binney, J. 1981, "Galactic Astronomy: Structure and Kinematics",
San Francisco: Freeman

Mould, J. and Kristian, J. 1986, ApJ, 305, 591

Norris, J. 1986, ApJS, 61, 667

Norris, J. 1987, ApJ, 314, L39

Norris, J., Bessell, M.S. & Pickles, A.J. 1985, ApJS, 58, 463

Norris, J. and Green, E.M. 1989, ApJ, 337, 272

Oort, J.H. 1927, Bull. Astron. Inst. Netherlands, 3, 275

Oort, J.H. 1928, Bull. Astron. Inst. Netherlands, 4, 269

Pritchet, C. J. & van den Bergh, S. 1988, ApJ, 331, 135

Pritchet, C. J. & van den Bergh, S. 1994, AJ, 107, 1730 (PvdB94)

Ratnatunga, K.U. and Bahcall, J.N. 1985, ApJS, 59, 63

Reddish, V. 1962, Z. für Astrophys., 56, 194

Reid, N and Majewski, S.R. 1993, ApJ, 409, 635

Rose, J.A. 1985, AJ, 90, 787

Sandage, A.R. 1972, ApJ, 178, 1

Sargent, W.L.W., Kowal, C.T., Hartwick, F.D.A. and van den Bergh, S. 1977, AJ, 82, 947

Searle, L. and Zinn, R. 1978, ApJ, 225, 357

Shapley, H. 1919, ApJ, 50, 107

Stetson, P.B. 1987, PASP, 99, 191

Stetson, P.B. 1990, PASP, 102, 932

Tyson, J.A. 1988, AJ, 96, 1

van den Bergh, S. 1960, Publ. DDO, 2, 159

van den Bergh, S. 1966, AJ, 71, 219

van den Bergh, S. 1991, PASP, 103, 1053

de Vaucouleurs, 1959, in Handbuch der Physik, Vol. 53, ed. S. Flugge, Berlin, Springer–Verlag, p. 311

Walterbos, R.A.M. and Kennicutt, R.C. 1987, A&AS, 69, 311

Walterbos, R.A.M. and Kennicutt, R.C. 1988, A&A, 198, 61 (WK88)

Walterbos, R.A.M. and Schwering, P.B.W. 1987, A&A, 180, 27

Wielen, R. 1974, Highlights in Astronomy, vol. 3, p. 395

Woods, D., Fahlman, G.G. and Richer, H.B., 1995, ApJ, submitted

Young, 1976, AJ, 81, 807